Algorithm Theoretical Basis Document (ATBD)

Reference: CCI-LAKES2-0012-ATBD

Issue: 3.0.0 – 10/12/2025

Contract number: 4000125030/18/I-NB –Lakes_cci

11 rue Hermès, Parc Technologique du Canal — 31520 Ramonville Saint-Agne, France
Tel +33 (0)5 61 39 47 00 Fax +33(0)5 61 75 10 14
www.cls.fr

CHRONOLOGY ISSUES

Revised issue	[Legacy issues]	Date	Objective	Written by
1.0	1.0	09/12/2019	Initial Version	S. Simis et al.
	1.1	24/03/2020	Revision following ESA review	S. Simis et al.
	1.2	24/04/2020	Revision following 2nd ESA review	S. Simis et al.
	2.0	30/07/2020	Update of the LSWT chapter to take into account MODIS data. Update 4. 2: Optical LWE Estimates	C. Merchant, H. Yesou
	2.1	29/09/2020	Revision following ESA Review	J-F Crétaux, H. Yésou, C. Merchant
	2.2	17/03/2021	Update due to the new algorithm implemented for LIT and used for the CRDP version 1.1	C. Duguay
	2.3	30/03/2021	Minor corrections following the ESA Review	B. Coulon
2.0	3.0	03/05/2022	Accompanying CRDP v2.0	All authors
	3.1	06/07/2022	Revision following ESA Review	Laura Carrea
2.1	-	21/07/2023	Updates with CRDP v2.1 Addition of Lake Ice Thickness	S. Simis, L. Carrea, B. Calmettes, J-F Crétaux, C. Duguay, X. Liu, A. Mangili, D. Müller, H. Yésou
2.1.1	-	17/06/2023	Corrections following ESA review	S. Simis, L. Carrea, B. Calmettes, J-F Crétaux, C. Duguay, X. Liu, A. Mangili, D. Müller, H. Yésou
3.0.0	-	07/10/2025	Documentation accompanying CRDP v3.0.0	S. Simis, L. Carrea, B. Calmettes, J-F Crétaux, C. Duguay, C. Fatras, X. Liu, A. Mangili, D. Müller, H. Yésou

Note: versioning prior to 2022 did not follow the CRDP release sequence. The revised versioning in the first column should be used for future consistency.

BIBLIOGRAPHIC REFERENCE

This document may be cited as:

Simis, S., Carrea, L., Calmettes, B., Crétaux, J-F., Duguay, C., C. Fatras, Liu, X., Mangili, A. Müller, D., Yésou, H. 2025. Lakes Climate Change Inititiave Algorithm Theoretical Basis Document (ATBD), version 3.0.0. European Space Agency. DOI: 10.5281/zenodo.17288453

DOCUMENT REVIEW

Checked by	Stefan Simis – PML	
Approved by	Philippe Mourot - CLS	
Authorized by	Clément Albergel - ESA	

LIST OF CONTENTS

1 Introduction

This Algorithm Theoretical Basis Document (ATBD) describes the methodology, theoretical basis, assumptions and limitations of the algorithms used to derive the Essential Climate Variable (ECV) products from input satellite data, for the Lakes_cci Climate Research Data Package (CRDP) v3.0.0.

The ATBD details, as applicable for each part of the Lakes_cci ECV:

- Input satellite and ancillary data.
- Retrieval algorithms used, including:
    - the physical theory used as a basis
    - the mathematical, logical and heuristic procedures employed
    - simplifying assumptions made.
- A general overview of the processing chain for retrieval of the data products
- Any pre-processing or post-processing steps
- Sensor-specific optimisations of the algorithm
- Steps taken to ensure consistency between products derived from different satellite instruments, where applicable
- The approach to harmonisation of products from different instruments, where applicable.
- The approach to data merging, if performed.
- How product uncertainties are estimated on a per-datum prognostic basis, reflecting the combination of sources of uncertainty identified in the E3UB.
- Overall strengths and weaknesses or limitations of the product that are traceable to the algorithm/processing.

2 Lake Water level – LWL

2.1 Description of the algorithm and data/satellite used

Altimetry was originally designed for oceanography in the 1970s, and to study favourable continental surfaces, especially in hydrology and glaciology, two themes for which monitoring the height of water or ice surfaces is crucial. The principles of measurement have not changed over time, but the interpretation of measurements becomes more complex with increasing heterogeneity of the target, or the presence of slopes. Altimetry is not a singular measurement - multiple sensors on board an 'altimetry mission' satellite contribute to the quality of the measurement. Accurate orbit positioning sensors are crucial, as well as radiometers to determine the influence of atmospheric moisture on the signal. Dual-frequency altimeter systems for correcting the ionospheric delay are combined onto the same platform to gain the required precision in height measurement. However, these auxiliary sensors do not work for all continental surfaces as they do on ocean surfaces. This chapter, therefore, discusses the proposed solution for the challenge of altimetry of lake surfaces.

Satellite altimeters are designed to measure the two-way travel time of short radar (or laser) pulses reflected from the Earth's surface which gives the distance between the satellite and the reflected surface, called "range". The shape of the reflected signal, known as the "waveform", represents the power distribution of accumulated echoes from the radar pulse hitting the surface. The so-called onboard tracking system is the software which attempts to keep the reflected radar echo within the receiver observation window. The resulting waveforms are called 'tracked waveforms'. The travel time is calculated using a predefined analytic function, which fits the time distribution of the reflected energy. The fitting process of the acquired waveform is called re-tracking. The first altimetry missions were designed for the ocean domain and the corresponding algorithm, the so-called Brown model (Brown 1977) was fitted to classic ocean surfaces. This considers that thermal noise is followed by a rapid rise of the returned power called 'leading edge', and a gentle end sloping plateau known as 'trailing edge'. However, over the continents the waveforms are generally contaminated by noise resulting from multiple land returns such as vegetation, bare soil, or steep shorelines. Consequently, the shape of the echoes reflected by continental waters is often very different from that reflected by the ocean surface. It can thus become complex, if not impossible, to unambiguously calculate the water level of a river or small lake using the classic Brown analytic function. One way of working around this is to use alternative and more suitable re-tracking functions of the waveforms. Another way is to simulate the waveform and to recalculate the range as done with the LPP algorithm (see section 2.2). Moreover, several corrections that are commonly well measured over ocean are also degraded over continental surface and lead to use specific models.

2.2 Algorithm definition

Here, Lake Water Level (LWL) is measured using satellite radar altimetry (alternatively, Lidar altimetry, for example on ICESat-1 and ICEsat-2 missions, can also be considered).

Radar altimeters send an electromagnetic pulse to the satellite nadir and record the propagation time to and from the emitted wave and its echo from the surface. The electromagnetic bands of interest are the Ku and Ka bands, with are reflected perfectly – without penetration – by water (which is not the case for snow and ice). Multiplied by the speed of light c, half the time it takes for the transmission Δt gives length R (the range) between the satellite and the reflective surface:

$$R = c \frac{\Delta t}{2} \qquad [3.1]$$

The height *H* of the reflective surface is given by the following equation:

$$H = a - (R + \Sigma C_p + \Sigma C_g) \qquad [3.2]$$

where *a* is the orbital altitude of the satellite with respect to the ellipsoid. Corrections must be made for propagation in the atmosphere (C_p) and also vertical movements of the Earth's crust (C_g).

The ellipsoidal height is then converted into elevation *h*, taking the local undulation of geoid N into account:

$$h = H - N \qquad [3.3]$$

The ΣC_p and ΣC_g terms in Equation 3.2 correspond to sets of corrections that must be subtracted to arrive at an accurate estimation of H.

There are two types of corrections:

- propagation corrections needed because the radar pulse propagates through the atmosphere at a speed below the speed of light c used in Eq. 4.1
- geophysical corrections linked to the vertical movements of the Earth surface (tides, for example) and for which we want to correct the measurement in order to apply it to a fixed geodetic datum in the terrestrial reference frame.

Finally, we can express the height of a lake by the full following equation:

$$h = a - R - DTC - WTC - IC - ET - PT - LT - SSB - N \qquad [3.4]$$

where DTC is the dry tropospheric correction, WTC the wet tropospheric correction, IC the ionospheric correction, ET the Earth tide, PT the polar tide, LT the lake tide and SSB the instrumental so-called sea state bias. In the case of inland water products, these geophysical corrections come from models and are provided in the altimetry datasets. For some past missions, a temporal interpolation may be required.

The LWL in the Lakes_cci CRDP version 3.0 includes data estimated using a new Lake Physical Processing (LPP) algorithm developed at CNES. The detailed calculation of LWL using the LPP approach is given in Boy et al. (2022). The algorithm has been used for a series of lakes where data processing based on ICE-1 retracking of the waveform was inoperant. The LPP is based on simulation the altimeter waveforms used within the retracking algorithm. Simulation uses a lake contour to match the measurement geometry. The simulated range is then used for the estimation of lake elevation. The waveform shape depends on surface roughness, ranging from diffuse (when roughness is high) to specular (when roughness is very low). The simulated waveforms are used to determine the water signal inside the radargram, to filter out contamination from the surrounding environment. Once the radargram is cleaned up, the lake elevation and surface roughness are inverted, reducing the mean quadratic error between the waveform and the simulation.

The LPP processing is designed to retrack Synthetic Aperture Radar (SAR) data from on board Synthetic aperture Radar Altimeter (SRAL) on Sentinel-3A, Sentinel-3B and Sentinel-6A. The 'peakiness' of the waveform at the center of the lake gives an indication of the waveform shape or how the backscatter is behaving. This can range from a perfect square cardinal sinus ($Sinc^2$) to the so-called Brown model that is usually seen over the ocean or large lakes. This method is well adapted for small lakes, where waveforms almost never follow the Brown model, by first classifying waveforms with respect to their shape. The shape of the waveform depends on two factors: (i) the

illuminated surface included in the radar footprint and (ii) the roughness of the surface. Figure 1 illustrates simulated variation in peakiness, with dispersion around the peak for spread-out waveforms and peakiness reaching 1 when the waveform has the shape of a Dirac. To get accurate and precise water surface elevation, the model used inside the retracking must account for the physics that is responsible for these complex behaviors.

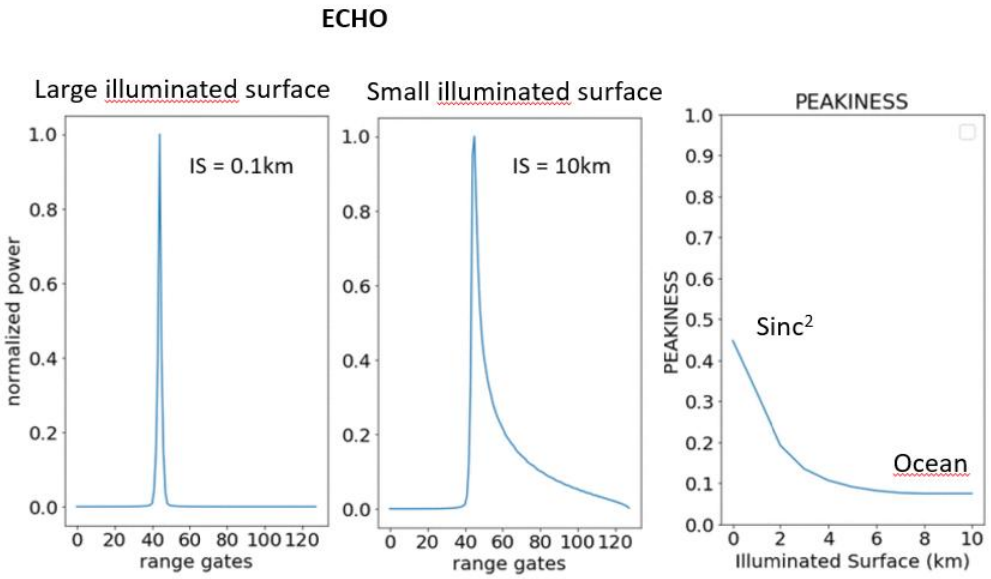

Figure 1. Simulations of SAR waveforms depending on the peakiness with regard to illuminated surface and mean square slope (mss).

The calculation of LWL in the LPP algorithm has three steps:

1) For each satellite pass over the lake, numerical simulations of the radar waveforms are built using a lake contour. The inversion is done over the entire radar acquisition sequence along the lake, to identify the approximate location of the water signal inside the radargram and to filter out contamination. This simulation consists of recognizing the simulated pattern in the observed radargram by adjusting the mean square slope (mss) and the LWL from the simulation, using least-squares adjustment. Convergence in the least squares adjustment of the Water Surface Elevation (WSE, pertaining to Level-2 processing steps), influenced by the chaotic shape of waveforms, is achieved by iterating two terms:

    a) WSE from gate 0 to 127 with a gate step of $1/8^{th}$

    b) $\log_{10}$(mss) from 0 dB to -8 dB with a -1 dB step.

    This results in a first guess of water height and roughness: $WSE1^{st}$ and $mss1^{st}$.

2) Rejecting contaminations of the signal from non-water surfaces is done by editing individual waveforms not simulated in the first phase. To remove non-water signals the range gates with a simulated normalized power below -20dB are rejected. Moreover, we keep only ten gates around WSE^{st} .

3) Once the signals received have been cleaned from spurious waveforms, individual waveform retracking can be performed, meaning that the retracking is applied for each valid measurement.

These three steps allow calculation of the range. LWL is then computed according to Eq. 4.

2.3 Quality assessment

Quality assessment is carried out by comparing the retrieved LWL with independent in situ measurements. In situ measurements are available for some lakes on national hydrological services, for example in Canada or Brazil, for selected lakes and reservoirs, or they are released to the project team by the State Hydrological Institute of St Petersburg within the framework of the Hydrolare data centre. A set of approximately 20 lakes regularly serve as validation data sets for altimetry products. The accuracy of lake height measurement depends on several factors: range, orbit and correction errors. Range errors result from surface roughness and quality of the retracking of the altimeter waveform. It is also important to emphasize that the altimeter measurement is an average over the footprint which intrinsically differs from a single point measurement of a ground gauge, and which is furthermore generally done along the coastline.

Performing comparisons over a set of several lakes and reservoirs of varying morphology and from different regions addresses the recurring question of accuracy of altimetry for lakes and reservoirs and its dependency on the size of the water bodies. It is not clear whether a minimum size threshold exists below which the altimeter does not provide valid water levels. Past studies (see Cretaux et al. 2016) have shown that the accuracy of LWL is largely sub-decimetre for large lakes and that lake size influences the quality of the measurement. However, these results also show that accuracy is dependent on the lake environment: mountain lakes or those with ice and snow in winter, as well as large but narrow reservoirs have degraded accuracy. For Lake Onega for example, the RMS accuracy was twice as good when winter months were excluded compared to the year as a whole. Past studies further show that accuracy of LWL products ranges from a few centimetres for very large lakes to a few decimetres for small or narrow lakes (Ričko et al. 2012, Cretaux et al. 2016). However, new missions like the Sentinel-3 constellation present new technological developments from which improved accuracy have been largely demonstrated (Boy et al., 2022; Taburet at al., 2020; Quartly et al., 2020), owing to acquisition in SAR mode. This will have little effect for large lakes (Cretaux et al. 2016) but prompts new assessment to gauge the extent of improvements over smaller lakes.

2.4 Summary of strengths, weaknesses and limitations

Since LWL products are exclusively based on satellite altimetry, its coverage depends on the satellite constellation, which present some limitations since some lakes will only occasionally be observed, while other lakes are never found under the altimeter track.

Since the launch of Topex / Poseidon in 1992, radar altimetry has evolved a lot from low resolution mode to SAR mode, from Ku band to Ka Band (Saral/Altika), which leads to disparity in the quality of the time series from one lake to another one, and for lakes covered by several altimeters. This is particularly true for small or narrow lakes, for which the SAR mode is more adapted and allows calculating more precise time series.

With the SWOT mission, which has a full coverage of the continent following requirements to resolve all lake levels, extent, and volume changes for lakes bigger than 6 ha, we expect much better results and we would be able to provide LWL for all lakes in the database in future.

The strength of satellite altimetry is that it is perennial (with current and future constellation of sentinel-3, sentinel-3NG, sentinel-6, SWOT, Icesat-2). Moreover, radar altimetry is not affected by cloud coverage.

With more than 30 years of altimetry data processing, the technique is robust, and many improvements have been progressively implemented in the data processing over lakes. LWL products then can serve as input for LWE inferring potential global studies on lake storage changes (Yao et al., 2023).

2.5 References

Birkett C. M. (1995). Contribution of TOPEX/POSEIDON to the global monitoring of climatically sensitive lakes, Journal of Geophysical Research, 100, C12, 25, 179-25, 204

Boy F., Cretaux J-F., Boussaroque M., & Tison C. (2022). Improving Sentinel-3 SAR mode processing over lake using numerical simulations, IEEE Transactions on Geoscience and Remote Sensing, 60, 1-18, Art no. 5220518, Doi: 10.1109/TGRS.2021.3137034

Brown G. S. (1977). The Average Impulse Response of a rough surface and its applications, IEEE Trans. Antennas Propag, Vol. 25, pp. 67-74. 10.1109/TAP.1977.1141536

Crétaux J-F. and Birkett C. M. (2006). Lake studies from satellite altimetry, C R Geoscience, 10.1016/J.crte.2006.08.002

Crétaux J-F. Calmant S. Romanovski V. Perosanz F. Tashbaeva S. Bonnefond P. Moreira D. Shum C. K. Nino F. Bergé-Nguyen M. Fleury S. Gegout P. Abarca Del Rio R. Maisongrande P. (2011). Absolute Calibration of Jason radar altimeters from GPS kinematic campaigns over Lake Issykkul, Marine Geodesy, 34: 3-4, 291-318, 10.080/01490419.2011.585110

Crétaux J-F, Abarca Del Rio R. Berge-Nguyen M. Arsen A. Drolon V. Clos G. Maisongrande P. (2016). Lake volume monitoring from Space, Survey in geophysics, 37: 269-305. 10.1007/s10712-016-9362-6

Crétaux J-F. Bergé-Nguyen M. Calmant S. Jamangulova N. Satylkanov R. Lyard F. Perosanz F. Verron J. Montazem A. S. Leguilcher G. Leroux D. Barrie J. Maisongrande P. and Bonnefond P. (2018). Absolute calibration / validation of the altimeters on Sentinel-3A and Jason-3 over the lake Issykkul, Remote sensing, 10, 1679. 10.3390/rs10111679

Quartly, G.D.; Nencioli, F.; Raynal, M.; Bonnefond, P.; Nilo Garcia, P.; Garcia-Mondéjar, A.; Flores de la Cruz, A.; Crétaux, J.-F.; Taburet, N.; Frery, M.-L.; Cancet, M.; Muir, A.; Brockley, D.; McMillan, M.; Abdalla, S.; Fleury, S.; Cadier, E.; Gao, Q.; Escorihuela, M.J.; Roca, M.; Bergé-Nguyen, M.; Laurain, O.; Bruniquel, J.; Féménias, P.; Lucas, B. (2020). The Roles of the S3MPC: Monitoring, Validation and Evolution of Sentinel-3 Altimetry Observations. Remote Sens. 12, 1763. doi:10.3390/rs121111763

Ričko M. C. M. Birkett, J. A. Carton, and J-F. Cretaux. (2012). Intercomparison and validation of continental water level products derived from satellite radar altimetry, J. of Applied Rem. Sensing 6, Art N°: 061710.10.1117/1.JRS.6.061710

Taburet N., Zawadzki., Vayre M., Blumstein D., LE Gac S., Boy F., Raynal M., Labroue S., Cretaux J-F., and Femenias P. (2020). S3MPC: Improvement on inland water tracking and water level monitoring from the OLTC onboard Sentinel-3 altimeters, Remote Sensing 12, 18, AN 3055, Doi: 10.3390/rs12183055

Yao F., Ben Livneh B., Rajagopalan B., Wang J., Crétaux J-F., Wada Y., Berge-Nguyen M. (2023). Satellites reveal widespread decline in global lake water storage, *Science* 380, 743-749.

3 Lake water extent -LWE

3.1 Description

Lake Water Extent (LWE) can be expressed as the outline of a water body (a shape) or as the total areal extent of a waterbody (a single quantity). It is practically very challenging to process the high spatial resolution satellite imagery required to generate maps of water presence for hundreds, if not thousands, of lakes at the accuracy and temporal frequency required for climate studies. For this reason, the strategy adopted is twofold. First, for each lake, we collect satellite imagery spread out over a long time period. To choose the images we use the water level time series (calculated using satellite altimetry) to determine when the lake was at low, medium, and high level. A relationship (a first or second order polynomial) can then be established using a set of 10 to 15 data combinations of LWL and LWE and least square adjustment. We can then relate LWL from altimetry to LWE using the established so-called hypsometric relation. This allows us to achieve a high temporal resolution of both LWL and LWE without overwhelming image processing requirements. The relationship is stable over long periods of time if the geomorphology of the lake and immediate surrounding landscape does not markedly change.

LWE maps used to calculate the hypsometry coefficients are determined from contrasts in the optical reflectance of water compared to surrounding land. Water surfaces are detected using a multilayer perceptron (neural network) algorithm and integrating the GSW database for sampling. This processing chain is implemented as part of a processing chain for Sentinels 1-3 used to derive several properties including water, fire, and cloud detection, in time series context with large spatial and temporal windows.

3.2 Algorithm definition

To calculate the LWE we use the vector (ΔLWL, LWE) derived from corresponding altimetry and water extent observations to estimate, by least square adjustment, the coefficients representing the polynomial subsequently used as hypsometry curve. LWL is then used together with the hypsometry coefficient to determine the LWE variable. This procedure is detailed as follows.

We first use the water level time series inferred from satellite altimetry and released as LWL products, to determine key periods when the lake was at extreme heights, as well as some intermediate values. Satellite images are then selected for the same dates for water mask detection using approaches described above. It is not realistic to determine water extent of a lake for each measurement of its water level, especially when a lake is too large and is not covered by only one image. We select between 10 and 20 images at different dates and calculate the hypsometry relationship (LWE/dLWL) which is then applied to determine surface extent of the lakes each time a water level is calculated using satellite altimetry. The hypsometry is expressed as a polynomial of degree 1, 2 or 3 depending on the linearity of the couples of water level and surface extent of the lake. In such processing, we do not need to process a large amount of satellite images, and this is a practical way to produce lake surface extent together with lake water level. We do not extrapolate the water surface for water height outside of the maximum and minimum values used to determine polynomial coefficients. Therefore, we try to collect satellite images as close as possible to the maximum and minimum level observed from satellite altimetry. The method is applied and described in Cretaux et al. (2015, 2016).

In a previous, dedicated Lakes_cci effort, various methods for image based LWE determination were compared, using both optical and radar methods. Based on the results of inter-comparison on a small set of lakes with increasingly complex hydromorphology, an approach based only on

optical HR imagery was adopted. Water surfaces were extracted from the images based on the exploitation of an in-house processing chain (Figure 2), named ExtractEO (Maxant et al, 2022).

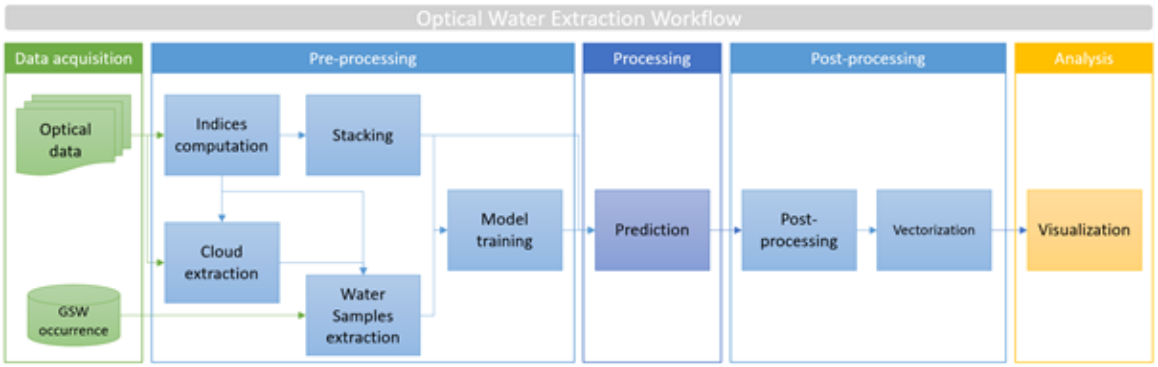

Figure 2: Optical Water Extraction Workflow

The preprocessing steps correspond to:

- Region Of Interest (ROI) is defined including the target lake.
- Selection of set of images representative of the different water levels of the target, i.e. based on altimetric water level curves obtained from HydroWebNext (previously Hydroweb).

The processing then follows the scheme shown in Figure 3:

- Automatic water sample generation from Global Surface Water. Water indices are computed to remove outliers and filter the training samples to the hydrological reality of the image (water extent, resolution)
- Training using the Multi-Layer Perceptron classifier
- Slope and hillshade thresholds derived from HR DEMs are applied to refine the water extraction (post-processing)
- Minimum mapping unit (MMU) sieving to remove small features (0,1 hectares in this case)
- Water extent (in km^2) is subsequently calculated using the sum of individual pixel classified as water pixel within the ROI
- Generation of a max extent water mask

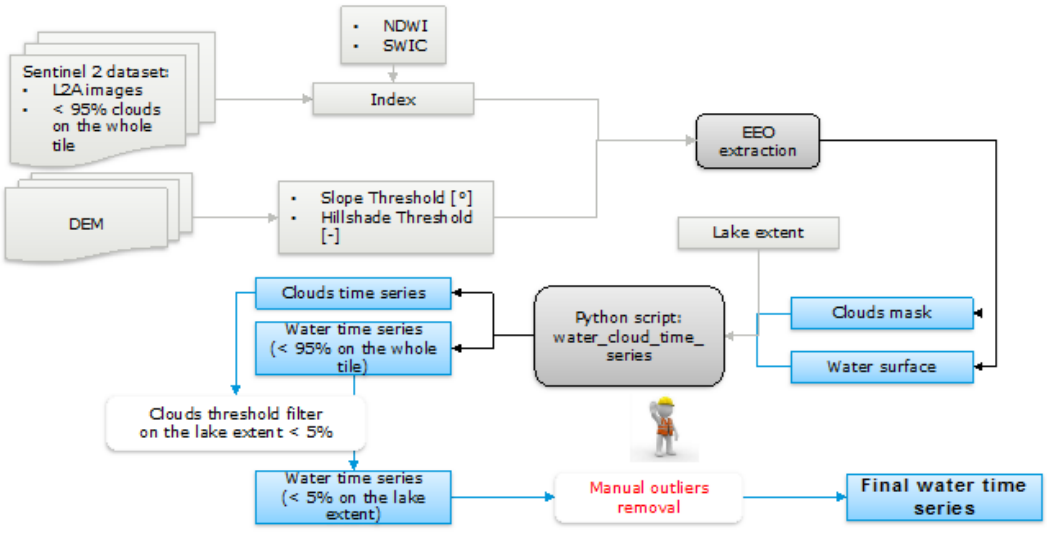

Figure 3: Detailed workflow of the water extraction procedure within ExtractEO

From a first set of selected images/dates, after outlier removal, 10 to 20 images are retained to calculate the hypsometry relationship.

3.3 Quality assessment

A final estimation of accuracy is calculated on all vectors used to calculate the hypsometry coefficients. The hypsometry is represented by a linear or a quadratic polynomial, depending on lake morphology, and is estimated using a set of 10-15 vectors (LWL, LWE) for a selection of dates at different levels. A way to estimate the associated uncertainty is to calculate the RMS of the differences between the theoretical (calculated from hypsometry's coefficient) and the measured LWE (directly from satellite imagery) for the dates that have been chosen to build the hypsometry. A series of tests done over a set of 40 lakes have shown that the estimated RMS of LWE was lower than 2 % of the total extent for each of the 40 lakes.

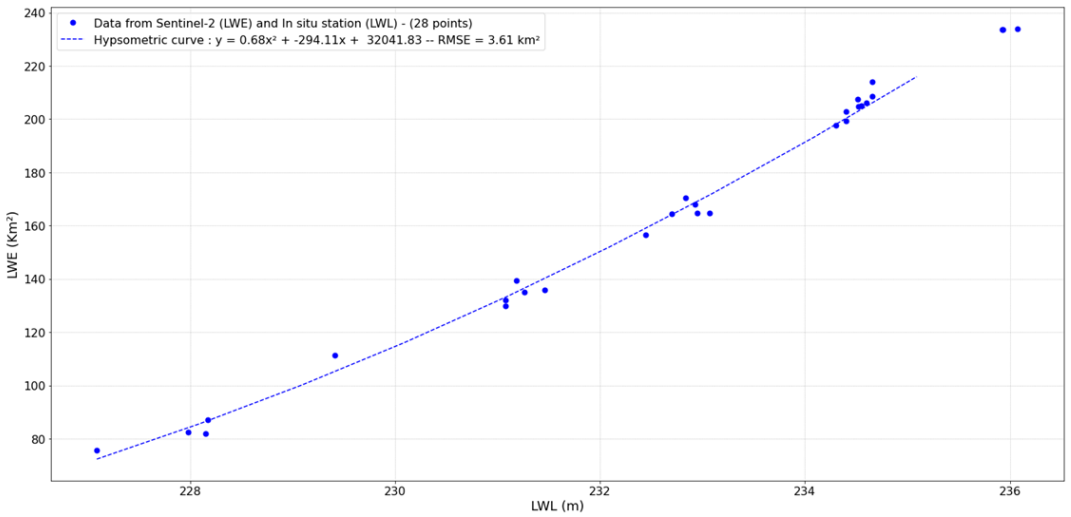

Figure 4: Resulting hypsometry for the lake Bagre in Africa using a set of 26 Sentinel-2 images and LWL time series..

3.4 Summary of the strengths, weaknesses and limitations

Strengths:

- A robust and proved method
- RMS meets the target requirements

Weaknesses:

- Access to input data timeseries, i.e. Landsat for early observations and Sentinel-2 for recent observations, can be a bottleneck. Limited access to the full Sentinel archives through the European DIAS providers is solved by using a FORCE gateway or the AWS capabilities.
- Availability of cloud-free optical data
- Gaps in the satellite archive (i.e. Landsat 7)
- Time consuming process to reach the required fine adjustment of the hypsometric curves

Limitations:

- There are (few) lakes for which there is no correspondence between surface extractions and corresponding elevation values.

- Observation limitations with mountainous deep lakes, with sharp banks, showing limited surface area expansion when waters rise.

3.5 References

Cretaux J-F. Biancamaria S. Arsen A. Bergé-Nguyen M. and Becker M. (2015). Global surveys of reservoirs and lakes from satellites and regional application to the Syrdarya river basin, *Environmental Research Letter*, 10, 1, AN: 015002. doi: 10.1088/1748-9326/10/1/015002

Crétaux J-F, Abarca Del Rio R, Berge-Nguyen M, Arsen A, Drolon V, Clos G, Maisongrande P. (2016). Lake volume monitoring from Space, *Survey in geophysics*, 37: 269-305, Doi 10.1007/s10712-016-9362-6

Maxant J, Braun R, Caspard M, Clandillon S. (2022). ExtractEO, a Pipeline for Disaster Extent Mapping in the Context of Emergency Management. Remote Sensing. .14(20):5253. https://doi.org/10.3390/rs14205253

McFeeters S. K. (1996) The use of Normalized Difference Water Index (NDWI) in the delineation of open water features, International Journal of Remote Sensing, 17(7):1425–1432

4 Lake surface water temperature – LSWT

4.1 Description

This section describes the algorithm for Lake Surface Water Temperature (LSWT) production chain. For consistency with data produced in heritage projects, version 4.5 of the production chain described here for CRDP v3.0.0 refers to the scientific versioning of the climate data record in a manner already familiar to users of data from previous projects, with GloboLakes offering product generation v4.0 (Carrea et al. 2019) and the first version from Lakes_cci being v4.1. The algorithm described here is v4.5 and includes the following changes with respect to the previous version LSWT v4.1.

- LSWT v4.5 includes data from the Moderate-resolution Imaging Spectroradiometer (MODIS) on Terra processed with ERA-5 (the most recent numerical weather prediction, NWP, re-analysis from ECMWF) and RTTOV12 as forward model.
- Reprocessed data are included from the Sea and Land Surface Temperature Radiometer (SLSTR) on Sentinel3A and Sentinel3B processed with the ECMWF operational meteorological files contained in the L1b SLSTR files.
- For all the other instruments, for the forward model RTTOV 11 was employed while the ERA-Interim reanalysis was utilised for the NWP fields.

The LSWT climate data record (CDR) is based on data from the following instruments: Along-Track Scanning Radiometer (ATSR), the Advanced Very High-Resolution Radiometer (AVHRR), the Sea and Land Surface Temperature Radiometer (SLSTR) series and Moderate Resolution Imaging Spectroradiometer (MODIS) on Terra. The timeline of the instruments used is summarised in Table 1.

Table 1 - List of the instruments used

Instrument/Platform	Start	End	NWP
ATSR2/ERS2	01/06/1995	22/06/2003	ERA-Interim
AATSR/Envisat	20/05/2002	08/04/2012	ERA-Interim
MODIS/Terra	24/02/2000	31/12/2022	ERA5
AVHRR/MetOpA	01/03/2007	31/08/2019	ERA-Interim
AVHRR/MetOpB	13/12/2012	31/08/2019	ERA-Interim
SLSTR/Sentinel3A	01/06/2016	31/12/2023	ECMWF operational
SLSTR/Sentinel3B	01/07/2018	31/12/2023	ECMWF operational

The scope of this algorithm description applies to the following steps:

1) identification of water-only pixels for valid retrieval,
2) the LSWT retrieval itself,
3) estimating the daily average LSWT from the instantaneous skin observation,
4) assigning a pixel quality level,
5) remapping the data to a regular global grid,
6) cross-sensor LSWT harmonization.

4.2 Algorithm definition

The LSWT processing sequence is described in Figure 5. The individual processing steps are described in turn below.

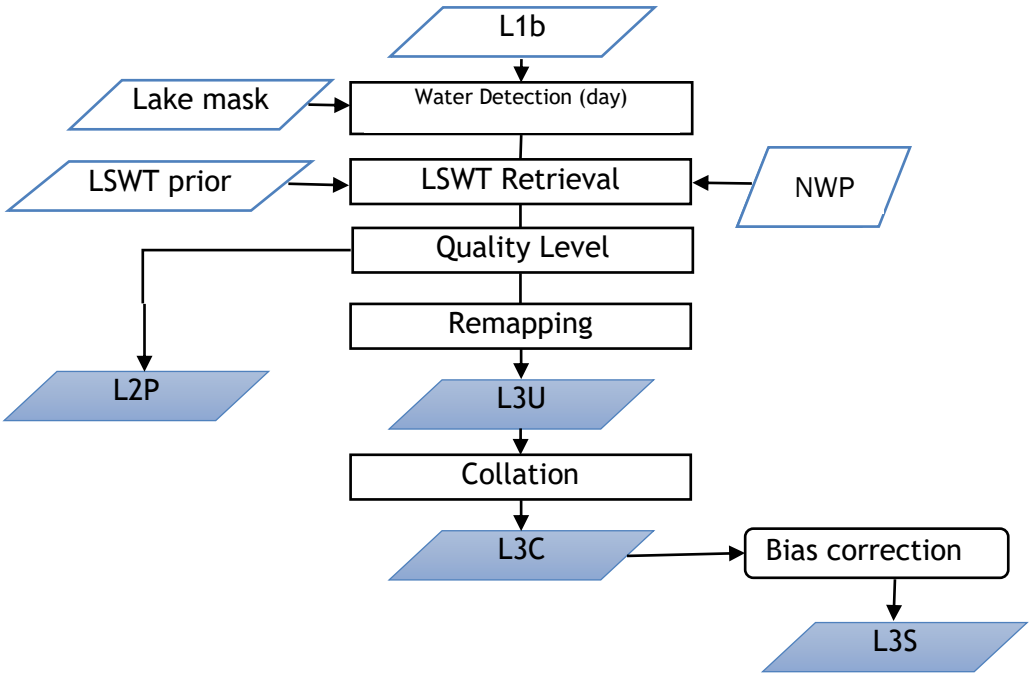

Figure 5: Major steps in LSWT processing

4.2.1 Water detection

Water detection is applied to potential inland water pixels. It operates by calculating a score against several metrics, derived from reflectance channels available. For this reason, LSWT products are in this version obtained only from daytime scenes.

The score for a given metric is defined as:

$$s = \begin{cases} 0 & \text{if } X \le t_0 \\ \frac{X - t_0}{t_1 - t_0} & \text{if } t_0 < X < t_1 \\ 1 & \text{if } X \ge t_1 \end{cases} \qquad [4.1]$$

The score is a linear ramp between 0 and 1, similar to well-known concepts of “fuzzy logic” (the scores are like probabilities).

The values of the terms in [4.1] are given in Table 2. The first three metrics based on red, near infra-red and shortwave infra-red bands use the expectation that reflection from a cloud-affected pixel exceeds that from a clear view of a lake, with values appropriate to different wavelengths.

The MNDWI is the modified normalised difference water index. The NDVI is a normalised difference vegetation index. The setting of the thresholds was done (within GloboLakes) using AATSR imagery tuned to a probability of cloud image derived from MERIS 300 m imagery. The tuning of thresholds was done one-at-time across metrics, maximising the posterior probability that a certain pixel is cloudy or cloud free.

Table 2: Thresholds test for water detection

$\boldsymbol{X}$, metric	Score definition	Thresholds
R_{670}	$\boldsymbol{s} = \begin{cases} 0 & \text{if } X \geq t_0 \\ \dfrac{X - t_0}{t_1 - t_0} & \text{if } t_1 < X < t_0 \\ 1 & \text{if } X \leq t_1 \end{cases}$	t_0 = 0.132 t_1 = 0.032
R_{870}	$\boldsymbol{s} = \begin{cases} 0 & \text{if } X \geq t_0 \\ \dfrac{X - t_0}{t_1 - t_0} & \text{if } t_1 < X < t_0 \\ 1 & \text{if } X \leq t_1 \end{cases}$	t_0 = 0.097 t_1 = 0.022
R_{1600}	$\boldsymbol{s} = \begin{cases} 0 & \text{if } X \geq t_0 \\ \dfrac{X - t_0}{t_1 - t_0} & \text{if } t_1 < X < t_0 \\ 1 & \text{if } X \leq t_1 \end{cases}$	t_0 = 0.048 t_1 = 0.012
MNDWI	$\boldsymbol{s} = \begin{cases} 0 & \text{if } X \leq t_0 \\ \dfrac{X - t_0}{t_1 - t_0} & \text{if } t_0 < X < t_1 \\ 1 & \text{if } X \geq t_1 \end{cases}$	t_0 = 0.295 t_1 = 0.515
NDVI	$\boldsymbol{s} = \begin{cases} 0 & \text{if } X \geq t_0 \\ \dfrac{X - t_0}{t_1 - t_0} & \text{if } t_1 < X < t_0 \\ 1 & \text{if } X \leq t_1 \end{cases}$	t_0 = -0.085 t_1 = -0.245
MNDWI-NDVI	$\boldsymbol{s} = \begin{cases} 0 & \text{if } X \leq t_0 \\ \dfrac{X - t_0}{t_1 - t_0} & \text{if } t_0 < X < t_1 \\ 1 & \text{if } X \geq t_1 \end{cases}$	t_0 = 0.375 t_1 = 0.685

The first three metrics use the expectation that reflection from a cloud-affected pixel exceeds that from a clear view of a lake, with values appropriate to different wavelengths. The MNDWI is the modified normalised difference water index. The NDVI is a normalised difference vegetation index. The setting of the thresholds was done (within GloboLakes) using AATSR imagery tuned to a probability of cloud image derived from MERIS 300m imagery. The tuning of thresholds was done one-at-time across metrics, maximising the posterior probability that a certain pixel is cloudy or cloud free.

The same method will apply for AATSR, AVHRR and MODIS, although the parameter values will be re-evaluated for MODIS. Additionally, to maximise consistency across the Lake_cci project, we expect to use full resolution information from the MODIS LIC processing chain to exclude ice-covered pixels consistently.

4.2.2 LSWT retrieval

The retrieval scheme is the optimal estimation (OE) scheme (MacCallum et al. 2012) for all sensors, the equation for which is:

$$\hat{\boldsymbol{x}} = \boldsymbol{x_a} + \boldsymbol{G}\big(\boldsymbol{y} - \boldsymbol{F}(\boldsymbol{x_a})\big) \quad with \quad \boldsymbol{G} = (\boldsymbol{K}^T\boldsymbol{S}_\varepsilon^{-1}\boldsymbol{K} + \boldsymbol{S}_a^{-1})^{-1}\boldsymbol{K}^T\boldsymbol{S}_\varepsilon^{-1} \qquad [4.2]$$

The retrieved state $\hat{\boldsymbol{x}}$ is the prior state $\boldsymbol{x_a}$ plus an increment of $\mathbf{G}\left(\boldsymbol{y} - F(\boldsymbol{x}_a)\right)$ where F is the forward model, i.e. the radiative transfer model (RTM) runs for the prior re-analysis data and prior LSWT. The matrix $\mathbf{K}$ expresses how the observations change for departures from the prior state x_a, i.e. it is a matrix where a given row contains the partial derivatives of the brightness temperature in a particular channel with respect to each element of the state vector in turn. The partial derivatives are the tangent linear outputs from the forward model $\mathbf{F}$. $\mathbf{S}_\varepsilon$ is the error covariance of the differences between the model and observed brightness temperatures. This error covariance matrix is the sum of the radiometric error covariance in the observations ($\mathbf{S}_o$) and estimated error covariance of the forward model ($\mathbf{S}_m$). $\mathbf{S}_a$ is the error covariance matrix for the prior state variables.

Standard OE theory also enables estimation of the retrieval uncertainty (to be output), a diagnostic of fit (the χ^2 of the retrieval fit) and the sensitivity of the retrieval to the true LSWT ("averaging kernel" in retrieval theory). The latter two outputs are used within quality level attribution (see below).

4.2.3 Quality levels

Quality level is treated as a concept that is distinct from uncertainty: a highly uncertain LSWT can have the highest quality level if all the conditions for giving a valid LSWT and valid LSWT uncertainty are met: the quality level reflects the degree of confidence in the validity of the uncertainty estimate and not the magnitude of data uncertainty.

The quality level assigned to a pixel will be the lowest level (row of table) which matches any of the conditions shown in Table 3. The assignments are compatible with GHRSST conventions: i.e. a particular level is given if none of the conditions higher up any column of the table are met.

Table 3: Quality level criteria. d = distance to land in km.

Level	Meaning	Water detection score (0. 5<d<=1.5)	Water detection score (d>=1.5)	Sensitivity	χ^2	Other
0	No data	<0	<0			No data; non-lakes pixel
1	Bad data	<0.5	<0	<0.1	>3	LSWT < 273.15
2	Worst quality	<2	<0.5	<0.5	>2	θ_{sat} > 55
3	Low quality	<3.5	<2	<0.9	>1	
4	Acceptable quality	<4.5	<3.5		>0.35	

For instance, any pixel where the water detection score is unavailable (value is less than zero), required input, the brightness temperatures (BTs), are unavailable, or which is over land will be assigned quality level of 0. Next, any pixels close to land which have s < 0.5, calculated LSWT sensitivity < 0.1 etc. will be assigned quality level of 1 and so on.

- Quality level 0 pixels should contain no other data
- Quality level 2-5 pixels should always contain valid data
- Quality level 1 pixels contain data, but the data are not suitable for use (bad data). For instance, the LSWT retrieval may have been attempted, but rejected as bad data due to low sensitivity etc

We recommend using quality level 4 and 5, and consideration of use of quality level 3 with caution, depending on application.

4.2.4 Remapping (L3U)

The remapping from the L2 data in swath projection to the fixed L3 grid proceeds as follows:

- Identify L2 pixels contributing to a L3 cell
- Select highest quality level pixel(s) in the L3 cell
- Calculate average LSWT from the pixels that share the highest quality level and propagate uncertainties to the uncertainty in this average (Bulgin et al. 2016a)

When averaging from the pixel scale to L3 grid scale, the component or uncertainty from uncorrelated errors reduces (uncertainty in the mean is scaled by the familiar "$1/\sqrt{n}$"). Uncertainty in the correlated error components is not reduced by averaging, since over these small scales the degree of correlation will be very high and is taken to be perfect ("r = 1"). The total uncertainty in the average is found by combining the propagated component uncertainties.

If the grid cell contains pixels which were not included in the averaging (e. g. due to the presence of cloud etc.), then there is an additional uncertainty due to incomplete sampling. This is calculated following Bulgin et al. (2016b) (derived for application to sea surface temperature uncertainty estimation) and is added to the uncorrelated component.

4.2.5 Daily Collation (L3C)

The polar orbiting satellite carrying the AVHRR/ATSR sensors typically complete 14-15 orbits each day resulting in the same number of L2P or L3U products. While L3U files are on a global grid, they are very sparse as the sensor will only observe a small fraction of the Earth's surface in each orbit. For ease of use the LSWT outputs are collated to produce one file for each 24-hour period, corresponding to day-time observations.

Following the GHRSST conventions [D1], when collating observations from overlapping orbits in the same day the L3C will contain the highest quality observation available in the 24-hour period. The selection of best observation is done as follows:

- Choose input cells with the highest quality level
- If multiple observations have the same quality level, then average.

4.2.6 Inter-sensor adjustment (L3S)

Inter-sensor adjustment applies small adjustment factors to reconcile typical differences between the LSWT obtained from different sensors. This is done by selecting a reference sensor and applying a per-lake adjustment to other sensors. This adjustment is applied only if:

- Enough observations where available to estimate the adjustment for the lake (more than 3 months of data for each sensor-to-reference pair).

The uncertainty of the adjustment was less than 0.049 K for 80% of the lakes.

For MODIS, only LSWTs of quality level 4 and 5 have been used for the final dataset and an overall adjustment of 0.19K and 0.11K for quality level 4 and 5 respectively have been applied.

A flag indicating whether the adjustment has been applied is present in the files and the uncertainty of the bias correction is included in the total uncertainty. For lakes where the flag is not set, the

impact of changes in sensor on the long-term trends in LSWT is less well constrained, and trends should be treated with caution.

4.3 Quality assessment

The quality assessment exercise is carried out mainly comparing the retrieved LSWTs with independent in situ measurements. An in-situ database has been compiled and is updated towards the end of each year. Quality control checks are performed on the in-situ data ranging from unrealistic values to comparison with the climatology together with its variability. The lakes where in situ data are available are distributed globally although European and especially North American lakes are the most monitored. The assessment of the differences between reference data and satellite LSWT is carried out using robust statistics which is resistant to outliers and bad data in both satellite and in situ measurements. Each LSWT is accompanied by its uncertainty which will be validated using independent reference data as well.

4.4 Summary of the strengths, weaknesses and limitations

Strengths

- The retrieval of LSWT is based on physics which gives good reason to expect stable performance across domains in time and space that cannot be directly easily validated
- Estimation of the LSWT retrieval uncertainty at pixel level
- Quality levels assigned at pixel levels which summarise the confidence in the LSWT and its uncertainty. They are assigned on the base of the chi2 of the OE retrieval, the water detection score, the closeness to the shore, the satellite zenith angle, and the sensitivity to the prior.

Weakness

- Currently, only LSWT has been retrieved only during daytime. Adding nighttime retrievals would improve the data coverage but also nighttime LSWT are more stable because not influenced by insolation
- The water detection algorithm which is used for detecting water in presence of clouds relies on threshold tests which are applied to visible channels and combinations. Consequently, the thresholds depend on water type and each threshold may be different for each water type. Also, the thresholds depend on wind and satellite zenith angle. In this version of the water detection algorithm a threshold for all the lakes has been derived and utilised

Limitations

- Cloudiness limits the retrieval using infrared/visible channels. Therefore, some parts of the globe have much less coverage due to high cloud cover.
- Resolution of meteorological satellite is ~1km therefore smaller lakes are excluded from the retrieval

4.5 References

Bulgin, C. E. Embury, O. Corlett, G. and Merchant, C. J. (2016a) Independent uncertainty estimates for coefficient-based sea surface temperature retrieval from the Along-Track Scanning Radiometer instruments. Remote Sensing of Environment, 178. pp. 213-222. ISSN 0034-4257 doi:10.1016/j.rse.2016.02.022

Bulgin, C. E. Embury, O. and Merchant, C. J. (2016b) Sampling uncertainty in gridded sea surface temperature products and Advanced Very High-Resolution Radiometer (AVHRR) Global Area

Coverage (GAC) data. Remote Sensing of Environment, 117. pp. 287-294. ISSN 0034-4257 doi:10.1016/j.rse.2016.02.021

Carrea, L. Embury, O. and Merchant, C. J. (2015a) Datasets related to in-land water for limnology and remote sensing applications: distance-to-land, distance-to-water, water-body identifiers and lake-centre co-ordinates. Geoscience Data Journal, 2(2). pp. 83-97. ISSN 2049-6060 doi:10.1002/gdj3.32

Carrea, L. ; Embury, O. ; Merchant, C. J. (2015b): GloboLakes: high-resolution global limnology dataset v1. Centre for Environmental Data Analysis, 21 July 2015. doi:10.5285/6be871bc-9572-4345-bb9a-2c42d9d85ceb

Carrea, L. ; Merchant, C. J. (2019): GloboLakes: Lake Surface Water Temperature (LSWT) v4. 0 (1995-2016). Centre for Environmental Data Analysis, 29 March 2019. doi:10.5285/76a29c5b55204b66a40308fc2ba9cdb3.

MacCallum, S. N. and Merchant, C. J. (2012) Surface water temperature observations for large lakes by optimal estimation. Canadian Journal of Remote Sensing, 38(1). pp. 25-45. ISSN 1712-7971 doi:10.5589/m12-010

[D1] GHRSST data specification;
https://www.ghrsst.org/wpcontent/uploads/2016/10/GDS20r5.pdf

5 Lake water-leaving reflectance – LWLR

5.1 Description

Lake water-leaving reflectance is the atmospherically corrected ratio of water-leaving radiance relative to downwelling irradiance, corrected for viewing and sun angle effects. LWLR describes the apparent colour of the water body irrespective of illumination conditions and under the assumption that the water is optically deep. The representation of lake colour is typically a reflectance spectrum, where the shape and amplitude are characteristic of biogeochemically relevant substances, and the efficiency of absorbing sunlight for photosynthesis as well as warming of the surface water column, a property which determines the depth of mixing.

Under the additional assumption that the water column is vertically homogeneous over the depth where solar radiation interacts, LWLR may be interpreted using physics-based or empirical algorithms to estimate the concentration of coloured dissolved and suspended materials, including sediment and plankton. In the context of modelling studies, these biogeochemically relevant variables correspond to state variables in biogeochemical models, providing an opportunity for data assimilation in the observed surface layer. In the context of water management, the abundance of phytoplankton is key to preserving good water quality status, and turbidity may be used alongside bathymetry to determine the extent of benthic habitats, for example.

LWLR processing inherits the *Calimnos* processing chain initially developed for the UK- GloboLakes project, in part based on the first global inland waterbodies processing chain using a comprehensive library of algorithms and resultant products in the ESA Diversity-2 project. These processing chains were built to process archived ENVISAT-MERIS data at full resolution (300m).

Calimnos has seen continuous development in H2020 TAPAS, H2020 EOMORES, the Copernicus Land Monitoring Service (CLMS) and Lakes_cci, from core collaborative efforts between PML, University of Stirling, Brockmann Consult and HYGEOS. It is presently used to deliver the *CLMS – Lake water quality* products (LWLR, Turbidity, Trophic State Index) at 10-day aggregation intervals. For CLMS, archived MERIS full resolution data are available from *Calimnos* v1.1 whereas operational processing of Sentinel-3 OLCI uses *Calimnos* v2.0 and Sentinel-2 MSI scenes are being processed for selected regions using *Calimnos* v1.5. The incremental versions represent evolutions of the process chain to handle newly introduced satellites, as well as updated dependencies such as POLYMER for atmospheric correction or Idepix for land/cloud/water masking. Major version numbers represent changes accompanied by algorithm round-robin selection and calibration. The v1.5 evolution for the MSI sensor additionally saw algorithm adjustments to calibrate MSI products against OLCI, whilst support for MODIS-Aqua was also added with v1.5 as part of the Lakes_cci. Due to observed limitations in using MODIS across a global set of lake targets, extension of the data record to SeaWiFs has lower priority and is not yet discussed in this document.

Lakes_cci has introduced per-pixel product uncertainty estimates and algorithms for LWLR and chlorophyll-a for MODIS-Aqua since v1.5 of the processing chain, first delivered as part of CRDP v2.0. For CRDP v3.0.0, support has been added for the MERIS 4th reprocessing format, and a new initialisation condition in Polymer v4.15 and upwards is adopted, yielding a wider output range to better resolve highly turbid water types while also requiring updates to quality control procedures and flags. Per-sensor and OWT algorithm optimisation and uncertainty characterisation has been updated to support the latest improvements in atmospheric correction. Two products have been added to CRDP v3.0.0 to support climate modelling, being the Coloured Dissolved Organic Matter (CDOM) light absorption coefficient as a proxy of the dissolved organic carbon pool, and the vertical diffuse light attenuation coefficient (K_d) to support underwater light climate characterisation for

primary production studies. Finally, processing efficiency has been greatly improved across the pixel identification, atmospheric correction and subsequent algorithm processing steps.

Calimnos is a processing chain with many stages, each of which are described in documents referred to in the following sections as relevant. The algorithms that form the core of atmospheric correction and retrieval of water column optical properties are based in published literature and/or documentation of Lakes_cci and CLMS, whereas algorithm-specific tuning and their assignment to specific optical water types is unique to *Calimnos* as first described in Neil et al. (2019) and extended to uncertainty characterisation is detailed in Liu et al. (2021). The algorithm basis described here is equivalent to the ATBD provided for CLMS, with algorithm evolution and new elements for lakes cci specified in additional detail.

5.2 Algorithm definition

Calimnos combines data discovery, subsetting by target area (individual water bodies), radiometric and atmospheric corrections, pixel identification (land/cloud/water/ice), optical water type classification, individual algorithms (per variable and water type), algorithm blending, conversion and aggregation into a single processing chain. The processes are run exclusively with optical imagery using visible and near infrared wavebands, and short-wave infrared where available.

A schematic overview of *Calimnos* is given in Figure 6. The main processing stages and their corresponding algorithms are given below.

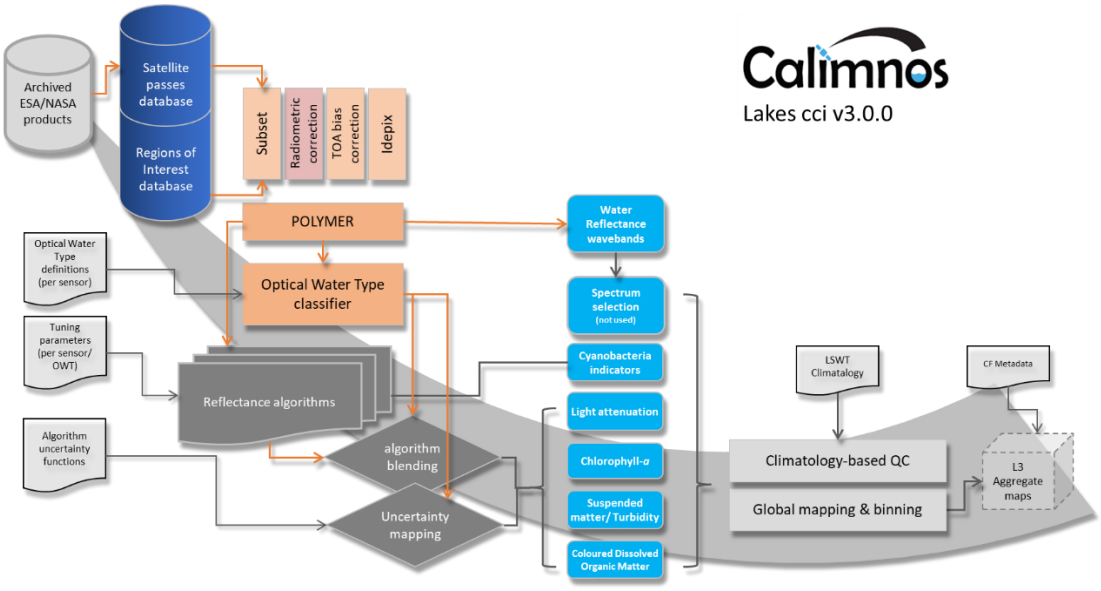

Figure 6: Schematic overview of the Calimnos processing chain v3.0 for LWLR, chlorophyll-a and turbidity or suspended matter, and candidate products for cyanobacteria, light attenuation and Coloured Dissolved Organic Matter.

To produce Lake Water-Leaving Reflectance:

- Data discovery. Following download of new satellite passes at L1A or L1B these are entered into a geospatial database. Target regions are similarly specified in a geospatial database and satellite products which overlap any of the target regions are queued for processing. In the context of re-processing, any duplicate passes are removed. The procedure relies on in-house python scripts and postgres database functionality. For MERIS both the full and

reduced resolution archives are checked for matches, with the full resolution selected when and where available.

- Subsetting. For best processing performance, satellite passes are cropped to bounding boxes. This is done in two stages. First, a 30-km buffer is included around each target area to ensure clouds that may cast shadow on the target area, can be identified. Following the pixel identification step (see below), the cropped area is further reduced, normally by 10% in area around the target. The subsetting routine is part of the SNAP toolbox, called through the Graph Processing Tool (GPT).
- Geographic correction. MODIS-Aqua L1A scenes are converted to L1C using the l2gen processor. The L1C file format is defined for the CCI (Ocean Colour and Lakes) and bundles all auxiliary data and accurate geo-location.
- Pixel identification. The *Idepix* neural network routine is applied for initial pixel identification as water, land, cloud/haze, or snow/ice. *Idepix* is called through SNAP using the GPT. Pixel identification masks are stored for later masking of invalid (non-water) pixels.
- Atmospheric correction. POLYMER is applied to the corrected L1B data of MERIS and OLCI, and L1C MODIS-Aqua, and yields water-leaving reflectance wavebands. Sensor gain corrections (SVC gains) are applied in the same step. The outputs are fully normalized water-leaving reflectance per waveband. POLYMER is called using a function wrapper in Python.

To produce derived water-column properties (total suspended matter (TSM), concentrations of chlorophyll-a, light absorption by Coloured Dissolved Matter, vertical attenuation and cyanobacteria indicators):

- Optical water type classification. The optical water type (OWT) classification developed in the GloboLakes project (Spyrakos et al. 2018) is applied to each pixel to determine the similarity of the observed water-leaving reflectance spectrum to thirteen known types. The same set of OWTs is used with MERIS/OLCI and MODIS wavebands. From CRDP v2.1 onwards, additional mixed-water types are added to identify interference from adjacent land (Jiang et al. 2023).
- Algorithm mapping and blending. For each of the 13 base OWTs a best-performing algorithm (see section 5.2.1) has been selected and tuned against in situ data sets, individually per satellite sensor. For some products, one algorithm configuration may serve several Optical Water Types (details further below). The best-performing algorithms were selected based on atmospherically corrected satellite data, using subsets of the dataset with relatively high OWT membership scores to perform algorithm tuning per OWT (typically the 80 % most-similar LWLR data points were used). Insofar as inter-sensor bias corrections are not already corrected within the top-of-atmosphere product or atmospheric corrections, this tuning step compensates for bias against in situ reference data per algorithm, optical water type and sensor. Where no suitable algorithm/OWT combination is found, no algorithm is assigned and reported values are either missing or derived from the remaining OWT class membership fraction for which algorithms were available. All algorithms were re-calibrated following an upgrade of the atmospheric correction processor for v3.0 of the Lakes_cci dataset.

For uncertainty characterization:

- Uncertainty mapping. The uncertainty mapper uses results from in situ validation, separated by OWT, to produce bias and root-mean-square uncertainties per pixel. A predetermined set of uncertainty functions expresses, per output product (LWLR or derived water constituent concentrations), any non-linearity in product uncertainty as a function of (for the time being) optical water type membership. It should be noted that the uncertainty models do not account for all observation effects, notably atmospheric composition and related land-adjacency effects.

For merged lakes (L3S) ECV product format consistency:

- Aggregation. Aggregation is done on a per-lake basis using all imagery available on a given day, after applying masks to select data for water pixels. When multiple LWLR products are available for a given day, preference is given to the MERIS or OLCI derived cloud-free results. i.e. MODIS spectra are not used. The aggregated products which contain the LWLR, chlorophyll-a and turbidity variables are then mapped to a global grid according to Lakes_cci specifications. Observations closest to solar noon are selected in case multiple observations are acquired on the same day. This mostly affects high-latitude areas.
- Mosaicking. For consistency with other thematic lakes cci variables, the products are combined on a global grid extending from -180 to 180° longitude and -90 to 90° latitude.

Lakes selection

- All lakes_cci targets for which data are retrieved with MERIS or OLCI are included in the dataset. MODIS-Aqua data are included only for water bodies where temporal consistency checks do not show a sensor-specific response. Typically, these are large lakes which are less subject to land adjacencies.

Climatologic filtering

From CRDP v2.1, a climatology-based quality control procedure is implemented during the L3 reprojection and aggregation phase, to improve consistency with the LWST and LIC products. This procedure identifies unrealistic LWLR retrieval co-occurring with (sub-pixel or thin) ice cover. Algorithm assumptions and known limitations

The following assumptions relating to individual algorithms are core to the performance of the processing chain for LWLR and derived substance concentrations:

- *Idepix* can differentiate adequately between pixels containing water and any of the following conditions: mixed land/water, cloud, cloud shadow, ice, snow, and haze.
- *POLYMER* successfully retains the shape and amplitude of water-leaving reflectance.
- The Optical Water Type classification sufficiently captures the diversity of natural water types so that the most appropriate algorithms can be used and tuned to remove systematic bias.
- Tuning of reflectance algorithms for chlorophyll-*a* and turbidity is adequate for each water type and based on sufficient in situ data availability to achieve statistical rigour.

5.2.1 Specific algorithms for LWLR

5.2.1.1 Pixel geolocation

For MERIS (from the 4th reprocessing) and OLCI, no processing step for improving the geolocation position is required. The accuracy is given by ESA with 0.2 – 0.7 pixels for processing version 2.23 and <0.1 pixel for processing version 2.29.

For MODIS Aqua, a GEO file is generated based on satellite attitude and ephemeris data provided by NASA, to produce L1C data as input to further processing.

5.2.1.2 Radiometric corrections

OLCI-A is the reference system for inter-sensor bias corrections, because it has the largest number of spectral bands and benefits from a larger vicarious calibration network than any earlier sensor. A per-band system vicarious gain correction is currently available for use with POLYMER.

For MERIS, the coherent noise equalization method reduces detector-to-detector and camera-to-camera systematic radiometric differences and results into a diminution of the vertical striping observed on MERIS L1b products following the algorithm developed by Bouvet and Ramino (2010);

coefficients for each detector line are retrieved from MERIS archive over ice. Another step for radiometric improvements is the smile correction, which corrects for the small variations of the spectral wavelength of each pixel along the image by the estimation of the reflectance spectral slope from the measurements in two neighbouring bands. POLYMER uses actual pixel wavelength, so smile correction is not used in this processing chain.

For MERIS and MODIS, sensor-specific bias corrections, including any known system vicarious calibration gains, are applied within the POLYMER atmospheric correction step.

Additional bias corrections and waveband-shifting are not considered at present due to the lack of a theoretical framework to resolve differences across all wavebands and optical water types found in lakes.

5.2.1.3 Pixel identification

The cloud detection function of the Idepix algorithm (by Brockmann Consult) was used in several processing chains, e.g. those used in CoastColour L1P and Diversity II. Due to the good performance of Idepix cloud screening in these applications, it is also selected for *Calimnos*. Idepix is based on a cloud probability derived from a neural net which has been trained with >60,000 manually classified pixels and which is combined with a number of additional tests on e. g. brightness, whiteness, glint. After clouds have been identified, a buffer can be defined in order to provide for a safety margin along cloud borders. This buffer radius (in pixel) can be configured and is set to 2 pixels.

Validation is performed by applying the PixBox Validation, a procedure where manually selected pixels are categorized to different categories and characterized with expert knowledge, e. g. to clear land, clear water, totally cloudy, semi-transparent cloud, cloud shadow, snow/ice, etc. A set of 17k MERIS FR pixels was collected in the scope of the CoastColour project, and detailed validation results are provided in the corresponding report (Ruescas et al. 2014).

Retrieval of water quality parameters is also strongly influenced by the occurrence of cloud shadow, which need to be identified and eliminated from further processing. Potential cloud shadow areas are identified by the geometry of the sun angle, viewing angle and the cloud height and the cloud bottom. The cloud height is gained by either the pressure or the temperature, but if this information is missing (not all sensors offer the respective bands), a maximum cloud height needs to be defined. The most difficult prediction is the height of the cloud base as it is not seen by the sensor. In Idepix it is defined as the minimum cloud height detected within the respective cloud minus an offset. Basis of good cloud shadow detection is a good cloud detection. Validation of the cloud shadow detection is done by visual inspection of different images under different conditions (cloud types and geometries). When the observation target is at the edge of the swath in the direction of the sun position, cloud shadows cast by clouds outside the scene may not be recognised.

In general, the most progressive combination of available cloud masks is selected, favouring accuracy over observation coverage.

5.2.1.4 Atmospheric correction

POLYMER versions 4.17is used to produce CRDP v3.0.0. The atmospheric correction processor was initially designed to resolve water-leaving reflectance in clear ocean waters including areas affected by sun glint (Steinmetz et al. 2011). The versatility of the processor to deal with bright waters has tested positively with a variety of optically complex (including inland) waters compared to alternative processors (Qin et al. 2017, Warren et al. 2019). POLYMER applies a spectral optimization based on bio-optical model in conjunction with radiative transfer models to separate

atmospheric (including glint) and water reflectance. The principle of the algorithm is a spectral matching method using a polynomial to model the spectral reflectance of the atmosphere and sun glint, and a bio-optical forward reflectance model for the water part. The algorithm uses a user-selectable set of wavebands as opposed to alternative ocean-colour methods that primarily extrapolate from near infra-red bands. The output is fully normalized water-leaving reflectance, referred to as LWLR in the context of Lakes_cci.

Configuration:

- POLYMER according to Steinmetz et al. (2011), updated in Steinmetz (2016 and 2018), parameterized to use the Park and Ruddick (2005) bidirectional reflectance distribution function and operating only on pixels identified as water by the *Idepix* module (masks generated by POLYMER are not used). From v4.15 and upwards, a broad range of initialisation conditions is used to allow a variable mineral component to contribute to particle scattering. Bounds for the chlorophyll-a concentration and and the scattering coefficient f_b are set to 0.01 – 1000 mg m^{-3} Chl-a and -3 to 3, respectively. All available visible, near-infrared and shortwave-infrared wavebands are used, except for bands in the 400-412 nm region.

5.2.1.5 Specific algorithms for derived water quality products

5.2.1.5.1 Optical water type (OWT) membership

The OWT classification module was written at PML based on the work of Moore et al. (2001) and equivalent software developed for ESA Ocean Colour cci. The algorithm used for lakes relies on a spectral library (spectral means) defined in the GloboLakes project by the University of Stirling (Spyrakos et al. 2018). In contrast to OWT mapping used in earlier versions of *Calimnos*, CLMS and Lakes_cci adopt the spectral angle (Kruse et al. 1993) rather than Mahalonobis distance as metric for similarity between observations and type spectra. The spectral angle is here defined over a range of 0 to 1 where 1 implies identical spectra.

5.2.1.5.2 Weighted tuning procedure

An upgraded per-OWT tuning procedure was adopted for CRDPv3.0 compared to earlier versions. Specifically, For each Optical Water Type, algorithms are individually tuned using only the matchups corresponding to the 80% highest spectral similarity with a given OWT, rather than the full dataset.

The weight of each matchup in the tuning process is calculated by its membership scores as:

$$W_i=(S_i-S_{min})/(S_{max}-S_{min})$$

This ensures that matchups with higher spectral similarity to the specific OWT play a more significant role in the tuning process, thereby enhancing the relevance and accuracy of the tunning process for each OWT.

Selected algorithm parameters for each of the OWT are tuned against data held in LIMNADES (no longer accessible) and GLORIA databases. This procedure also accounts for any uncertainties that stem from systematic bias in the retrieval of water-leaving reflectance from POLYMER, to the extent that they are represented in the in situ data. This whole-chain validation is applied to each algorithm in *Calimnos*, recognizing the fact that the most prominent error in inland water quality retrieval is the atmospheric correction step. It is noted that validation data for relatively clear inland waters are very scarce.

5.2.1.5.3 Water constituent algorithms

Weighted blending: Water constituent retrieval algorithms tuned to each OWT (Spyrakos et al. 2018, Neil et al. 2019) are mapped to individual pixels from the OWTs with the three highest

classification scores for that pixel. The algorithm results corresponding to those three OWTs are averaged using the membership score as weighting factor, after normalizing the scores between 0 and 1 where 1 is the highest score and 0 is the score of the 4th ranking OWT. This procedure is used to derive maps of total suspended matter (TSM) and chlorophyll-*a* (Chla) without discontinuities at the edge of the applicable range of any single algorithm.

Uncertainty mapping: to propagate product uncertainty from the individual algorithms, the weighted OWT membership score is again used, in combination with a set of uncertainty functions resulting from in situ algorithm validation. The uncertainty functions describe product uncertainty as a function of OWT membership score and target substance concentration (where relevant). The per-OWT uncertainties are weighted according to OWT-membership to allow propagation to the final product. Where in situ data are lacking in lakes to determine product uncertainties (e.g. in the case of a specific OWT, substance concentration range or sensors), and uncertainty cannot be provided this value is set to the no-data value.

5.2.1.5.4 Chlorophyll-a algorithms

5.2.1.5.4.1 Chlorophyll-a algorithms for MERIS

Table 4 lists the mapping of Chla algorithms to the OWTs defined in Spyrakos et al. (2018). Each algorithm is tuned to one or more OWTs, and the algorithms set out below are those selected for MERIS after extensive product validation in the Lakes_cci project.

Table 4 Chlorophyll-a algorithm selection per Optical Water Type for MERIS

Optical water type number	Algorithm source	Algorithm optimization
1, 7, 8, 10	QAA_TC2, adapted QAA algorithm according to Liu et al. (2020)	Per-OWT tuned algorithm applied to Polymer atmospherically corrected reflectance based on Lakes_cci calibration, against Limnades and GLORIA datasets.
2, 3, 6, 9, 11, 13	OCI https://www.earthdata.nasa.gov/apt/documents/chlor-a/v1.0#mathematical_theory	
4, 12	Switched blending algorithm by Smith et al. (2018)	
5	OC4 https://www.earthdata.nasa.gov/apt/documents/chlor-a/v1.0#mathematical_theory	

Following are the details of the selected Chla algorithm for MERIS, with the per-OWT tuned algorithm parameters listed in Table 5.

- QAA_TC2 algorithm

The Liu et al. (2020) algorithm, referred to as QAA_TC2, implements the Quasi-Analytical Approach (QAA), following emperical tuning to separate the total non-water absorption at 665 nm ($a_{nw}(665)$) into phytoplankton absorption ($a_{ph}(665)$) and yellow matter ($a_{ym}(665)$), which combines coloured dissolved matter (CDOM) and detritus.

To implement the QAA_TC2 algorithm, the fully normalized water-leaving reflectance ($R_w(\lambda)$, λ= 443, 560, 665, 709 and 754nm) is first converted to below-surface remote-sensing reflectance ($rrs(\lambda)$) as follows:

$$rrs(\lambda) = \frac{R_{rs}(\lambda)}{0.52+1.7\times R_{rs}(\lambda)} \quad [5.1]$$

Where $R_{rs}(\lambda) = R_w(\lambda)/\pi$.

The ratio of backscattering to the sum of backscattering and absorption, $\mu(\lambda)$, which according to the work by Gordon et al. (1988) can be obtained from below-surface remote-sensing reflectance *rrs*(λ) as:

$$u(\lambda) = \frac{-g_0 + \sqrt{g_0^2 + 4 \times g_1 \times rrs(\lambda)}}{2 \times g_1} \quad [5.2]$$

Where g_0 = 0.089 and g_1 = 0.125.

The backscattering coefficients ($b_{bp}(\lambda_0)$, $\lambda_0 = 709 \text{ or } 754\text{nm}$) of particulates at the reference band (λ_0) can be then calculated as:

$$b_{bp}(\lambda_0) = \frac{\mu(\lambda_0) a_w(\lambda_0)}{1 - \mu(\lambda_0)} - b_{bw}(\lambda_0) \quad [5.3]$$

The reference wavelength, λ_0, is determined based on the calculated Maximum Chlorophyll Index (MCI) using the equation below. If the calculated MCI ≤ 0.0016, λ_0 is set to 709 nm; otherwise, λ_0 is set to 754 nm. Here, $a_w(\lambda_0)$ and $b_{bw}(\lambda_0)$ represent the absorption coefficient and backscattering of pure water at the reference band λ_0, respectively. Specifically, $a_w(709) =$ 0.80210 m^{-1}, $a_w(754) = 2.86700$ m^{-1}, $b_{bw}(709) = 0.00030$ m^{-1}, $b_{bw}(754) = 0.00023$ m^{-1}.

$$\text{MCI} = R_{rs}(709) - R_{rs}(665) - (R_{rs}(754) - R_{rs}(665)) * \left(\frac{709-665}{754-665}\right) \quad [5.4]$$

The power-law exponent *Y* of backscattering coefficients of particulates can be then obtained following:

$$\text{Y} = 2.0\left(1 - 1.2exp\left(-0.9\frac{r_{rs}(443)}{r_{rs}(560)}\right)\right) \quad [5.5]$$

The backscattering coefficients of particulates at other bands $b_b(\lambda)$ can be then calculated by:

$$b_b(\lambda) = b_{bp}(\lambda_0)\left(\frac{\lambda_0}{\lambda}\right)^Y + b_w(\lambda) \quad [5.6]$$

The total non-water absorption coefficients ($a_{nw}(\lambda)$) could then be obtained by subtracting the pure water absorption from the total absorption coefficients following:

$$a_{nw}(\lambda) = \frac{(1-\mu(\lambda)) b_b(\lambda)}{\mu(\lambda)} - a_w(\lambda) \quad [5.7]$$

The absorption coefficients of phytoplankton at 665nm ($a_{ph}(665)$) can then be obtained as:

$$a_{ph}(665) = a_{nw}(665) - \eta a_{nw}(560) - (1-\eta) a_{nw}(709)$$

Where η = 0.17. The specific phytoplankton absorption coefficients at 665nm ($a^*_{ph}(665)$) is empirically tuned for each OWT using in *Calimnos*. The final Chla product is then obtained after a fine-tuned power-law conversion. The tuned parameters of $a^*_{ph}(665)$, *A*, *B* and *C* used in Calimnos for each OWT are listed in Table 5:

$$Chla = A * \left(\frac{a_{ph}(665)}{a^*_{ph}(665)}\right)^B + C \quad [5.8]$$

- OC4 algorithm

The OC4 algorithm, originally formulated to retrieve chlorophyll-a concentration from relatively clear ocean waters where phytoplankton and other optically active substances covary, relies on a ratio of blue and green wavebands. The algorithm is formulated as:

$$log(Chla_{oc4}) = a_0 + (a_1 x) + a_2 x^2 + a_3 x^3 + a_4 x^4 \quad [5.9]$$

where x is the reflectance band ratio:

$$x = log\ \frac{R_w(\lambda_{blue})}{R_w(\lambda_{green})} \quad [5.10]$$

The λ_{blue} corresponds to the band which shows the highest R_w value among bands 443, 489 and 510 nm. The λ_{green} is band 560 nm.The per-OWT tuned algorithm coefficients used in *Calimnos* are listed in Table 5.

- OCI algorithm

The OCI algorithm is a combination of the OC4 band ratio algorithm by O'Reilly & Werdell, (2019) and the colour index (CI) by Hu et al., (2019). The blending of CI and OC4 Chla products is based on the method described by Hu et al. (2019), which combines an empirical band difference approach at low Chla concentrations with a band ratio approach at higher Chla concentrations. For application to MERIS and OLCI, the CI algorithm is defined as:

$$CI = R_{rs}(560) - (R_{rs}(443) + \frac{560-443}{665-443} * (R_{rs}(665) - R_{rs}(443))) \quad [5.11]$$

Where $R_{rs}(\lambda) = R_w(\lambda)/\pi$. R_w is the fully normalized water-leaving reflectance. Chla concentration is then derived from CI as:

$$Chla_{CI} = 10^{(m+n*CI)} \quad [5.12]$$

Where *m* and *n* are per-OWT tuned in *Calimnos*, as listed in Table 5.

For Chla retrievals below 0.25 mg m^{-3}, the CI algorithm is used. For Chla retrievals above 0.35 mg m^{-3}, the OC4 algorithm is used. In between these values, the CI and OC4 algorithm are blended using a weighted approach:

$$Chla = \frac{Chla_{CI}(t_2 - Chla_{CI})}{t_2 - t_1} + \frac{Chla_{OC4}(Chla_{CI} - t_1)}{t_2 - t_1} \quad [5.13]$$

with t_1 = 0.25, and t_2=0.35 (edges of the blending region).

- Switched blending algorithm

The Smith et al. (2018) algorithm is a weighted blending of Gilerson et al. (2010) and OCI algorithms. The Gilerson et al. (2010) algorithm is more applicable over moderate to high biomass waters, which is defined as:

$$Chla_{Gilerson} = ((\left(A \times \frac{R_w(708)}{R_w(665)}\right) - B)^C \quad [5.14]$$

The coefficients A, B and C used in *Calimnos* for each OWT are shown in Table 5.

In the transition range, the Chla outputs from Gilerson et al. (2010) and OCI algorithms are blended using a weighted approach:

$$Chla = \alpha_1 * Chla_{Gilerson} + \alpha_1 * Chla_{OCI} \quad [5.15]$$

Where α_1=($\emptyset - 0.75$)/(1.15-0.75); α_2=(1.15-$\emptyset$)/(1.15-0.75); and $\emptyset = R_w(708)/R_w(665)$.

Table 5 Chlorophyll-a algorithms and tuned coefficients per optical water type for MERIS

OWT	Assigned Algorithm	Per-OWT Tuned Coefficients
1	QAA_TC2	a^*_{ph} (665)= 0.015002, A=1.0015, B=0.9064, C=3.4885
2	OCI	a_0=0.2354, a_1=-3.5980, a_2=3.1732, a_3=-0.7902, a_4=-0.6487, m=-0.4631, n=134.1613
3	OCI	a_0=0.2279, a_1=-3.3788, a_2=3.1732, a_3=-1.4674, a_4=-0.3493, m=-0.3436, n=134.1613
4	Switched-blending algorithm	a=25.2811, b=18.1938, c=0.9440, a_0=0.2279, a_1=-2.7420, a_2=1.7214, a_3=-0.7902, a_4=-0.6487, m=-0.3436, n=134.1613
5	OC4	a_0=0.2974, a_1=-3.1806, a_2=3.7664, a_3=-0.5268, a_4=-0.6878
6	OCI	a_0=0.2279, a_1=-3.5742, a_2=3.1731, a_3=-1.467, a_4=-0.3493, m=-0.3436, n=134.1613
7	QAA_TC2	a^*_{ph} (665)=0.0119, A=1.0096, B=0.8628, C=2.66
8	QAA_TC2	a^*_{ph} (665)=0.0119, A=1.0297, B=0.8589, C=2.5905
9	OCI	a_0=0.2279, a_1=-3.4395, a_2=3.1732, a_3=-1.4674, a_4=-0.3493, m=-0.3436, n=134.1613
10	QAA_TC2	a^*_{ph} (665)=0.0119, A=1.0198, B=0.86, C=2.9542
11	OCI	a_0=0.2558, a_1=-3.5980, a_2=3.1732, a_3=-0.7902, a_4=-0.6487, m=-0.4631, n=134.1613
12	Switched-blending algorithm	a=25.1975, b=18.1336, c=0.9442, a_0=0.2279, a_1=-2.7441, a_2=1.709, a_3=-0.7902, a_4=-0.6487, m=-0.3436, n=134.1613
13	OCI	a_0=0.2285, a_1=-3.3766, a_2=3.1732, a_3=-1.4674, a_4=-0.3493, m=-0.3436, n=134.1613

5.2.1.5.4.2 Chlorophyll-a algorithms for OLCI

Table 6 presents the mapping of Chla algorithms for OLCI to specific OWTs from Spyrakos et al. (2018). Each algorithm is tuned and assigned to one or more OWTs, following extensive product validation for CRDP v3.0.

Table 6 Chlorophyll-a algorithms per optical water type for OLCI

Optical water type number	Algorithm source	Algorithm optimization
1, 8, 9	MDN https://github.com/ryan-edward-oshea/MDN_V2	Per-OWT tuned algorithm applied to Polymer atmospherically corrected reflectance based on Lakes_cci calibration, against the Limnades and GLORIA datasets.
2	BNN https://github.com/mowerther/BNN_2022	
3, 13	OC2 https://www.earthdata.nasa.gov/apt/documents/chlor-a/v1.0#mathematical_theory	
4, 5, 6, 11, 12	Switched blending algorithm by Smith et al. (2018)	
7,10	R708_665, empirical band ratio based on Gilerson et al. (2010)	

- MDN

The Mixture Density Network (MDN), a machine-learning model, was trained and validated using a large database of co-located in situ Chla measurements and satellite observations (Pahlevan et al., 2020). There is significant overlap in this training data set with the matchup databases used to tune other algorithms in *Calimnos,* and this trained model was not further tuned for CRDP v3.0. The algorithm was obtained from https://github.com/ryan-edward-oshea/MDN_V2.

- BNN

The Bayesian Neural Networks (BNNs) is also a machine-learning based algorithm, built using an extended *in situ* dataset of oligo- and mesotrophic water bodies in Werther et al. (2022), including relevant samples from LIMNADES. The original algorithm and parameters were adopted in *Calimnos* for CRDP v3.0 from https://github.com/mowerther/BNN_2022.

- OC2 algorithm

The OC2 algorithm, originally formulated to retrieve chlorophyll-a concentration from relatively clear ocean waters where phytoplankton and other optically active substances covary, relies on a ratio of blue and green wavebands. The algorithm is formulated as:

$$log(Chla_{oc2}) = a_0 + (a_1 x) + a_2 x^2 + a_3 x^3 + a_4 x^4 \quad [5.16]$$

where x is the reflectance band ratio:

$$x = log\ \frac{R_w(\lambda_{490})}{R_w(\lambda_{560})} \quad [5.17]$$

The per-OWT tuned algorithm coefficients used in *Calimnos* are listed in Table 7.

- Switched-blending algorithm

The application procedure of the switched blending algorithm by Smith et al. (2018) is as described in the section for MERIS, with per-OWT tuned algorithm coefficients listed in Table 7.

- R708_665

The R708_665 algorithm by Gilerson et al. (2010) is an empirically tuned ratio of 708 and 665 nm wavebands. The tuning of the algorithm is revised in *Calimnos*, by calibrating against the LIMNADES

and GLORIA datasets which are much larger than the dataset used in the original publication. The final configuration is also a highly simplified form of the original algorithm:

$$Chla_{Gilerson} = (\left(A \times \frac{R_w(708)}{R_w(665)}\right) + B)^C \quad [5.18]$$

Where *A, B* and *C* are tuning coefficients empirically calibrated for each OWT in *Calimnos* (Table 7). *R*(λ) is the reflectance (irrespective of whether it is expressed above or below water and normalized for viewing geometry or not) at waveband λ.

Table 7 Chlorophyll-a algorithms and tuned coefficients per optical water type for OLCI

OWT	Assigned Algorithm	Per-OWT Tuned Coefficients
1	MDN	Not applied
2	BNN	Not applied
3	OC2	a_0=0.1212, a_1=-4.2822, a_2=-0.3934, a_3=3.1506, a_4=-2.1014
4	Switched-blending algorithm	a_0=0.1001, a_1=-6.6148, a_2=-10.8148, a_3=-3.7905, a_4=0.9988, m=-0.2767, n=1062.3917, A=35.8687, B=22.3873, C=0.9116
5	Switched-blending algorithm	a_0=0.0865, a_1=-5.3237, a_2=-5.0588, a_3=-5.6914, a_4=-0.8829, m=-1.4848, n=421.8537, A=54.4613, B=26.8897, C=0.8222
6	Switched-blending algorithm	a_0=0.1815, a_1=-3.4529, a_2=3.2158, a_3=-1.2300, a_4=-0.5275, m=-0.9348, n=72.5114, A=31.1194, B=19.2723, C=0.9115
7	R708_665	A=88.8820, B=0.4573, C=-61.1019
8	MDN	Not applied
9	MDN	Not applied
10	R708_665	A=90.3244, B=0.4537, C=-62.2799
11	Switched-blending algorithm	a_0=0.1525, a_1=-5.4944, a_2=-3.0315, a_3=12.4144, a_4=-4.0788, m=0.2178, n=363.4227, A=96.3866, B=111.4691, C=0.7165
12	Switched-blending algorithm	a_0=0.0655, a_1=-5.8495, a_2=-6.2201, a_3=-1.8117, a_4=-0.4015, m=-1.2322, n=258.5630, A=103.8986, B=47.2341, C=0.7143
13	OC2	a_0=0.1212, a_1=-2.7741, a_2=-0.7306, a_3=3.1506, a_4=-2.1014

5.2.1.5.4.3 Chla algorithms for MODIS

For MODIS-Aqua, each selected algorithm was tuned to each OWT for the optimal assignment of algorithms as shown in Table 8. Only matchups corresponding to the top-80% of OWT membership scores were used for the tuning of these algorithms. This is done to improve the overall performance of Chla algorithms across diverse optical properties and to assess the appropriate algorithms and parameterizations for given scenarios, which means although assigned to the same algorithm, different OWTs would adopt different tuned parameterizations. The algorithm selection and assignment presented here is based on extensive product validation conducted for CRDP v3.0.

It is important to note that, due to the absence of several wavebands in MODIS sensors compared to OLCI and MERIS, fewer algorithm formulations are available for comparison. Furthermore, due to having fewer wavebands, OWT classification with MODIS operates in a mathematically compressed space, resulting in fewer distinct water type observations. In other words, relatively fewer algorithms are mapped to a broader set of optical water conditions, resulting in larger product uncertainty.

Table 8 : Chlorophyll-a algorithms per optical water type for MODIS

Optical water type number	Algorithm source	Algorithm optimization
1, 2, 3, 5, 6, 7, 9, 10, 12, 13	OC2 https://www.earthdata.nasa.gov/apt/documents/chlor-a/v1.0#mathematical_theory	Per-OWT tuned algorithm applied to Polymer atmospherically corrected reflectance based on Lakes_cci calibration, against the Limnades and GLORIA datasets.
4, 8, 11	OC3 https://www.earthdata.nasa.gov/apt/documents/chlor-a/v1.0#mathematical_theory	

The OCX algorithms, originally formulated to retrieve chlorophyll-a concentration from relatively clear ocean waters where phytoplankton and other optically active substances covary, relies on a ratio of blue and green wavebands. The algorithm is formulated as:

$$log(Chla) = a_0 + (a_1 x) + a_2 x^2 + a_3 x^3 + a_4 x^4 \quad [5.19]$$

For OC2, *x* is the reflectance band ratio:

$$x = log\ \frac{R_w(488)}{R_w(554)}. \quad [5.20]$$

For OC3, *x* is the reflectance band ratio:

$$x = log\ \frac{min\ (R_w(443), R_w(488))}{R_w(547)} \quad [5.21]$$

R_w is the fully normalized water-leaving reflectance. The tuned algorithm coefficients of OCX algorithms for each OWT are listed in Table 9.

Table 9 : Chlorophyll-a algorithms and tuned coefficients per optical water type for MODIS

OWT	Assigned Algorithm	Per-OWT Tuned Coefficients
1	OC2	a_0=0.3141, a_1=-2.9074, a_2=1.1678, a_3=-1.9763, a_4=0.3784
2	OC2	a_0=0.1755, a_1=-3.0745, a_2=1.6173, a_3=-2.3480, a_4=0.3784
3	OC2	a_0=0.2072, a_1=-3.2178, a_2=1.7435, a_3=-1.9763, a_4=0.3784
4	OC3	a_0=0.2333, a_1=-3.5650, a_2=1.9559, a_3=0.00105, a_4=-0.9175
5	OC2	a_0=0.2650, a_1=-2.8203, a_2=1.6808, a_3=-1.9763, a_4=0.3784
6	OC2	a_0=0.2528, a_1=-2.8726, a_2=1.6758, a_3=-1.9763, a_4=0.3784
7	OC2	a_0=0.2895, a_1=-2.8429, a_2=1.4732, a_3=-1.9763, a_4=0.3784
8	OC3	a_0=0.2046, a_1=-3.5650, a_2=2.3420, a_3=0.00106, a_4=-0.9239
9	OC2	a_0=0.1750, a_1=-3.1022, a_2=1.6029, a_3=-2.4736, a_4=0.3790
10	OC2	a_0=0.2001, a_1=-3.2178, a_2=1.0659, a_3=-1.9763, a_4=0.3784
11	OC3	a_0=0.2296, a_1=-3.5650, a_2=1.9821, a_3=0.0011, a_4=-0.8596
12	OC2	a_0=0.2020, a_1=-2.9164, a_2=1.6713, a_3=-2.7826, a_4=0.3784
13	OC2	a_0=0.3047, a_1=-3.2103, a_2=0.9986, a_3=-1.9763, a_4=0.3784

5.2.1.5.4.4 Turbidity and suspended matter algorithms

Turbidity and total suspended matter (TSM) can be derived from LWLR using wavebands where, ideally, absorption by phytoplankton and dissolved organic matter have minimal influence on reflectance amplitude. Ultimately, turbidity and TSM algorithms rely on empirical relationships between light backscattering and absorption efficiency. As wavelength increases, light absorption becomes more predictable due to the strong absorption properties of pure water at longer wavelengths. Unlike earlier CRDP versions, where these algorithm results were reported in terms of turbidity in nephelometric units, CRDP v3.0 provides the result as the equivalent particle dry weight commonly referred to as Total Suspended Matter (TSM). This change is driven by the availability of more in situ measurements for TSM compared to turbidity, thus providing better characterisation of product uncertainty.

5.2.1.5.4.5 TSM algorithms for MERIS

The TSM algorithms for MERIS are assigned per OWT as shown in Table 10. The algorithms for MERIS were chosen following extensive product validation for CRDP v3.0.

Table 10 TSM algorithms per optical water type for MERIS

Optical water type number	Algorithm source	Algorithm optimization
1	Uudeberg et al. (2020) for turbid water	Per-OWT tuned algorithm applied to Polymer atmospherically corrected reflectance based on Lakes_cci calibration, against the Limnades and GLORIA datasets.
2, 10, 11	Nechad et al.(2006, 2010) at 709nm	
3, 9	Klein et al. (2021)	
4, 13	Nechad et al.(2010, 2016) at 665nm	
5, 8	Nechad et al.(2010, 2016) at 681nm	
6	Binding et al. (2010)	
7, 12	Zhang et al. (2014)	

- Uudeberg-turbid algorithm

The Uudeberg et al. (2020) algorithm for turbid waters is expressed as follows:

$$TSM = A \times \left(R_w(865) - \frac{R_w(779)+R_w(865)}{2}\right) + B \quad [5.22]$$

Where A and B are per-OWT tunned in *Calimnos* (Table 11).

- Nechad algorithm

The Nechad algorithm (Nechad et al. 2010 and 2016) is a single band algorithm which is expressed as follows:

$$TSM = A \times \frac{R_w(\lambda)}{1-\frac{R_w(\lambda)}{C}} \quad [5.23]$$

Where λ is 665, 681 or 709 nm depending on OWT, and A and C values are per-OWT tuned in *Calimnos* (Table 11).

- Klein algorithm

The Klein et al. (2021) algorithm as it is implemented here is based on Nechad et al. (2009) and Dogliotti et al. (2015). The general semi-empirical equation for estimating TSM ($T(\lambda)$) is expressed as:

$$T(\lambda) = A \times \frac{R_w(\lambda)}{1-\frac{R_w(\lambda)}{C}} \quad [5.24]$$

where $R_w(\lambda)$ represents the water-leaving reflectance at wavelength λ, while *A* (in FNU) and *C* are wavelength-dependent constants. According to Dogliotti et al. (2015), TSM derived from the Red band 667 nm ($T(red)$) is used when $R_w(667)$ < 0.05, while $T(nir)$ at band 869nm is used if $R_w(869)$ > 0.07, with a linear transition between these thresholds. The values of *A* and *C* are wavelength-dependent (i.e., A_{red}, C_{red}, A_{nir}, and C_{nir}) and are determined for each OWT accordingly, which are shown in Table 11.

- Binding algorithm

The Binding et al. (2010) algorithm as it is implemented here is based on the analytical inversion of reflectance in the 754 nm band and converting the resultant particulate backscattering signal using a mass-specific backscattering coefficient for suspended matter:

$$TSM\ [g\ m^{-3}] = \frac{a_w(754)\times R_w(754)}{f\times B\times b^*_{TSM}} \quad [5.25]$$

where the absorption by water $a_w(754)$ = 2.8 m^{-1}, the *f* factor is 0.319, the backscattering-to-scattering ratio *B*=0.019. The TSM-specific scattering coefficient b^*_{TSM} is the only coefficient optimised per OWT in *Calimnos*, as listed in Table 11.

- Zhang algorithm

The Zhang et al. (2014) algorithm as it is implemented here is an empirical relation between the 709 nm band and in situ measured suspended matter dry weight, tuned as with the algorithms above:

$$TSM\ [g\ m^{-3}] = A \times (\frac{R_w(709)}{\pi})^B \quad [5.26]$$

where the per-OWT optimized empirical coefficients are listed in Table 11.

Table 11 TSM algorithms and tuned coefficients per optical water type for MERIS

OWT	Assigned Algorithm	Per-OWT Tuned Coefficients
1	Uudeberg2020_Turbid	A=-2311.9624, B=0.0461
2, 10, 11	Nechad_709nm	A=542.2259, C=5.3651
3, 9	Klein2021	A_{red}=226.2059, C_{red}=5.2992, A_{nir}=1618.1759, C_{nir}=5.3397
4	Nechad_665nm	A=357.7859, C=5.3487
5, 8	Nechad_681nm	A=162.7560, C=0.2860
6	Binding	b^*_{TSM}=0.7375
7, 12	Zhang	A=1009.6000, C=0.9891
13	Nechad_665nm	A=141.0442, C=0.2206

5.2.1.5.4.6 TSM algorithms for OLCI

The TSM algorithms for OLCI are assigned per OWT, as shown in Table 12. The algorithm selection for OLCI is based on extensive product validation for CRDP v3.0.

Table 12 TSM algorithms per optical water type for OLCI

Optical water type number	Algorithm source	Algorithm optimization
1, 5	Vantrepotte et al. (2011) algorithm	Per-OWT tuned algorithm applied to Polymer atmospherically corrected reflectance based on Lakes_cci calibration, against the Limnades and GLORIA datasets.
2, 7, 10	Zhang et al. (2014)	
3	Nechad et al.(2010, 2016) at 665nm	
4, 9, 12	Nechad et al.(2010, 2016) at 709nm	
6	Jiang et al. (2021)	
8, 11	Binding et al. (2010)	
13	Nechad et al.(2010, 2016) at 681nm	

The application procedure of the Zhang, Nechad, and Binding algorithms are as described for MERIS, with per-OWT tuned algorithm coefficients listed in Table 13.

- Vantrepotte et al. (2011) algorithm

The Vantrepotte et al. (2011) algorithm as it is implemented here is similar but uses the 665 nm band and an additional empirical factor, which is also tuned to provide the best match for the corresponding water types:

$$TSM\ [g\ m^{-3}] = \frac{A \times R_w(665)}{1 - \frac{R_w(665)}{B}} + C \qquad [5.27]$$

where the empirical coefficients A, B and C are per-OWT optimized against the LIMNADES datasets (Table 13).

- Jiang et al. (2021) algorithm

Jiang et al. (2021) algorithm provides a semi-analytical method for estimating TSM across diverse water bodies. Below is a step-by-step procedure for applying this algorithm:

Step 1: satellite observed water-leaving reflectance (R_w) at bands λ (λ=443, 490, 560, 620, 665, 754 and 865 nm) are converted to remote sensing reflectance (R_{rs}) by dividing by π:

$$R_{rs}(\lambda) = R_w(\lambda)/\pi \qquad [5.28]$$

Step 2: water type classification

Classify the water body into one of four water types based on spectral characteristics:

- Type I: Rrs(490) is greater than Rrs(560).
- Type II: (For pixels which are not classified as Type I), Rrs(490) is less than or equal to Rrs(560), and Rrs(490) is greater than Rrs(620).
- Type III: (For pixels which are not classified as Type I or Type II), Rrs(490) is less than or equal to Rrs(620), and Rrs(754) is less than or equal to 0.01.
- Type IV: (For pixels which are not classified as Type I, Type II or Type III), Rrs(754) is greater than Rrs(490), and Rrs(754) is greater than 0.01.

Step 3: calculation of particulate backscattering coefficient (b_{bp})

For each water type, calculate the particulate backscattering coefficient (b_{bp}) using the following steps:

Calculate the below-surface remote sensing reflectance (rrs):

$$rrs(\lambda) = \frac{R_{rs}(\lambda)}{0.52+1.7\times R_{rs}(\lambda)} \quad [5.29]$$

The ratio of backscattering to the sum of backscattering and absorption, μ(λ), which according to the work by Gordon et al. (1988) can be obtained from below-surface remote-sensing reflectance *rrs*(λ) as:

$$u(\lambda) = \frac{-g_0+\sqrt{{g_0}^2+4\times g_1\times rrs(\lambda)}}{2\times g_1} \quad [5.30]$$

Where g_0 = 0.089 and g_1 = 0.125.

The total absorption coefficient for each water Type can be then determined by:

- Type I: Use the 560 nm band and calculate $a(560)$ as:

$$a(560) = a_w(560) + 10^{-1.146-1.366\times x-0.469\times x^2} \quad [5.31]$$

Where $x = \log\left(\frac{R_{rs}(443)+R_{rs}(490)}{R_{rs}(560)+5\times(\frac{R_{rs}(665)}{R_{rs}(490)})\times R_{rs}(665)}\right)$

- Type II: Use the 665 nm band and calculate $a(665)$ as:

$$a(665) = a_w(665) + 0.39 \times y^{1.14} \quad [5.32]$$

Where $y = \frac{R_{rs}(665)}{R_{rs}(443)+R_{rs}(490)}$

- Type III and IV: For Type III, use the 754 nm band; for Type IV, use the 865 nm band. In both cases, assume $a \approx a_w$.

The backscattering coefficients of particulates, b_{bp}, can be then calculated as:

$$b_{bp}(\lambda) = \frac{u(\lambda)\times a(\lambda)}{1-u(\lambda)} - b_{bw}(\lambda) \quad [5.33]$$

The final TSM product can then be calculated by the corresponding relationship between TSM and b_{bp}:

$$TSM = P_{Type} \times b_{bp} \quad [5.34]$$

Where the P_{Type} refers to water type-specific coefficients (i.e., I, II, III and IV), as listed in Table 13.

Table 13 TSM algorithms and tuned coefficients per optical water type for OLCI

OWT	Assigned Algorithm	Per-OWT Tuned Coefficients
1	Vantrepotte	A=226.0665, B=28643.9982, C=1.2399
2	Zhang	A=1514.4000, B=1.12456
3	Nechad_665nm	A=211.5660, C=0.2419

4	Nechad_709nm	A=322.2300, C=0.2454
5	Vantrepotte	A=134.7918, B=12530.6266, C=2.6909
6	Jiang2021	I=56.7642, II=68.4072, III=82.5990, IV=99.7009
7	Zhang	A=1514.4003, B=1.1454
8	Binding	b^*_{TSM} =0.8242
9	Nechad_709nm	A=322.2301, C=0.2593
10	Zhang	A=1514.4001, B=1.1450
11	Binding	b^*_{TSM} =0.8152
12	Nechad_709nm	A=322.2300, C=0.2454
13	Nechad_681nm	A=244.1341, C=0.23211

5.2.1.5.4.7 TSM algorithms for MODIS

The TSM algorithms for MODIS are assigned per OWT as detailed in Table 14. These algorithms were selected based on extensive product validation conducted for CRDP v3.0.

Table 14 Suspended matter algorithms per optical water type for MODIS

Optical water type number	Algorithm source	Algorithm optimization
1, 5, 10	Nechad et al.(2010, 2016) at 667nm	Per-OWT tuned algorithm applied to Polymer atmospherically corrected reflectance based on Lakes_cci calibration, against the LIMNADES and GLORIA datasets.
2, 7, 11	Miller and McKee (2004)	
3	Petus et al. (2010)	
4, 6, 8, 12	Klein et al. (2021)	
9	Ondrusek et al. (2012)	
3	Chen et al. (2007)	

- Nechad et al. (2010, 2016) algorithm

This algorithm is applied for the 667 nm waveband as detailed in the previous section, with per-OWT tuned coefficients for MODIS shown in Table 15.

- Miller and McKee (2004) algorithm

The Miller and McKee (2004) algorithm as it is implemented here is an empirical linear relationship between the 645nm band and in situ measured suspended matter dry weight, which is tuned to provide the best match for each of the corresponding water types:

$$TSM\ [g.m^{-3}] = A \times\ R_w(645) + B \qquad [5.35]$$

Where A and B are per-OWT tuned, and the tuned algorithm coefficients are listed in Table 15.

- Petus et al. (2010) algorithm

The Petus et al. (2010) algorithm as it is implemented here is an empirical 2nd order polynomial relation between the 645nm and TSM, which is tuned to each of the assigned OWTs:

$$TSM[g.m^{-3}] = A \times R_w(645)^2 + B \times R_w(645) + C \quad [5.36]$$

Where the per-OWT tuned parameters for A, B and C are listed in Table 15.

- Klein et al. (2021) algorithm

This algorithm is as detailed in the previous section, applied to 667 nm and 869nm wavebands, with per-OWT tuned coefficients for MODIS shown in Table 15.

- Ondrusek et al. (2012) algorithm

The Ondrusek et al. (2012) algorithm as it is implemented here is an empirical 3rd order polynomial relation between the 645nm band and in situ measured suspended matter dry weight, which is also tuned for each of the corresponding water types

$$TSM\ [g.m^{-3}] = A \times R_w(645)^3 + B \times R_w(645)^2 + C \times R_w(645) \quad [5.37]$$

Where the per-OWT tuned parameters for A, B and C are listed in Table 15.

- Chen et al. (2007) algorithm

The Chen et al. (2007) algorithm as it is implemented here is an empirical power-law relation between the 645nm band and in situ measured TSM, which is tuned for each of the assigned water types:

$$TSM\ [g.m^{-3}] = A \times R_w(645)^B \quad [5.38]$$

Where the per-OWT tuned parameters for A and B are listed in Table 15.

Table 15 TSM algorithms and tuned coefficients per optical water type for MODIS

OWT	Assigned Algorithm	Per-OWT Tuned Coefficients
1, 5, 10	Nechad_667nm	A=211.5660, C=0.2433
2	Miller	A=247.3024, B=-2.3776
3	Petus	A=-0.0377, B=162.1307, C=-510.4737
4	Klein2021	A_{red}=151.8869, C_{red}=0.1726, A_{nir}=1669.2444, C_{nir}=0.2293
6	Klein2021	A_{red}=153.8515, C_{red}=0.1726, A_{nir}=1663.9652, C_{nir}=0.2293
7	Miller	A=256.6830, B=-2.4771
8	Klein2021	A_{red}=156.2747, C_{red}=0.1726, A_{nir}=1657.4319, C_{nir}=0.2293
9	Ondrusek	A=-23.4944, B=-358.4991, C=165.6321
11	Miller	A=246.7519, B=-2.3723
12	Klein2021	A_{red}=152.2851, C_{red}=0.1726, A_{nir}=1668.1772, C_{nir}=0.2293
13	Chen	A=82.9027, B=0.8411

5.2.1.5.5 Coloured Dissolved Organic Matter algorithms

5.2.1.5.5.1 CDOM algorithms for MERIS

The CDOM algorithms for MERIS are assigned per OWT following extensive product validation for CRDP v3.0, as detailed in Table 16Table 14.

Table 16 CDOM algorithms per optical water type for MERIS

Optical water type number	Algorithm source	Algorithm optimization
1, 5, 8, 10	Ficek et al. (2011)	Per-OWT tuned algorithm applied to Polymer atmospherically corrected reflectance based on Lakes_cci calibration, against the GLORIA datasets.
2, 3, 4, 6, 9, 11, 12	Brezonik et al. (2015)	
7, 13	Tiwari & Shanmugam (2011)	

- Ficek et al. (2011)

The Ficek et al. (2011) algorithm for CDOM absorption at 440 nm ($a_{\mathrm{CDOM}}(440)$), as implemented here, expressed as an empirical relationship based on the spectral reflectance band ratio between 560 nm and 665 nm

$$a_{\mathrm{CDOM}}(440) = A \times [R_{\mathrm{w}}(560)/R_{\mathrm{w}}(665)]^{B} \quad [5.39]$$

Where A and B are per-OWT tuned parameters, as listed in Table 17.

- Brezonik et al. (2015)

The Brezonik et al. (2015) algorithm for $a_{\mathrm{CDOM}}(440)$, as implemented here, is expressed as an empirical relationship based on the spectral reflectance band ratio between 510 nm and 754 nm

$$a_{\mathrm{CDOM}}(440) = \exp[A \times \ln\left(\frac{R_{\mathrm{w}}(510)}{R_{\mathrm{w}}(754)}\right) + B] \quad [5.40]$$

Where A and B are per-OWT tuned parameters, as listed in Table 17.

- Tiwari & Shanmugam, (2011)

The Tiwari & Shanmugam (2011) algorithm for $a_{\mathrm{CDOM}}(440)$, as implemented here, is expressed as an empirical linear relationship based on the spectral reflectance band ratio between 665 nm and 490 nm

$$a_{\mathrm{CDOM}}(440) = A \times \left(\frac{R_{\mathrm{w}}(665)}{R_{\mathrm{w}}(490)}\right) + B \quad [5.41]$$

Where A and B are per-OWT tuned parameters, as listed in Table 17.

Table 17 CDOM algorithms and tuned coefficients per optical water type for MERIS

OWT	Assigned Algorithm	Per-OWT Tuned Coefficients
1,5,8,10	Ficek2011	A=2.92, B=-2.3160
2	Brezonik2015	A=-0.626, B=0.1954
3	Brezonik2015	A=-0.7130, B=0.2573
4	Brezonik2015	A=-0.6572, B=-0.2336

6	Brezonik2015	A=-0.6565, B=-0.2342
7	TiwariShanmugam2011	A=0.7696, B=0.001548
9	Brezonik2015	A=-0.7174, B=0.4504
11	Brezonik2015	A=-0.6431, B=-0.2532
12	Brezonik2015	A=-0.6638, B=-0.2231
13	TiwariShanmugam2011	A=0.7726, B=0.001445

5.2.1.5.5.2 CDOM algorithms for OLCI

The CDOM algorithms for OLCI are assigned per OWT, following extensive product validation for CRDP v3.0, as detailed in Table 18Table 14.

Table 18 CDOM algorithms per optical water type for OLCI

Optical water type number	Algorithm source	Algorithm optimization
1, 6, 7, 8, 11	Mannino et al. (2014)	Per-OWT tuned algorithm applied to Polymer atmospherically corrected reflectance based on Lakes_cci calibration, against the GLORIA datasets.
2, 4, 5, 12, 13	Brezonik et al. (2015)	
3	Tiwari & Shanmugam (2011)	
9	Shanmugam (2011)	
10	Wang et al. (2017)	

- Mannino et al. (2014)

Mannino et al. (2014) for $a_{CDOM}(440)$, as is implemented here, is a multiple linear regression algorithm based on bands 443nm and 560 nm:

$$R_{rs}(\lambda) = R_w(\lambda)/\pi \quad [5.42]$$

$$a_{\mathrm{CDOM}}(440) = \exp[A \cdot \ln(R_{\mathrm{rs}}(443)) + \mathrm{B} \cdot \ln(R_{\mathrm{rs}}(560)) + C] \quad [5.43]$$

Where A and B are per-OWT tuned parameters, as listed in Table 19.

- Brezonik et al. (2015)

This algorithm is as detailed in the previous section, with per-OWT tuned coefficients for OLCI shown in Table 19.

- Shanmugam (2011)

Shanmugam (2011) for $a_{CDOM}(440)$, as is implemented here, is a simplified version of the approach detailed in their original publication, formulated as:

$$a_{\mathrm{CDOM}}(440) = A \times \left(\frac{R_{\mathrm{w}}(443)}{R_{\mathrm{w}}(560)}\right)^{B} \quad [5.44]$$

Where A and B are per-OWT tuned parameters, as listed in Table 19.

- Wang et al. (2017)

The fully normalized water-leaving reflectance ($R_w(\lambda)$, λ=443, 490 or 681 nm) is firstly converted to below-surface remote-sensing reflectance (*rrs*(λ)) as follows:

$$r_{\mathrm{rs}}(\lambda) = \frac{R_{\mathrm{rs}}(\lambda)}{\alpha(\lambda)+\beta(\lambda)R_{\mathrm{rs}}(\lambda)} \quad [5.45]$$

Where $R_{rs}(\lambda) = R_w(\lambda)/\pi$, and $\alpha(\lambda)$ and $\beta(\lambda)$ are calculated as follows:

$$\alpha(\lambda) = 0.3638 + 8.776 \times 10^{-4}\lambda - 9.193 \times 10^{-7}\lambda^2 + 3.17 \times 10^{-10}\lambda^3 \quad [5.46]$$

$$\beta(\lambda) = 1.357 + 8.608 \times 10^{-4}\lambda - 6.347 \times 10^{-7}\lambda^2 \quad [5.47]$$

The ratio of backscattering to the sum of backscattering and absorption, μ(λ), can be obtained from below-surface remote-sensing reflectance *rrs*(λ) according to the work by Gordon et al. (1988) as:

$$u(\lambda) = \frac{-g_0+\sqrt{{g_0}^2+4\times g_1 \times rrs(\lambda)}}{2\times g_1} \quad [5.48]$$

Where g_0 = 0.089 and g_1 = 0.1245.

The total absorption at reference band 681 nm (λ_0) can be then calculated as:

$$a(\lambda_0) = a(681) = a_{\mathrm{w}}(681) + 0.9398x^2 + 0.865x - 0.0852 \quad [5.49]$$

$$x = \frac{R_{\mathrm{rs}}(681)}{R_{\mathrm{rs}}(490)} \quad [5.50]$$

$$b_{bp}(\lambda_0) = b_{bp}(681) = \frac{u(681)\times a(681)}{1-u(681)} - b_{bw}(681) \quad [5.51]$$

$$Y = 1.75 b_{bp}(681)^{-0.05} \quad [5.52]$$

Where $a_w(681)$=0.472 m^{-1}, $b_{bw}(681)$=0.000336 m^{-1}.

$$b_{\mathrm{bp}}(\lambda) = b_{\mathrm{bp}}(\lambda_0)\left(\frac{\lambda_0}{\lambda}\right)^Y \quad [5.53]$$

$$a(443) = \frac{(1-u(443))(b_{\mathrm{bw}}(443)+b_{\mathrm{bp}}(443))}{u(443)} \quad [5.54]$$

$a_p(443)$ is estimated as follows:

$$a_p(443) = 4.8024 b_{bp}(681)^{0.8055} \quad [5.55]$$

$$a_{\mathrm{CDOM}}(443) = a(443) - a_{\mathrm{w}}(443) - a_{\mathrm{p}}(443) \quad [5.56]$$

The $a_{\mathrm{CDOM}}(440)$ can be then obtained from an emperical power-law relationship with $a_{\mathrm{CDOM}}(443)$

$$a_{\mathrm{CDOM}}(440) = A \times a_{\mathrm{CDOM}}(443)^B + C \quad [5.57]$$

Where A and B are per-OWT tuned parameters, as listed in Table 19.

Table 19 CDOM algorithms and tuned coefficients per optical water type for OLCI

OWT	Assigned Algorithm	Per-OWT Tuned Coefficients
1	Mannino2014	A= -1.4056, B=0.7545, C=-4.2238
2	Brezonik2015	A=-0.8609, B=0.6715

3	TiwariShanmugam2011	A=0.8179, B=0.001613
4	Brezonik2015	A=-0.7953, B=0.6219
5	Brezonik2015	A=-0.7480, B=0.5451
6	Mannino2014	A=-1.4391, B=0.7661, C=-4.2238
7	Mannino2014	A=-1.4388, B=0.7825, C=-4.2237
8	Mannino2014	A=-1.4391, B=0.7699 , C=-4.2237
9	Shanmugam2011	A=5.3625, B=3.2091
10	Wang2017	A=0.3400, B=0.5780, C=0.12131
11	Mannino2014	A=-1.4391, B=0.7669, C=-4.2237
12	Brezonik2015	A=-0.8145, B=0.6407
13	Brezonik2015	A=-0.7454, B=0.2796

5.2.1.5.5.3 CDOM algorithms for MODIS

The CDOM algorithms for MODIS are assigned per OWT following on extensive product validation conducted during Phase 2 of the Lakes_cci project, as detailed in Table 20Table 14.

Table 20 CDOM algorithms per optical water type for MODIS

Optical water type number	Algorithm source	Algorithm optimization
1, 2, 3, 4, 5, 6, 7, 8, 10, 11, 12, 13	Brezonik et al. (2015)	Per-OWT tuned algorithm applied to Polymer atmospherically corrected reflectance based on Lakes_cci calibration, against the GLORIA datasets.
9	Ficek et al. (2011)	

- Brezonik et al. (2015) follows the methodology detailed in the previous section, with application bands shifted to 531 nm and 748 nm for MODIS. The per-OWT tuned coefficients are presented in Table 21.
- Ficek et al. (2011) follows the methodology detailed in the previous section, with application bands shifted to 555 nm and 667 nm for MODIS. The per-OWT tuned coefficients are presented in Table 21.

Table 21 CDOM algorithms and tuned cefficients per optical water type for MODIS

OWT	Assigned Algorithm	Per-OWT Tuned Coefficients
1	Brezonik2015	A=-1.2929, B=1.8491
2	Brezonik2015	A=-1.2929, B=1.8928
3	Brezonik2015	A=-1.3957, B=1.9393
4	Brezonik2015	A=-1.3595, B=2.0271

5	Brezonik2015	A=-1.1376, B=1.4229
6	Brezonik2015	A=-1.2853, B=1.8863
7	Brezonik2015	A=-1.3015, B=1.9002
8	Brezonik2015	A=-1.3660, B=2.0336
9	Ficek2011	A=3.2850, B=-1.7370
10	Brezonik2015	A=-1.2264, B=1.8015
11	Brezonik2015	A=-1.3573, B=2.0310
12	Brezonik2015	A=-1.3645, B=2.0311
13	Brezonik2015	A=-1.1376, B=1.3215

5.2.1.5.6 Vertical diffuse attenuation coefficient (K_d) algorithms

The diffuse downwelling attenuation coefficient of (K_d) describes water transparency and light availability in the water column. K_d can be semi-analytically retrieved from R_{rs} through two steps: (I) estimate absorption and backscattering coefficients (a, b_b) from R_{rs}; (II) estimate K_d from absorption and back scattering coefficients and solar zenith angle.

Step I: to estimate a and b_b from R_{rs}, the quasi-analytical algorithm (QAA) is used, which generally includes the following steps:

$$r_{rs}(\lambda) = \frac{R_{rs}(\lambda)}{0.52+1.7\times R_{rs}(\lambda)} \quad [5.58]$$

$$u(\lambda) = \frac{-g_0+\sqrt{g_0{}^2+4\times g_1\times r_{rs}(\lambda)}}{2\times g_1} \quad [5.59]$$

Where r_{rs} is the remote sensing reflectance just below water surface, g_0=0.089, g_1=0.125, λ is the wavelength of satellite bands.

$$a(\lambda_0) = a_w(\lambda_0) + \Delta a(\lambda_0) \quad [5.60]$$

Where λ_0 is the reference wavelength, $a_w(\lambda_0)$ is the absorption coefficient of pure water at the reference wavelength, $\Delta a(\lambda_0)$ is the contribution of absorption by non-water constitutes (i.e., Chl-*a*, TSM, CDOM) at the reference wavelength.

$$b_{bp}(\lambda_0) = \frac{u(\lambda_0)\times a(\lambda_0)}{1-u(\lambda_0)} - b_{bw}(\lambda_0) \quad [5.61]$$

Where $b_{bp}(\lambda_0)$ is the backscattering coefficient at the reference wavelength, $b_{bw}(\lambda_0)$ is the backscattering coefficient of pure water at the reference wavelength.

$$b_b(\lambda) = b_{bp}(\lambda_0)(\frac{\lambda_0}{\lambda})^{\eta} + b_{bw}(\lambda) \quad [5.62]$$

Where η is the spectral slope of b_{bp}, b_{bw} is the back scattering coefficient of pure water.

$$a(\lambda) = \frac{(1-\mu(\lambda))b_b(\lambda)}{\mu(\lambda)} \quad [5.63]$$

Step II: to estimate K_d from a and b_b, the semi-analytical algorithm from Lee et al. (2013) is used:

$$K_d(\lambda) = (1 + 0.005\theta)a(\lambda) + 4.259\left(1 - 0.265h_w(\lambda)\right)\left(1 - 0.52e^{-10.8a(\lambda)}\right)b_b(\lambda) \quad [5.64]$$

where θ is the solar zenith angle, $h_w(\lambda)$ is the ratio of $b_{bw}(\lambda)$ and $b_b(\lambda)$. It should be noted that K_d is an apparent optical property (AOP), so its value depends on the light field. In Lakes_cci, we set the solar zenith angle to 0 degree for all lakes, i.e., light comes from nadir direction, to make the produced K_d data comparable between different lakes and at different time.

Finally, K_d for photosynthetically active radiation (K_d(PAR)) is calculated by assessing the photon count (rather than energy) loss over depth in each waveband considered, converting energy to photon flux using Planck's constant. The loss of photons over an (arbitrary) 3-m depth interval is calculated in each waveband, then the number of photons across the red, green and blue bands is used for the spectral average to represent PAR.

5.2.1.5.7 K_d algorithms for MERIS and OLCI

Optimisation per OWT focusses on the parameterisatio of QAA for estimating *a* and b_b from R_{rs} (Step I above). The step for estimating K_d from *a* and b_b (Step II) is identical between OWTs. The QAAs for MERIS and OLCI assigned per OWT are shown in Table 22.

Table 22. QAA algorithm per optical water type for MERIS and OLCI.

OWT	K_d(490)	K_d(560)	K_d(665)
1	Pedroso Curtarelli et al (2020)	Le et al (2009)	Pitarch et al (2021)
2	Gons et al (2005)	Le et al (2009)	Le et al (2009)
3	Rodrigues et al (2017)	Rodrigues et al (2017)	QAA v6
4	Liu et al (2019)	Gons et al (2005)	Pitarch et al (2021)
5	Gons et al (2005)	Yang et al (2013)	Pitarch et al (2021)
6	Gons et al (2005)	Le et al (2009)	Pitarch et al (2021)
7	Pedroso Curtarelli et al (2020)	Yang et al (2013)	Pitarch et al (2021)
8	Gons et al (2005)	Yang et al (2013)	Pitarch et al (2021)
9	Pitarch et al (2021)	QAA v5	Joshi et al (2018)
10	Yang et al (2013)	Yang et al (2013)	Pitarch et al (2021)
11	Gons et al (2005)	Gons et al (2005)	Joshi et al (2018)
12	Gons et al (2005)	Gons et al (2005)	Pitarch et al (2021)
13	Rodrigues et al (2017)	Rodrigues et al (2017)	QAA v6

Different QAAs generally follow the same calculation steps as shown in Step I, and the main differences are the choice of reference wavelength λ_0, and the equations for estimating $a(\lambda_0)$ and η. The overview below only presents equations that differ from the general Step I abaove:

- **QAA_v5 (Lee et al., 2009) (hereafter, v5)**

v5 uses 560 nm as the reference wavelength:

$$a(\lambda_0) = 0.0621 + 10^{-1.146 - 1.366\chi - 0.469\chi^2} \quad [5.65]$$

$$\chi = \log_{10}\left(\frac{r_{rs}(443)+r_{rs}(490)}{r_{rs}(560)+5\frac{r_{rs}(665)}{r_{rs}(490)}r_{rs}(665))}\right) \quad [5.66]$$

$$\eta = 2.0\left(1 - 1.2 \times \exp\left(-0.9\frac{r_{rs}(443)}{r_{rs}(560)}\right)\right) \quad [5.67]$$

- **QAA_v6 (IOCCG, 2014) (hereafter, v6)**

V6 uses 665 nm as reference wavelength:

$$a(\lambda_0) = 0.4275 + 0.39\left(\frac{R_{rs}(665)}{R_{rs}(443)+R_{rs}(490)}\right)^{1.14} \quad [5.68]$$

η is calculated using the same equation as in v5.

- **Pedroso Curtarelli et al. (2020) (hereafter, C20)**

C20 uses 560 nm as reference wavelength:

$$a(\lambda_0) = 0.0621 + 0.43\left(\frac{R_{rs}(560)}{R_{rs}(665)+R_{rs}(709)}\right)^{-1.44} \quad [5.69]$$

$$\eta = 0.5248 \times exp\left(\frac{r_{rs}(665)}{r_{rs}(709)}\right) \quad [5.70]$$

- **Gons et al. (2005) (hereafter, G05)**

G05 use 779 nm as reference wavelength, and $b_{bp}(\lambda_0)$ is calculated uses the equations below:

$$R_w(779) = R_{rs}(779) \times pi \quad [5.71]$$

$$b_{bp}(\lambda_0) = \frac{0.6\times a_w(779)\times R_w(779)}{0.082-0.6\times R_w(779)} - b_{bw}(779) \quad [5.72]$$

Where $a_w(779) = 2.6994$, η is calculated using the same equation as in QAA_v5.

- **Rodrigues et al. (2017) (hereafter, R17)**

R17 use 560 nm as reference wavelength:

$$a(\lambda_0) = 0.0621 + 10^{-1.146-1.366\chi-0.469\chi^2} \quad [5.73]$$

$$\chi = \log_{10}\left(\frac{0.02\times r_{rs}(443)+r_{rs}(490)}{r_{rs}(560)+0.005\frac{r_{rs}(665)}{r_{rs}(490)}r_{rs}(665))}\right) \quad [5.74]$$

$$\eta = 2.2\left(1 - 1.2 \times \exp\left(-0.9\frac{r_{rs}(443)}{r_{rs}(560)}\right)\right) \quad [5.75]$$

- **Liu et al. (2019) (hereafter, L19)**

L19 uses 560 nm as reference wavelength:

$$a(\lambda_0) = 0.0621 + 0.739\left(\frac{R_{rs}(560)}{R_{rs}(665)+R_{rs}(779)}\right)^{-2.36} \quad [5.76]$$

$$\eta = 4.52 \times exp\left(\frac{r_{rs}(443)}{r_{rs}(490)}\right) - 7.0 \quad [5.77]$$

- **Pitarch et al. (2021) (hereafter, P21)**

P21 uses 560 nm as reference wavelength:

$$a(\lambda_0) = 0.0621 + 10^{P_0 + P_1\chi + P_2\chi^2 + P_3\chi^3} \quad [5.78]$$

Where P_0=-1.09651, P_1=-1.33678, P_2=-0.35707, P_3=-0.08409

$$\chi = \log_{10}\left(\frac{2.0 \times R_{rs}(490)}{R_{rs}(560) + 5\frac{R_{rs}(665)}{R_{rs}(490)}R_{rs}(665))}\right) \quad [5.79]$$

$$\eta = 2.0 \times \left(1 - 1.2 \times \exp(-0.9 \times QBG)\right) \quad [5.80]$$

$$QBG = q_0 + q_1 \times bg + q_2 \times bg^2 + q_3 \times bg^3 \quad [5.81]$$

$$bg = \frac{R_{rs}(443)}{R_{rs}(560)} \quad [5.82]$$

Where q_0=-0.02085, q_1=0.540187, q_2=0.226931, q_3=0.010022

- **Yang et al. (2013) (hereafter, Y13)**

Y13 uses 754 nm as reference wavelength:

$$a(\lambda_0) = a_w(\lambda_0) = 2.8683 \quad [5.83]$$

$$\eta = -372.99x^2 + 37.286x + 0.84 \quad [5.84]$$

$$x = \log_{10}\left(\frac{u(754)}{u(779)}\right) \quad [5.85]$$

- **Le et al. (2009) (hereafter, L09)**

L09 uses 709 nm as reference wavelength:

$$a(\lambda_0) = a_w(\lambda_0) = 0.8156 \quad [5.86]$$

$$\eta = 2.2\left(1 - 1.2 \times \exp\left(-0.9\frac{r_{rs}(560)}{r_{rs}(754)}\right)\right) \quad [5.87]$$

- **Joshi et al. (2018) (hereafter, J18)**

J18 uses 560 nm as reference wavelength, and different g_0 and g_1 are used for calculating $u(\lambda)$ from $r_{rs}(\lambda)$:

$$\rho = \log_{10}\left(\frac{r_{rs}(560)}{r_{rs}(665)}\right) \quad [5.88]$$

If $\rho < 0.25$, $g_0 = 0.0788, g_1 = 0.2379$, and $a(\lambda_0)$ is estimated using:

$$a(\lambda_0) = 0.0621 + 10^{0.081 - 1.868\rho + 0.688\rho^2} \quad [5.89]$$

If $\rho \geq 0.25$, $g_0 = 0.0895, g_1 = 0.1247$, and $a(\lambda_0)$ is estimated using:

$$a(\lambda_0) = 0.0621 + 10^{0.314 - 2.733\rho + 0.713\rho^2} \quad [5.90]$$

5.2.1.5.7.1 K_d algorithms for MODIS

The QAAs for MODIS assigned per OWT are shown in Table 23.

Table 23. QAA algorithms per optical water type for MODIS.

OWT	$K_d(488)$	$K_d(555)$	$K_d(667)$
1	Joshi et al (2018)	Joshi et al (2018)	Pitarch et al (2021)
2	Joshi et al (2018)	Joshi et al (2018)	Pitarch et al (2021)
3	Rodrigues et al (2017)	Rodrigues et al (2017)	QAA v6
4	Joshi et al (2018)	Joshi et al (2018)	Pitarch et al (2021)
5	Joshi et al (2018)	Joshi et al (2018)	Pitarch et al (2021)
6	Joshi et al (2018)	Joshi et al (2018)	Pitarch et al (2021)
7	Joshi et al (2018)	Joshi et al (2018)	Pitarch et al (2021)
8	Joshi et al (2018)	Joshi et al (2018)	Pitarch et al (2021)
9	Joshi et al (2018)	Wang et al (2017)	Wang et al (2017)
10	Joshi et al (2018)	Joshi et al (2018)	Pitarch et al (2021)
11	Joshi et al (2018)	Joshi et al (2018)	Pitarch et al (2021)
12	Pitarch et al (2021)	Pitarch et al (2021)	Pitarch et al (2021)
13	Rodrigues et al (2017)	Rodrigues et al (2017)	QAA v6

The equations of QAA for MODIS are same as those for MERIS and OLCI except for the following differences:

- $a_w(\lambda_0)$ and $b_{bw}(\lambda_0)$ for MODIS are different with MERIS and OLCI;
- Because the bands are different between MODIS and MERIS (OLCI), the nearest bands were used in QAA equations for MODIS, i.e., replacing $R_{rs}(490)$ by $R_{rs}(488)$, replacing $R_{rs}(560)$ by $R_{rs}(555)$, replacing $R_{rs}(665)$ by $R_{rs}(667)$.

In addition, the QAA from Wang et al. (2017) (hereafter, W17) was selected for K_d estimation for MODIS, which includes different equations for calculating r_{rs} from R_{rs}:

$$\alpha = 0.3638 + 8.776 \times 10^{-4} \times \lambda - 9.193 \times 10^{-7} \times \lambda^2 + 3.174 \times 10^{-10} \times \lambda^3 \quad [5.91]$$

$$\beta = 1.357 + 8.608 \times 10^{-4} \times \lambda - 6.347 \times 10^{-7} \times \lambda^2 \quad [5.92]$$

$$r_{rs}(\lambda) = \frac{R_{rs}(\lambda)}{\alpha + \beta \times R_{rs}(\lambda)} \quad [5.93]$$

W17 uses 678 nm as reference wavelength:

$$a(\lambda_0) = 0.4564 + 0.9398x^2 + 0.865x - 0.0852 \quad [5.94]$$

$$x = \frac{R_{rs}(678)}{R_{rs}(488)} \quad [5.95]$$

$$\eta = 1.75 \times b_{bp}(\lambda_0)^{-0.05} \quad [5.96]$$

5.2.1.5.8 Phycocyanin algorithms

The phycocyanin product is introduced in v3.0.0 to assist with the intial detection of shift in phytoplankton composition in lakes, where phycocyanin typically marks the presence of cyanobacteria.

Unlike the other LWLR-derived products, phycocyanin is derived using a single Mixed Density Network algorithm strategy, trained on the GLORIA dataset. The fundamental properties of the algorithm are the same as described above for Chla estimates from MERIS and OLCI. The MDN-PC algorithm was previously published for OLCI and other sensors (Pahlevan et al. 2022, Zolfaghari et al. 2022) and recently updated for use with MERIS. Product uncertainty is currently not available for this product.

5.2.2 Methods to generate quality flags

Quality information is added to the quality_flags variable from three sources:

- L1 satellite input product per-pixel flags indicating suboptimal or poor observations
- L2 processing algorithms, including atmospheric correction and derived variables
- L3 processing, i.e. inconsistencies observed from comparing many L2 products

The lwlr_quality_flag variable provides essential information to users regarding the reasons behind missing observations and aids in the proper use of the data. The following flags indicate that at least one of the source products for the aggregation period was affected by a condition that prevented processing to L2:

- lwlr_cloud: not processed due to suspected cloud
- lwlr_land: not processed due to suspected land
- lwlr_snow_ice: not processed due to suspected snow or ice
- lwlr_bright_pixels: masked due to extreme reflectance values
- lwlr_atmospheric_correction_failure: no atmospheric correction result

The following flags indicate that at least one of the source products in the aggregation period was affected by a condition that may affect observation quality, even though the output was not masked:

- lwlr_land_contaminated: risk of land influence on water signal
- lwlr_high_solar_zenith_angle: low observation quality due to high solar zenith angle (>76 degrees)
- lwlr_poor_consistency: illegal combination of LWLR, LWST, and/or LIC
- lwlr_low_consistency: pixel includes at least some suspect combinations of LWLR, LWST, and/or LIC
- lwlr_floating_cyanobacteria: likely presence of cyanobacteria floating at the water surface
- lwlr_floating_macrophytes_or_mixed_pixel: likely presence of macrophytes floating at the water surface, or combined water-land-vegetation within pixel.

The three categories of product flagging are detailed in the following subsections.

5.2.2.1 Quality flags from L1 products

Pixels classified as ‘Invalid’ in the L1 product, or with an a sun zenith angle exceeding 76 degrees are masked out from Rw and derived variables. Any L1 products that flag the saturation of any

waveband are also observed and corresponding pixels masked out – noting that the LWLR product itself is also checked for the presence of unrealistically bright water surfaces.

5.2.2.2 Quality flags from L2 product generation

Per-pixel classification using Idepix provides land, cloud (including buffer and shadow) and suspected ice or snow masks. These are excluded from LWLR processing meaning no LWLR (Rw) or derived variables are available, and reported in the cloud, land, and snow_ice quality flags. Pixels outside the region-of-interest definition of the water body are also masked.

Atmospheric correction failures are masked out on the basis of the Polymer 'out of bounds' flag (reported in the 'atmospheric_correction_failure flag). The resulting R_w variables at 412, 560 and 865 nm are inspected and pixels where either exceeds 0.4 are masked across the R_w and derived products (reported in the 'bright_pixels' quality flag).

During the Optical Water Type classification stage, similarity to a 'land adjacency' spectrum is quantified. When similarity to this spectrum exceeds 0.9, R_w and derived products are masked and the occurrence is reported in the 'land_contaminated' quality flag.

Finally, the floating_cyanobacteria and floating_macrophytes_or_mixed_pixel quality flags are determined by adapting the Maximum Peak Height (MPH) algorithm from Matthews and Odermatt (2015), to detect floating cyanobacteria and floating vegetation. Whereas the original algorithm is based on BRR to partially remove atmospheric effects, the method used here was calibrated and applied to TOA reflectance, to reduce computation time. The MPH algorithm works on the principle that the concentration of phytoplankton can be estimated from the MPH of the reflectance spectrum in the red to near-infrared region of the electromagnetic spectrum, where the location of the peak is variable. A Sun-Induced Chlorophyll Fluorescence (SICF) peak feature typically appears in low-biomass conditions, centred on the Chl-a fluorescence emission which is observable in 681nm satellite bands and typically more expressed in algal species and vegetation than in cyanobacteria. The Sun-Induced Phycocyanin absorption and Fluorescence (SIPF) feature centres on the spectral band where phycocyanin absorption and fluorescence may appear, which is a characteristic feature of cyanobacteria blooms in nutrient-replete bloom conditions. Comparing these two variables allows cyano-dominant waters to be distinguished from other phytoplankton blooms: cyanobacteria-specific spectral pigmentation features will enhance SIPF and reduce SICF. This work demonstrates how the adapted MPH signatures provide consistent estimates for cyanobacteria surface blooms and floating macrophytes.

The workflow for detection of surface blooms with Sentinel-3 OLCI wavebands is shown in Figure 7. First, the normalised difference vegetation index (NDVI) is used to distinguish between a surfacing bloom versus mixed conditions. If a surface bloom is detected, SIPF and SICF are used to distinguish between floating cyanobacteria and floating macrophytes based on defined thresholds.

The following equations for the NDVI, SICF and SIPF are used:

$$NDVI = \frac{B18-B8}{B18+B8} \quad [5.97]$$

$$SICF = B10 - B8 - ((B11 - B8) * \frac{681-664}{709-664} \quad [5.98]$$

$$SIPF = B8 - B7 - ((B10 - B7) * \frac{664-619}{681-619} \quad [5.99]$$

Exponential functions are used to calculate probabilities of floating cyanobacteria and floating macrophytes using the rate of change of SICF and SIPF with the following equation:

$$-e^{\alpha*SICF-\beta*SIPF} + 1 \quad [5.100]$$

The resulting probability indicates the likelihood of floating cyanobacteria or floating macrophytes presence in each pixel. The weights in the probability function are α = 60 and β = 60.

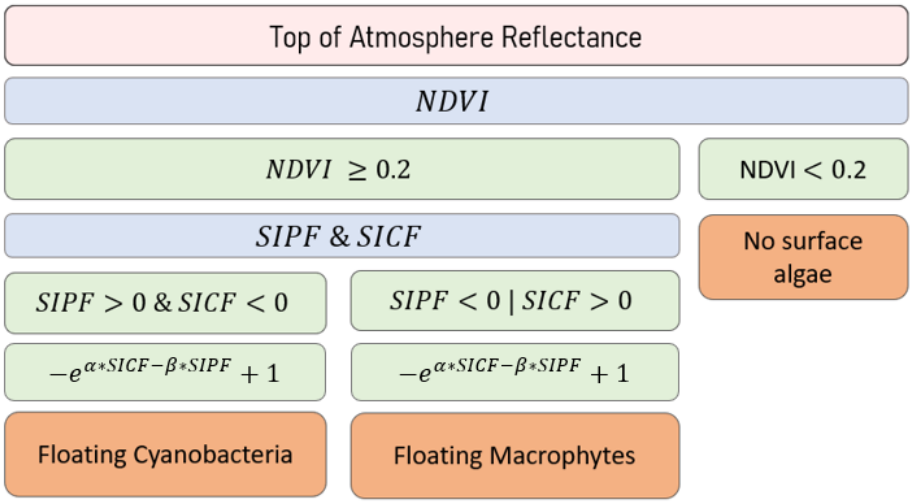

Figure 7. Workflow of detecting surface blooms with Sentinel-3 OLCI

The thresholds used here were identified against visual inspection of processed imagery. Reference data for the actual occurrence of surface blooms and floating aquatic vegetation are generally lacking. Moreover, due to their patchy distribution in time and space, spatial variability of the blooms is not easily captured from in situ observations. The Sentinel 3 OLCI methodology was calibrated against the MPH based on BRR, and was found to yield the same floating biomass indicator values from TOA signals, in imagery where both floating cyanobacteria and floating macrophytes were visually observed.

The floating cyanobacteria and macrophytes flag is not raised if the atmospherically corrected R_w is in the range 0.4 – 2 at either 412 or 865 nm, to avoid misclassification of land pixels.

Please note that the floating cyanobacteria and macrophyte flag is not generated when the satellite product is from MODIS, due to lack of essential wavebands.

5.2.2.3 Quality flags during L3 product generation

A climatology based consistency analysis is implemented by comparing LWLR L2 products against LSWT climatology, to determine whether outliers are likely to be caused by thin or sub-pixel ice.

The filtering procedure consists of two steps, the first clustering the per-lake water quality products derived from LWLR against LWST to identify specific outliers patterns, the second to assign per-pixel quality flags based on the data distributions derived from the former step.

In the clustering step, extractions of the lake-median value for Chla, TSM, and LSWT are generated for each lake, for each sensor period. The LWST is a climatology calculated from daily data, spanning the 2002 - 2020 period. To determine the consistency between the water quality product and LSWT for each lake, a BIRCH clustering technique (implemented as sklearn. cluster. Birch in Python) is applied to each combination of WQ (either Chla or Turbidity) and LSWT. This process classifies the per-lake time-series into several clusters, with each cluster corresponding to different degrees of consistency between the WQ variable and LSWT. Clusters with the highest median values, lowest associated temperature, and rare occurrence are scored accordingly (Figure 8) to determine whether they are likely good, low or poor quality observations.

In the second step, data distributions of WQ and LSWT for each cluster are used to assign per-pixel good, poor and low consistency flags to the L3 products. Any observations where the LSWT climatology is > 278K remains categorized as good. For the remaining observations, a decision tree (Figure 9) is used.

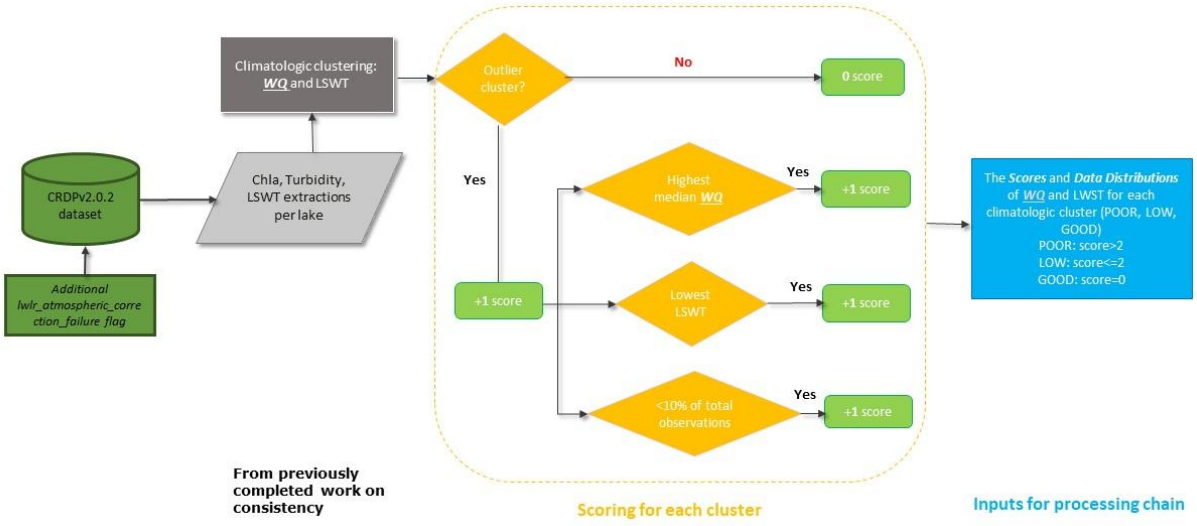

Figure 8 Climatologic cluster generation and the scoring system.

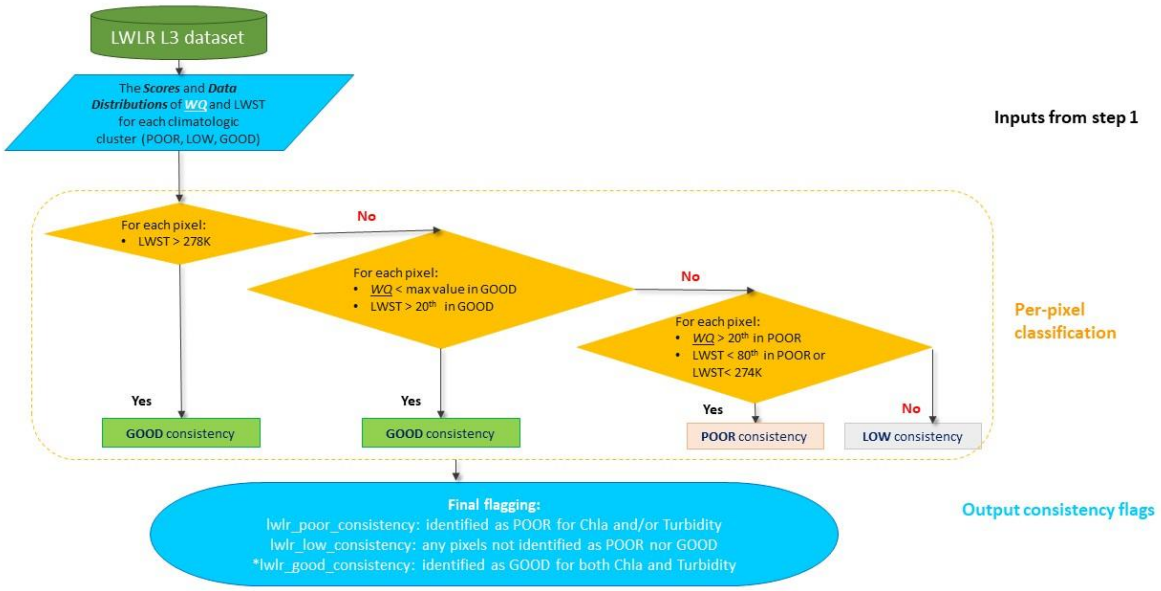

Figure 9 Climatologic consistency flag generation.

5.3 Input products and dependencies

Satellite input data:

- Envisat MERIS L1B, 4th reprocessing, Full and Reduced Resolution (SAFE format)
- Sentinel 3A/B OLCI L1B (SAFE format)
- MODIS Aqua L1A (+ GEO files)

Lake water boundaries:

- maximum water extent observed in ESA CCI Land Cover (v4.0) at 150-m resolution
- polygons generated (including manual inspection) at PML (doi: 10.5281/zenodo.3349547).

POLYMER ancillary data:

- ECMWF Meteorological Analysis data bundled with OLCI NTC (source ESA/EUM)
- Global Modeling and Assimilation Office (NASA GMAO) atmospheric optical data (Forward Processing)

Optical water type definitions (mean spectra standardized using Simpson's criterion)

- GloboLakes project (Spyrakos et al. 2018)
- Adjacent-land affected water types (Jiang et al. 2023)

In situ algorithm calibration reference datasets:

- GLORIA (Lehmann et al. 2021)
- LIMNADES (no longer accessible)

Please refer to section 5.7 for details on the accessed in situ datasets.

5.4 Output product

The output data (product layers) are produced as gridded variables in a NetCDF file. At processing Level 2 (L2) these follow the native projection of the respective sensor. In the merged L3S product these have been aggregated to a planetary geographic grid at 1/120 degrees (approximately 1 km resolution) using the nearest-neighbour approach. Each datum is derived from only one sensor, even during periods where MODIS and either MERIS or OLCI overlap. In those cases, MERIS or OLCI observations are used for the respective mission span, meaning that MODIS data are not used to fill spatiotemporal gaps. Where multiple overpasses from the same sensor (or from OLCI A and B) are available on a given day (particularly common at higher latitudes), observations nearest solar noon are preferentially used.

Variables include each reflectance band except those used exclusively for atmospheric correction, the derived chlorophyll-a and suspended matter, and the associated per-pixel uncertainty for each of these. Reflectance wavebands from different sensors, where the centre wavelengths are within 6 nm are reported as the OLCI-equivalent band to facilitate time-series analysis. Intermediary (i.e. L2) products are not distributed to users but are generally stored for product validation and improvement purposes and may be requested from PML for specific studies. These include the specific outputs from individual algorithms (prior to mapping/blending) and all processor-generated flags. A detailed overview of the output bands, their data types and attributes are provided in the Product Specification Document (PSD).

Specific quality flags are added to the final products as described in the previous section, with more detail given in the Product Specification Document (PSD).

5.5 Quality Assessment

This section provides a high-level quality assessment of the LWLR and derived products is based on comparison against in situ observations, illustrating any artefacts that users should be aware of. This section contains an overview of product quality assessment efforts resulting from past and present validation activities, to provide the user sufficient information to determine which variables are suitable for their particular use case. Further details are provided in the PVASR and E3UB documents, focussed on algorithm comparison and uncertainty characterisation, respectively.

5.5.1 Atmospheric correction

Examples of scenes for clear, turbid and productive lakes are given below, resulting from POLYMER v4.15 configured with a wide range of per-pixel initialisation conditions and using all wavebands in the 443-865 nm range.

5.5.1.1 MERIS examples

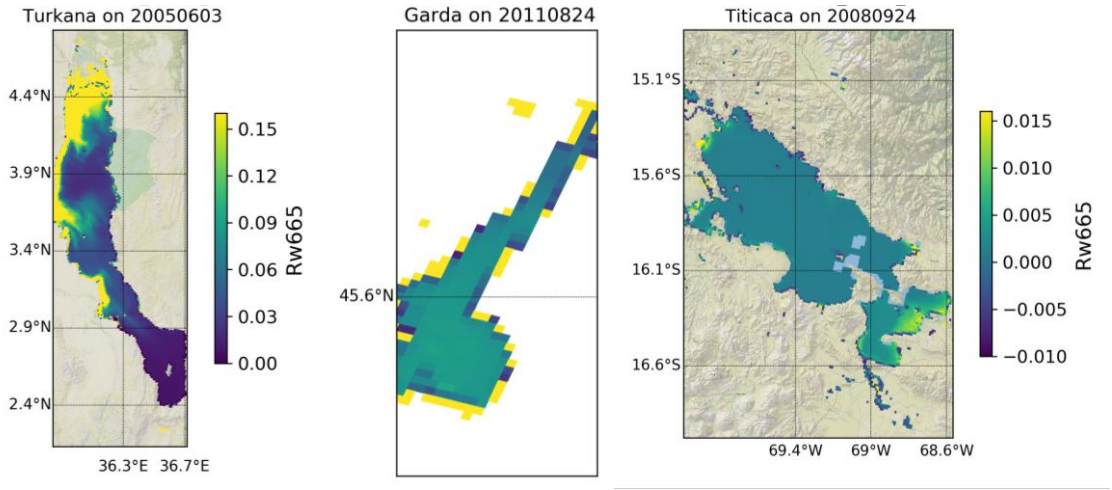

Figure 10: Band R_w(665) LWLR in Lakes Turkana (turbid), Garda (clear) and Titicaca (clear) using MERIS.

Shoreline effects are clearly observed in the MERIS imagery of Lake Garda and some areas of Lake Titicaca, potentially in shallow or vegetated areas (Figure 10). These outliers typically show R_w in the 0.1-0.5 range, well separated from values seen in open water, and are subject to quality flagging. Quality flags are not typically part of data masking procedures, so users are advised to consider which quality flags to use to mask suboptimal data points depending on their specific application. The wide variation in turbidity in Lake Turkana is well resolved. Note that, due to the mixed used of Full and Reduced Resolution MERIS observations, shoreline and adjacent land effects may be more visible during specific time periods where full resolution data were not available.

5.5.1.2 MODIS examples

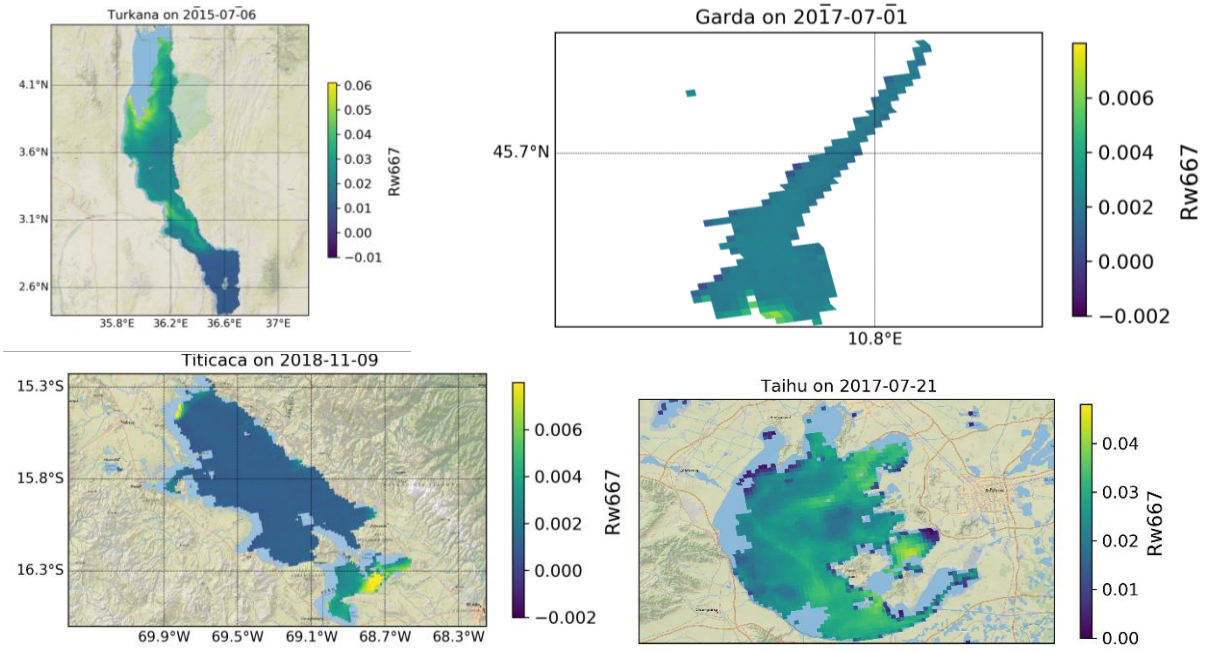

Figure 11: Band R_w(667) LWLR in Lakes Turkana (turbid), Garda (clear), Titicaca (clear) and Taihu (productive) using MODIS-Aqua.

5.5.1.3 OLCI examples

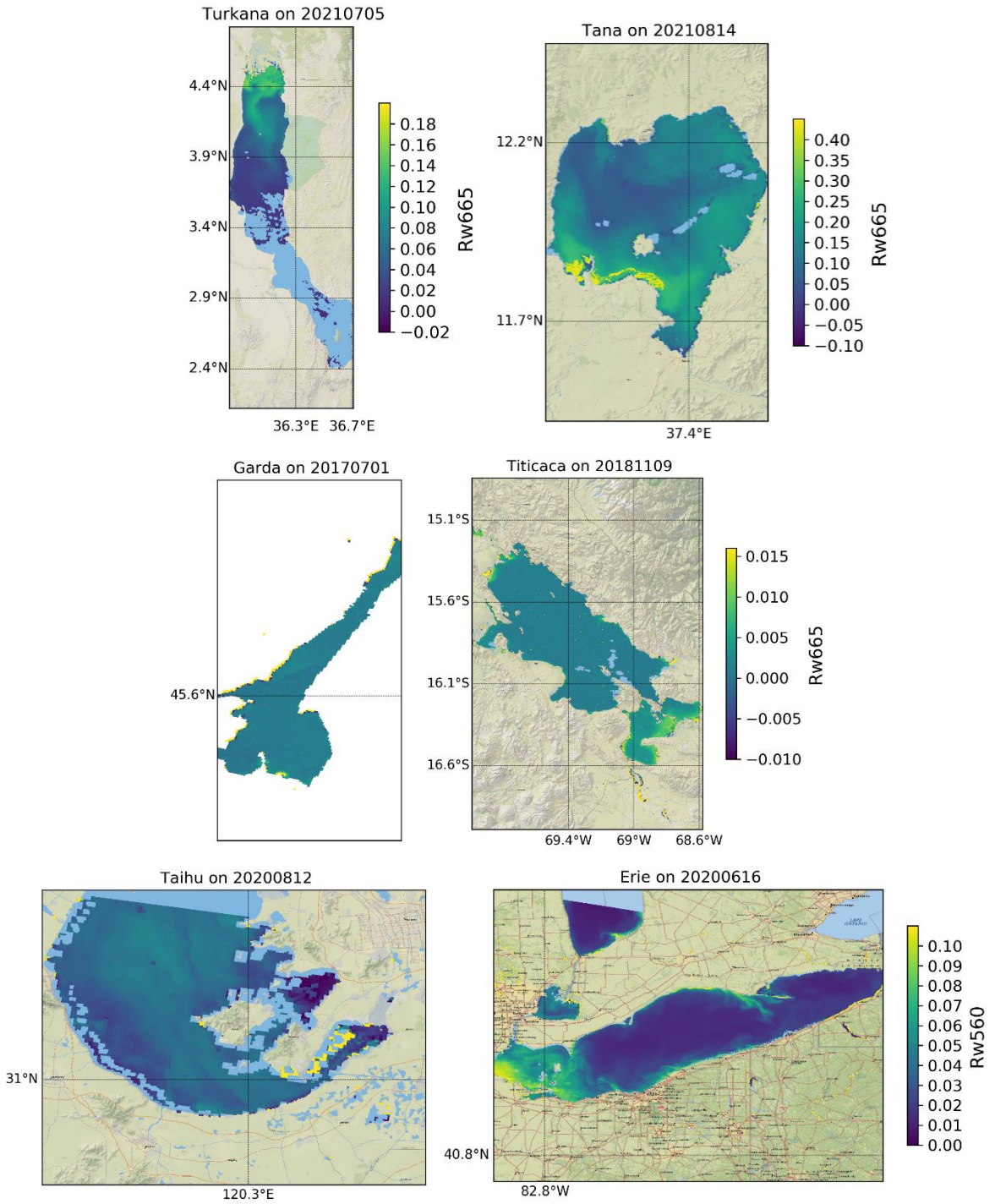

Figure 12: Band $R_w(665)$ LWLR in Lakes Turkana (turbid), Tana (extremely turbid), Garda (clear), Titicaca (clear), Taihu (productive) and Lake Erie (productive).

5.5.2 Weighted blending of biogeochemical variable algorithm outputs

The end-to-end calibration methodology with specific tuning of algorithms corresponding to sets of optical water types is believed to counteract systematic bias in LWLR retrieval. Furthermore, the number of matchup data points for validation of chlorophyll-a and turbidity or suspended matter is much higher than for water-leaving reflectance, benefitting the calibration of these products.

Neil et al. (2019) presented the results of algorithm calibration using exclusively in situ radiometry and substance concentrations determined from water samples. During the GloboLakes project, further tuning of an algorithm set was carried out to calibrate them against atmospherically corrected satellite data (using POLYMER and other candidate atmospheric correction algorithms for MERIS).

Results shown below are from a recent uncertainty characterization analysis of the chlorophyll-*a* product in the *Calimnos* v1.04 data set, which is similar to the result expected in the first climate data record of the Lakes_cci. This exercise has not been repeated for subsequent versions of the CRDP.

These results (Figure 13) clearly show that applying the weighted average of a combination of (two) tuned algorithms for each observed pixel provides a marked improvement over selecting, for each lake and each observation day, the algorithm that is most suitable for the lake-wide predominant optical water type. One clearly visible effect is the need to select algorithms that can deal with a (very) large concentration range, for example to accommodate patchy phytoplankton blooms surrounded by lower biomass conditions. At the scale of the whole lake, bloom-affected pixels are a minority such that mid-range algorithms would perform best for the lake as a whole. A whole-lake algorithm selection can ignore dense (but likely patchy) blooms, shown as saturation at concentrations of approximately 1000 mg m^{-3}, whereas per-pixel algorithm selection allows retrieval up to two orders of magnitude higher. The dynamic algorithm selection approach is therefore preferred as it is better equipped to deal with optical gradients within individual lakes.

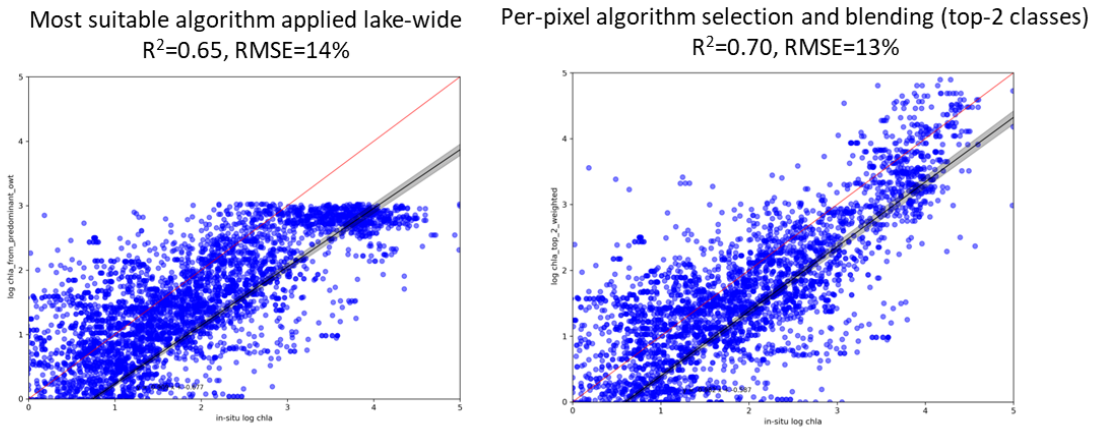

Figure 13: Comparison of the performance of (left) the best chlorophyll-a algorithm for the predominant optical water type of each lake and (right) per-pixel selection and blending of the two highest ranking algorithms based on optical water type membership scores.

5.6 Summary of strengths, weaknesses and limitations

The remarkable variability in the bio-optical properties of inland waters, both regionally and temporally, poses a formidable challenge in developing universally applicable algorithms for

atmospheric correction and biogeochemical substance concentration estimates. Numerous studies have highlighted the potential of integrating an OWT classification step in optically complex waters, followed by type-specific algorithm development, regional tuning, or even algorithm switching, to enhance the accuracy of Chla estimates. Our evaluation of a weighted blended Chla product procedure, utilizing the fuzzy OWT classification framework, demonstrates a significant improvement in retrieval performance compared to that of individually regionally tuned algorithms (Figure 13). This outcome aligns with the expected results from the algorithm tuning exercise conducted by Neil et al. (2019) on in situ reflectance data under the same project, as well as the application of individual algorithms to suitable water bodies in their original publications.

In CRDP V2.1 and before, the water quality algorithms implemented for MERIS and OLCI underwent tuning based on matchups between in situ measurements and MERIS data. This tuning process took into account the extended operational period of MERIS (2002-2012) and the availability of coinciding in situ data from the LIMNADES database. It was assumed that the similarities in radiometric performance and waveband configuration between MERIS and OLCI enable the extrapolation of MERIS results to OLCI.

However, given the extended operational period of OLCI and the development of new algorithms in recent years, a dedicated analysis specific to OLCI became both essential and increasingly feasible. For CRDP v3.0 of Lakes_cci, a comprehensive evaluation of recently published algorithms was conducted for OLCI, as well as for MERIS and MODIS, where similar wavebands were available or slightly adjusted to the closest bands (particularly for MODIS).

In this algorithm validation and calibration process, an additional update involved per-OWT tuning, utilizing matchups that most closely resemble each OWT (within the limitations of having relative sparse in situ matchup datasets available). This dynamic tuning approach enhances the selection of the most suitable algorithm for each satellite pixel, ensuring improved accuracy and adaptability.

It follows from the above that any change in the upstream processing, either through sensor re-calibration, atmospheric correction improvements or pixel identification, may lead to different estimates in LWLR and derives substances, requiring re-tuning of the algorithm library, such as has been implemented for CRDP v3.0. This process is highly dependent on representative in situ reference observations, which are typically scarce. A regular re-analysis of tuning parameters is therefore recommended should extended datasets become available (for example, from releasing embargoed data under open licence).

A known limitation of the methodology described here is an instability in the atmospheric correction step in highly turbid waters, which may lead to unrealistic outcomes. Some of these can be masked and flagged but give rise to a bias in the climate data records towards relatively clearer waters. An update to the atmospheric correction procedure used for CRDPv3.0 is seen to lead to improved results across the sensors, but also to larger deviations from realistic values in cases where the reflectance is likely influenced by observation artefacts such as shallow water, shoreline or reflectance of adjacent land. We anticipate that the development of further use cases will lead to improved quality flagging procedures, and invite data users to suggest any improvements.

5.7 Acknowledgments

All in situ datasets used in this research are obtained from two primary sources: the **LIMNADES** (Lake Bio-optical Measurements and Matchup Data for Remote Sensing) repository, maintained by the University of Stirling (https://limnades.stir.ac.uk – currently not accessible), and the **GLORIA** dataset (GLObal Reflectance community dataset for Imaging and Optical Sensing of Aquatic Environments), which is openly available online (Lehmann et al, 2023). We thank all organizations

and individuals who made in situ data available through specific agreements and licences, whether included or not in the above databases: Agri-food and Biosciences Institute in Northern Ireland; General Directorate of Water Management (OVF, Hungary); Central Transdanubian Inspectorate for Environmental and Natural Protection (Közép-dunántúli Környezetvédelmi és Természetvédelmi Felügyelőség); Balaton Limnological Institute; Finnish Environment Institute; Mariano Bresciani and Claudia Giardino (Institute for Electromagnetic Sensing of the Environment, CNR-IREA, Milano, Italy); Bunkei Matsushita (Faculty of Life and Environmental Sciences, University of Tsukuba, Ibaraki, Japan); Mark W. Matthews (CyanoLakes (Pty) Ltd., Cape Town, South Africa); Daniel Andrade Maciel, Victor Pedroso Curtarelli, Cláudio Clemente Faria Barbosa (National Institute for Space Research, Brazil); Daniela Gurlin (Wisconsin Department of Natural Resources, USA); Enner Alcântara, Thanan Pequeno (São Paulo State University, Brazil); Kersti Kangro, Krista Alikas (Tartu University, Estonia); Mortimer Werther, Daniel Odermatt (Eawag, Switzerland); Sachi Mishra, Deepak Mishra (University of Georgia, USA); Thi Thu Ha Nguyen (Vietnam National University, Vietnam).

5.8 References

Binding, C. E. J. H. Jerome, R. P. Bukata and W. G. Booty. (2010). Suspended particulate matter in Lake Erie derived from MODIS aquatic colour imagery. Int. J. Remote Sens 31(19).

Bouvet M. Ramino F. (2010). Equalization of MERIS L1b products from the 2nd reprocessing, ESA TN TEC-EEP/2009. 521/MB.

Brezonik, P. L., Olmanson, L. G., Finlay, J. C., & Bauer, M. E. (2015). Factors affecting the measurement of CDOM by remote sensing of optically complex inland waters. Remote Sens. Environ., 157, 199-215.

Chen, Z., Hu, C. and Muller-Karger, F. (2007). Monitoring turbidity in Tampa Bay using MODIS/Aqua 250-m imagery. Remote Sens. Environ. 109(2): 207-220.

Dogliotti, A.I., Ruddick, K., Nechad, B., Doxaran, D., & Knaeps, E. (2015). A single algorithm to retrieve turbidity from remotely-sensed data in all coastal and estuarine waters. Remote Sens. Environ., 156: 157-168.

Ficek, D., Zapadka, T., & Dera, J. (2011). Remote sensing reflectance of Pomeranian lakes and the Baltic. Oceanologia, 53(4), 959-970.

Gilerson, A. A. Gitelson, A. A. Zhou, J, Gurlin, D. Moses, W. Ioannou, I. and Ahmed, S. A. (2010). Algorithms for remote estimation of chlorophyll-a in coastal and inland waters using red and near infrared bands. Opt. Express 18(23): 24109-24125.

Gons HJ, Rijkeboer M, Ruddick KG. (2005): Effect of a waveband shift on chlorophyll retrieval from MERIS imagery of inland and coastal waters. J. Plankton Res. 27(1):125-7.

Gordon, H. R. O. B. Brown, R. H. Evans, J. W. Brown, R. C. Smith, K. S. Baker, and D. K. Clark. (1988). A semianalytic radiance model of ocean color. J. Geophys. Res.: Atmos. 93: 10909-10924.

Hu, C., Feng, L., Lee, Z., Franz, B.A., Bailey, S.W., Werdell, P.J., & Proctor, C.W. 2019. Improving satellite global chlorophyll a data products through algorithm refinement and data recovery. J. Geophys. Res. Oceans. 124, 1524-1543.

IOCCG, 2014. Update of the Quasi-Analytical Algorithm (QAA_v6). Available online. http://www.ioccg.org/groups/Software_OCA/QAA_v6_2014209.pdf.

Jiang, D., Matsushita, B., Pahlevan, N., Gurlin, D., Lehmann, M.K., Fichot, C.G., Schalles, J., Loisel, H., Binding, C., & Zhang, Y. (2021). Remotely estimating total suspended solids concentration in clear to extremely turbid waters using a novel semi-analytical method. Remote Sens. Environ. 258: 112386

Jiang D, Scholze J, Liu X, Simis SGH, Stelzer K, Müller D, et al. (2023). A data-driven approach to flag land-affected signals in satellite derived water quality from small lakes. Int. J. Appl. Earth Obs. Geoinf. 2023;117:103188.

Joshi, I. D., & D'Sa, E. J. (2018). An estuarine-tuned quasi-analytical algorithm (QAA-V): assessment and application to satellite estimates of SPM in Galveston Bay following Hurricane Harvey. Biogeosciences, 15(13), 4065-4086.

Klein, K.P., Lantuit, H., Heim, B., Doxaran, D., Juhls, B., Nitze, I., Walch, D., Poste, A., & Søreide, J.E. (2021). The Arctic Nearshore Turbidity Algorithm (ANTA)-A multi sensor turbidity algorithm for Arctic nearshore environments. Sci. Remote Sens. 4, 100036.

Kruse F. A. A. B. Lefkoff, J. W. Boardman, K. B. Heidebrecht, A. T. Shapiro, P. J. Barloon, A. F. H. Goetz. (1993). The spectral image processing system (SIPS)—interactive visualization and analysis of imaging spectrometer data, Remote Sens. Environ, 44(2–3):145-163.

Le, C. F., Li, Y. M., Zha, Y., Sun, D., & Yin, B. (2009). Validation of a quasi-analytical algorithm for highly turbid eutrophic water of Meiliang Bay in Taihu Lake, China. IEEE Transactions on Geoscience and Remote Sensing, 47(8), 2492-2500.

Lee, Z., Hu, C., Shang, S., Du, K., Lewis, M., Arnone, R., & Brewin, R. (2013). Penetration of UV-visible solar radiation in the global oceans: Insights from ocean color remote sensing. Journal of Geophysical Research: Oceans, 118(9), 4241-4255.

Lee, Z., Lubac, B., Werdell, J., & Arnone, R. (2009). An update of the quasi-analytical algorithm (QAA_v5). International Ocean Color Group Software Report, 1, 1-9.

Liu X, Steele C, Simis S, Warren M, Tyler A, Spyrakos E, et al. (2021). Retrieval of Chlorophyll-a concentration and associated product uncertainty in optically diverse lakes and reservoirs. Remote Sens. Environ. 267:112710.

Liu, G., Li, L., Song, K., Li, Y., Lyu, H., Wen, Z., Fang, C., Bi, S., Sun, X., & Wang, Z. 2020. An OLCI-based algorithm for semi-empirically partitioning absorption coefficient and estimating chlorophyll a concentration in various turbid case-2 waters. Remote Sens. Environ. 239, 111648.

Liu, X., Lee, Z., Zhang, Y., Lin, J., Shi, K., Zhou, Y., ... & Sun, Z. (2019). Remote sensing of secchi depth in highly turbid lake waters and its application with MERIS data. Remote Sensing, 11(19), 2226.

Mannino, A., Novak, M. G., Hooker, S. B., Hyde, K., & Aurin, D. (2014). Algorithm development and validation of CDOM properties for estuarine and continental shelf waters along the northeastern US coast. Remote Sens. Environ., 152, 576-602.

Miller, R.L. and McKee, B.A. (2004). Using MODIS Terra 250 m imagery to map concentrations of total suspended matter in coastal waters. Remote Sens. Environ. 93(1-2): 259-266.

Mishra, S. D. R. Mishra, Z. Lee, Craig S. Tucker. (2013). Quantifying cyanobacterial phycocyanin concentration in turbid productive waters: A quasi-analytical approach, Remote Sens. Environ, 133: 141-151.

Moore, TS. JW. Campbell and Hui Feng. (2001). A fuzzy logic classification scheme for selecting and blending satellite ocean color algorithms. IEEE Trans. Geosci. Remote Sens. 39(8) 1764-1776.

Morel, A. (1974). Optical properties of pure water and pure sea water. In: Jerlov MG, Nielsen ES, editors. Optical Aspects of Oceanography. New York: Academic Press; 1974. p. 1–24.

Nechad, B. Dogliotti, A. I. Ruddick, K. G. Doxaran, D. (2016). Particulate Backscattering and suspended matter concentration retrieval from remote-sensed turbidity in various coastal and riverine turbid waters. Proceedings of ESA Living Planet Symposium, Prague, 9-13 May 2016, ESA-SP 740.

Nechad, B. Ruddick, K. G, Park, Y. (2010). Calibration and validation of a generic multisensor algorithm for mapping of total suspended matter in turbid waters. Remote Sens. Environ. 114 (2010) 854–866.

Nechad, B., Ruddick, K., & Neukermans, G. (2009). Calibration and validation of a generic multisensor algorithm for mapping of turbidity in coastal waters. In, *Remote Sensing of the Ocean, Sea Ice, and Large Water Regions 2009* (pp. 161-171): SPIE

Neil, C. Spyrakos, E. Hunter, PD, Tyler, AN. (2019). A global approach for chlorophyll-a retrieval across optically complex inland waters based on optical water types. Remote Sens. Environ. 229:159-178.10.1016/j.rse.2019.04.027

Ondrusek, M., Stengel, E., Kinkade, C.S., Vogel, R.L., Keegstra, P., Hunter, C. and Kim, C. (2012). The development of a new optical total suspended matter algorithm for the Chesapeake Bay. Remote Sens. Environ. 119243-254.

O'Reilly, J.E., & Werdell, P.J. 2019. Chlorophyll algorithms for ocean color sensors-OC4, OC5 & OC6. Remote Sens. Environ. 229, 32-47.

Pahlevan, N., Smith, B., Schalles, J., Binding, C., Cao, Z., Ma, R., Alikas, K., Kangro, K., Gurlin, D., & Hà, N. 2020. Seamless retrievals of chlorophyll-a from Sentinel-2 (MSI) and Sentinel-3 (OLCI) in inland and coastal waters: A machine-learning approach. Remote Sens. Environ. 240, 111604.

Pahlevan, N., Smith, B., Alikas, K., Anstee, J., Barbosa, C., Binding, C., Bresciani, M., Cremella, B., Giardino, C., Gurlin, D., Fernandez, V., Jamet, C., Kangro, K., Lehmann, M. K., Loisel, H., Matsushita, B., Hà, N., Olmanson, L., Potvin, G., . . . Ruiz-Verdù, A. (2022). Simultaneous retrieval of selected optical water quality indicators from Landsat-8, Sentinel-2, and Sentinel-3. Remote Sensing of Environment, 270, 112860. https://doi.org/https://doi.org/10.1016/j.rse.2021.112860

Park Y. J. and Ruddick K. Model of remote-sensing reflectance including bidirectional effects for case 1 and case 2 waters. (2005). Appl. Optics. 2005; 44(7):1236-49. doi:10.1364/ao.44.001236

Pedroso Curtarelli, V., Clemente Faria Barbosa, C., Andrade Maciel, D., Flores Júnior, R., Menino Carlos, F., de Moraes Novo, E. M. L., ... & da Silva, E. F. F. (2020). Diffuse attenuation of clear water tropical reservoir: A remote sensing semi-analytical approach. Remote Sensing, 12(17), 2828.

Petus, C., Chust, G., Gohin, F., Doxaran, D., Froidefond, J.M. and Sagarminaga, Y. (2010). Estimating turbidity and total suspended matter in the Adour River plume (South Bay of Biscay) using MODIS 250-m imagery. Cont. Shelf Res. 30(5): 379-392.

Pitarch, J., & Vanhellemont, Q. (2021). The QAA-RGB: A universal three-band absorption and backscattering retrieval algorithm for high resolution satellite sensors. Development and implementation in ACOLITE. Remote Sensing of Environment, 265, 112667.

Qin P, Simis S, Tilstone GH. (2017). Radiometric validation of atmospheric correction for MERIS in the Baltic Sea based on continuous observations from ships and AERONET-OC. Remote Sens. Environ. 200:263-80.

Rodrigues, T., Alcântara, E., Watanabe, F., & Imai, N. (2017). Retrieval of Secchi disk depth from a reservoir using a semi-analytical scheme. Remote Sensing of Environment, 198, 213-228.

Roettgers, R. Doerffer, R. McKee, D. and Schoenfeld, W. (2011). Pure water spectral absorption, scattering, and real part of refractive index model. ESA Water radiance project. From www.brockmann-consult.de/beam-wiki/download/attachments/17563679/WOPP.zip?version=1&modificationDate=1299075673760

Ruescas, A. B. Brockmann, C. Stelzer, K. Tilstone, G. H. Beltran, J. (2014). DUE CoastColour Validation Report (p. 58). Geesthacht, Germany: Brockmann Consult. Retrieved from http://www.coastcolour.org/documents/DEL-27%20Validation%20Report_v1.pdf.

Shanmugam, P. (2011). New models for retrieving and partitioning the colored dissolved organic matter in the global ocean: Implications for remote sensing. Remote Sens. Environ., 115(6), 1501-1521.

Smith, M.E., Lain, L.R., & Bernard, S. 2018. An optimized chlorophyll a switching algorithm for MERIS and OLCI in phytoplankton-dominated waters. Remote Sens. Environ. 215, 217-227.

Spyrakos E, O'Donnell R, Hunter PD, Miller C, Scott M, Simis S, et al. (2018). Optical types of inland and coastal waters. Limnol. Oceanogr. 63(2). doi: 10. 1002/lno. 10674.

Steinmetz F, Deschamps P-Y, Ramon D. Atmospheric correction in presence of sun glint: application to MERIS. (2011). Optics Express. 19(10):9783-800. doi: 10. 1364/oe. 19. 009783

Steinmetz, F. (2018): ATBD v1 – Evolution of Polymer Atmospheric correction within Copernicus Global Land Service – Inland Water products. On request

Steinmetz, F. Ramon, D. Deschamps, P-Y (2016). ATBD v1 – Polymer atmospheric correction algorithm, D2. 3 OC-CCI project http://www.esa-oceancolour-cci.org/?q=webfm_send/658

Tiwari, S., & Shanmugam, P. (2011). An optical model for the remote sensing of coloured dissolved organic matter in coastal/ocean waters. Estuar. Coast. Shelf Sci., 93, 396-402

Uudeberg, K., Aavaste, A., Kõks, K.-L., Ansper, A., Uusõue, M., Kangro, K., Ansko, I., Ligi, M., Toming, K., & Reinart, A. 2020. Optical water type guided approach to estimate optical water quality parameters. Remote Sens. 12, 931.

Vantrepotte, V. H. Loisel , X. Mériaux, G. Neukermans, D. Dessailly, C. Jamet, E. Gensac, and A. Gardel, (2011). Seasonal and inter-annual (2002-2010) variability of the suspended particulate matter as retrieved from satellite ocean color sensor over the French Guiana coastal waters. J Coast Res. SI 64 (Proceedings of the 11th International Coastal Symposium), – . Szczecin, Poland, ISSN 0749-0208

Wang, Y., Shen, F., Sokoletsky, L., & Sun, X. (2017). Validation and calibration of QAA algorithm for CDOM absorption retrieval in the Changjiang (Yangtze) estuarine and coastal waters. Remote Sensing, 9(11), 1192.

Wang, Y., Shen, F., Sokoletsky, L., & Sun, X. (2017). Validation and calibration of QAA algorithm for CDOM absorption retrieval in the Changjiang (Yangtze) estuarine and coastal waters. Remote Sens., 9(11), 1192.

Warren MA, Simis SGH, Martinez-Vicente V, Poser K, Bresciani M, Alikas K, et al. (2019). Assessment of atmospheric correction algorithms for the Sentinel-2A MultiSpectral Imager over coastal and inland waters. Remote Sens. Environ. 225:267-89.

Werther, M., Odermatt, D., Simis, S.G., Gurlin, D., Lehmann, M.K., Kutser, T., Gupana, R., Varley, A., Hunter, P.D., & Tyler, A.N.J.R.S.o.E. 2022. A Bayesian approach for remote sensing of chlorophyll-a and associated retrieval uncertainty in oligotrophic and mesotrophic lakes 283, 113295.

Yang, W., Matsushita, B., Chen, J., Yoshimura, K., & Fukushima, T. (2013). Retrieval of inherent optical properties for turbid inland waters from remote-sensing reflectance. IEEE Transactions on Geoscience and Remote Sensing, 51(6), 3761-3773.

Zhang, M., Tang, J., Dong, Q., Song, Q. and Ding, J. (2010). Retrieval of total suspended matter concentration in the Yellow and East China Seas from MODIS imagery. Remote Sens. Environ. 114(2): 392-403.

Zhang, Y. K. Shi, X. Liu, Y. Zhou, B. Qin. (2014). Lake topography and wind waves determining seasonal-spatial dynamics of total suspended matter in turbid lake Taihu, China: assessment using long-term high-resolution MERIS data. PLoS ONE 9(5):e98055. doi:10.1371/journal.pone.0098055.

Zolfaghari, K., Pahlevan, N., Simis, S. G. H., O'Shea, R. E., & Duguay, C. R. (2022). Sensitivity of remotely sensed pigment concentration via Mixture Density Networks (MDNs) to uncertainties from atmospheric correction. Journal of Great Lakes Research. https://doi.org/https://doi.org/10.1016/j.jglr.2022.12.010.

6 Lake Ice cover – LIC

6.1 Description

Lake ice cover corresponds to the extent (or area) of a lake covered by ice. The generation of a lake ice cover (LIC) product from satellite observations requires implementation of a retrieval algorithm that can correctly label pixels as either ice (either snow-free or snow-covered), open water or cloud. From such a product, one can determine ice cover dynamcis and duration at the pixel scale (e.g., ice-on and ice-off dates) and at the lake-wide scale (complete freeze-over (CFO) and water clear of ice (WCI)) (Duguay et al. 2015). From a climate perspective, determination of ice onset (date of first pixel covered by ice), CFO, melt onset (date of first pixel with open water) and WCI are of most relevance to capture important ice events during the freeze-up and break-up periods. Duration of freeze-up and break-up periods and duration of ice cover over a full ice season can be determined from these dates.

The LIC product v3.0.0 generated for Lakes_cci uses MODIS (Terra and Aqua) data to provide the most consistent and longest historical record globally to date (2000-2022). The full processing chain and retrieval algorithm are described below.

6.2 Algorithm definition

Prior to the main processing chain, the Canadian Lake Ice Model (CLIMo) is applied to help determine which lakes of the Lakes_cci harmonised product (total 2024 lakes) could have formed ice or have remained ice-free at any time over the 2000-2023 period. CLIMo (Duguay et al. 2003) is a one-dimensional thermodynamic model capable of simulating ice phenology events (ice-on and ice-off dates), ice thickness and temperature, and all components of the energy/radiation balance equations during the ice and open water seasons at a daily timestep. Input data to drive CLIMo include mean daily air temperature (°C), wind speed (m s^{-1}), relative humidity (%), snowfall (or depth) (m), and cloud cover (in tenth). Here, ERA5 reanalysis hourly data on single levels (25 km) were used to generate inputs required for CLIMo simulations for each of the 2024 lakes. ERA5 hourly data including wind speed, air temperature, relative humidity, and cloud cover were converted to daily values (each day to be the average of 24 hours). In addition, snow depth of daily accumulation was extracted from the ERA5 hourly data. As a second check to the possible formation of ice on any of the lakes, lake ice depth data provided by ERA5 were also utilised. Ice cover was deemed possible to have formed on a lake if ice depth was determined to have reached a thickness greater than 0.001 m on any day from either CLIMo or ERA5.

Ice was determined to have formed on a common set of 1390 lakes by both CLIMo and from the ERA5 lake ice depth data. 558 lakes were determined not to form any ice (ice-free) from both sources. However, there were also discrepancies between CLIMo simulations and ERA5 ice depth data for 76 of the 2024 lakes. 24 lakes were identified to have formed ice from CLIMo but not ERA5 and vice versa for 52 lakes. Hence, as a third check, a number of lakes (largely located at the southern limit of where ice could potentially form during a cold winter in the Northern Hemisphere and in mountainous regions of both the Northern and Southern hemispheres) were inspected manually through interpretation of MODIS RGB images to determine if any of these lakes had formed ice between 2000 and 2023.

As a result of the process described above, 1391 of 2024 lakes were identified as forming ice and 633 not forming ice. Only lakes that were identified as forming ice are included in the final output for the LIC product.

An overview of the implemented processing chain is given in Figure 14Figure 14. It includes three modules: data import, retrieval, and data export. Data is processed one day at a time. As part of global initialization, a water mask is loaded. Then, the data for each day is processed. One execution of the processing chain processes one day of data.

Six MODIS (Terra/Aqua) TOA reflectance bands, a solar zenith angle (SZA) band, and a TOA emission band are used for feature retrieval (i.e. for labelling as water, ice, or cloud) (Wu et al., 2021). The reflectance bands are MOD02QKM/MYD02QKM at 250 m (band 1: 0.645 µm and band 2: 0.858µm) and MOD02HKM/MYD02HKM at 500 m (band 3: 0.469µm; band 4: 0.555µm; band 6: 1.640 µm; band 7: 2.130 µm) resolutions. The emission band is MOD021KM/MYD021KM at 1 KM band 31: 10.780 - 11.280 µm.

MODIS pixels are initially cast to the coordinates of the static CCI lake mask (1/120-degree resolution, Carrea et al., 2015) to ensure spatial consistency between ECVs. Pixels that do not have a match with a lake mask pixel are omitted. Pixels of interest are classified and labelled as cloud, ice or water from a random forest (RF) algorithm (Wu et al., 2021). After retrieval, pixels with SZA higher than 85 degrees are omitted from the final product and flagged as missing/unclassified. . The MODIS band 31 is used to correct for misclassifications of ice/water. For pixels that are classified as water, but the temperature is <268.15 K, the pixel is reclassified as ice. For pixels that are classified as ice, but the temperature is >278.15 K, the pixel is reclassified as water. Aggregation is performed by taking a majority vote between ice and water, ties broken by selecting water. If there are zero ice and water pixels, then the cell is labelled as cloud if there are non-zero cloud pixels; otherwise, the output cell is flagged as missing/unclassified. After aggregation is performed, ice cover extent (the fractional ice cover) is calculated omitting pixels for a lake that are classified as cloud cover.

More specifically, the processing steps presented in Figure 14Figure 14 are:

- Load TOA reflectance and emission bands (1, 2, 3, 4, 6, 7, 31, and SZA) from MODIS Level 1B calibrated radiances product (MOD02/MYD02), Collection 6.1.
- Match latitude and longitude coordinates from the TOA products to the closest coordinates from the Lake CCI water mask (1/120 degrees resolution).
- Label pixels of interest from application of RF algorithm for the detection of clouds, ice, and open water.
- Filter out pixels with a SZA >85 degrees and apply temperature filters to correct ice and water pixels where high or low temperatures are found.
- Aggregate pixels by majority vote
- Determine LIC extent excluding cloud pixels, total cloud cover, and lake ice area for each lake where the RF algorithm was applied.
- Write and export the daily lake ice cover product in the required format (NetCDF) with metadata.

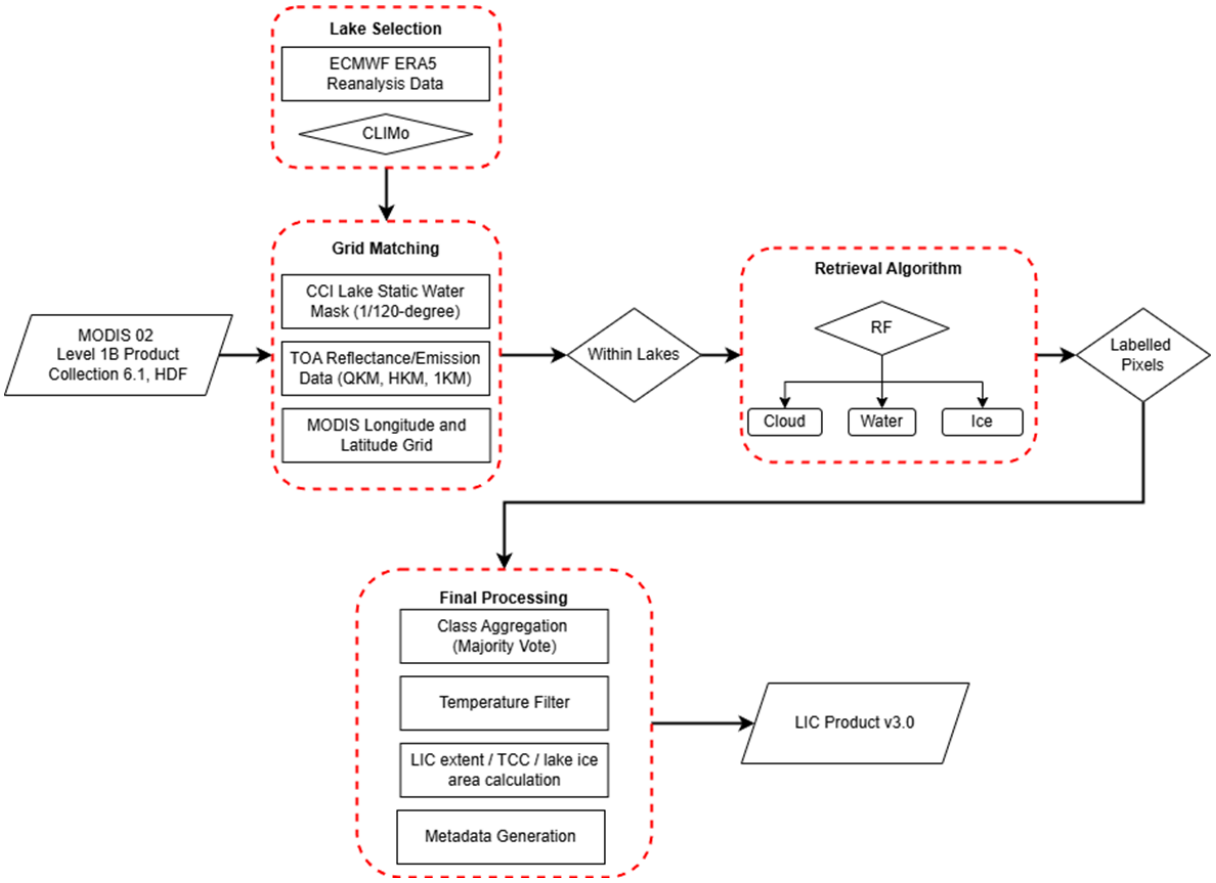

Figure 14: Overview of the processing chain for generation of MODIS LIC daily product. RF stands for random forest

6.2.1 Input Data

Satellite input data:

- MODIS Terra/Aqua Level 1B calibrated radiances product (MOD02/MYD02), Collection 6.1 (TOA reflectance data) stored in two separate files as a function of spatial resolution: MOD02QKM/MYD02QKM (250 m, bands 1-2) and MOD02HKM/MYD02HKM (500 m, bands: 3-4, 6-7). SZA and band 31 from MOD021KM/MYD021KM is also used.

Lake water boundaries:

- Static Lake Mask at 1/120 degree resolution, as used throughout the Lakes_cci

6.2.2 Output Data

The output data are produced in the harmonized grid format. The edge of each grid cell subtends 1/120 degrees latitude or longitude. The list of variables included in the LIC product are provided in Table 24Table 24.

Table 24: Output variables in LIC product

Band	Variable name	Description	Values
1	Lake Cover Class	Assigned classifications	1: Water, 2: ice, 3: cloud
2	LIC Process Flag	User notice flags	1: No Flag, 2: Unclassified/Missing, 3: LIC High Temp
3	LIC Class Agreement	Number of swaths that agree with assigned classification	0 - 255
4	LIC MODIS Overlap	Number of swaths that overlap for a grid cell	0 – 255
5	LIC Random Forest Total Uncertainty	Random forest total uncertainty for each grid cell	0 – 2
6	LIC Random Forest Quality Level	Quality flag assigned to grid cell	1: Lowest quality, 2: Poor quality, 3: Medium quality, 4: Good quality, 5: Best quality
7	Fractional Ice Cover	Fractional ice extent excluding cloud cover	0 – 100
8	Total Cloud Cover	Cloud cover percentage for each lake	0 – 100
9	Area of Lake Covered by Ice	Area of the lake covered by ice in km^2	0 - 83000

6.2.3 Retrieval Algorithm

The retrieval algorithm is a random forest (RF) classifier. As an ensemble approach, RF integrates decision trees developed by bagging samples to improve the limitations of the single-tree structure (Breiman, 2001). The bagging creates several subsets randomly from training samples with replacement (i.e. a

sample can be collected several times in the same subset whereas other samples are probably not selected in this subset). Subsequently, each data subset is used to train a decision tree. For building a single tree, a random sample with a number of variables is chosen as split candidates from all variables. The number of variables available to a split is one of the key RF hyperparameters, denoted *mtry*. For the whole RF model, the number of trees (*ntree*) is defined a priori to develop various independent classifier outputs. The final class of each unknown sample is assigned by the majority vote of all outputs from the trees.

RF was found to outperform two other machine learning algorithms (multinomial logistic regression, MLR, and support vector machine, SVM) and comparable to gradient boosting trees (GBT) for lake ice cover, open water and cloud classification in a recent paper by the developers of the current LIC product (Wu et al., 2021). While RF and GBT provided similar results following a comprehensive accuracy assessment (cross validation (CV): random k-fold as well as spatial and temporal CV), the former was selected for LIC product generation since it was determined to be less sensitive to the to the choice of hyperparameters necessary for classification compared to GBT, MLR and SVM.

To develop and validate the retrieval algorithm, 17 lakes distributed across the Northern Hemisphere were selected (Figure 15Figure 15 and Table 25Table 25). Training, testing and validation of the four machine learning algorithms found that RF with a combination of visible, near infrared, and mid infrared bands was the best choice for LIC product (Figure 16Figure 16).

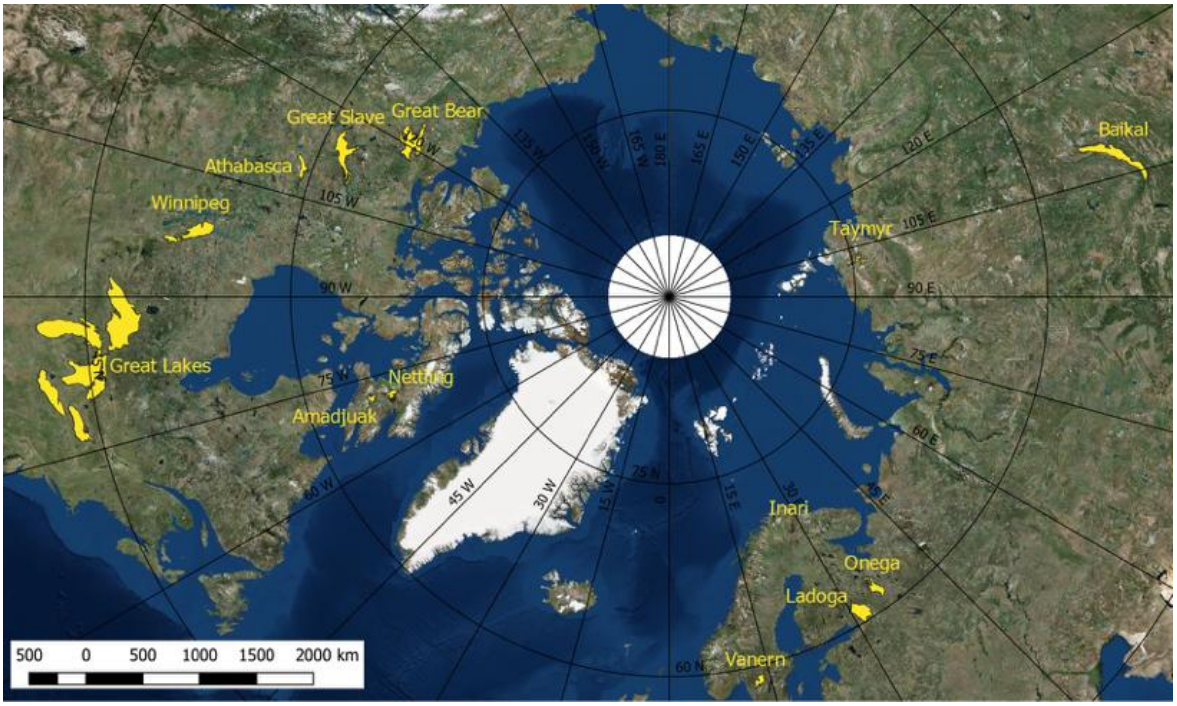

Figure 15: Geographical distribution of lakes used for LIC algorithm development and validation

Table 25: List of lakes for LIC algorithm development and (internal) validation

Lake	Country	Latitude	Longitude	Elevation (m)	Area (km²)
Amadjuak	Canada	64.925	-71.149	113	3,115
Athabasca	Canada	59.424	-109.34	213	7,900
Baikal	Russia	53.525	108.207	456	31,500
Erie	Canada/USA	42.209	-81.246	174	25,821
Great Bear	Canada	66.024	-120.61	186	31,153
Great Slave	Canada	61.579	-114.196	156	28,568
Huron	Canada/USA	44.918	-82.455	176	59,570
Inari	Finland	69.048	27.876	118	1,040

Ladoga	Russia	60.83	31.578	5	18,135
Michigan	USA	43.862	-87.093	177	58,016
Nettilling	Canada	66.42	-70.28	30	5,542
Onega	Russia	61.75	35.407	35	9,890
Ontario	Canada/USA	43.636	-77.727	75	19,009
Superior	Canada/USA	47.945	-87.32	183	82,367
Taymyr	Russia	74.538	101.639	6	4,560
Vanern	Sweden	58.88	13.22	44	5,650
Winnipeg	Canada	52.421	-97.677	217	23,750

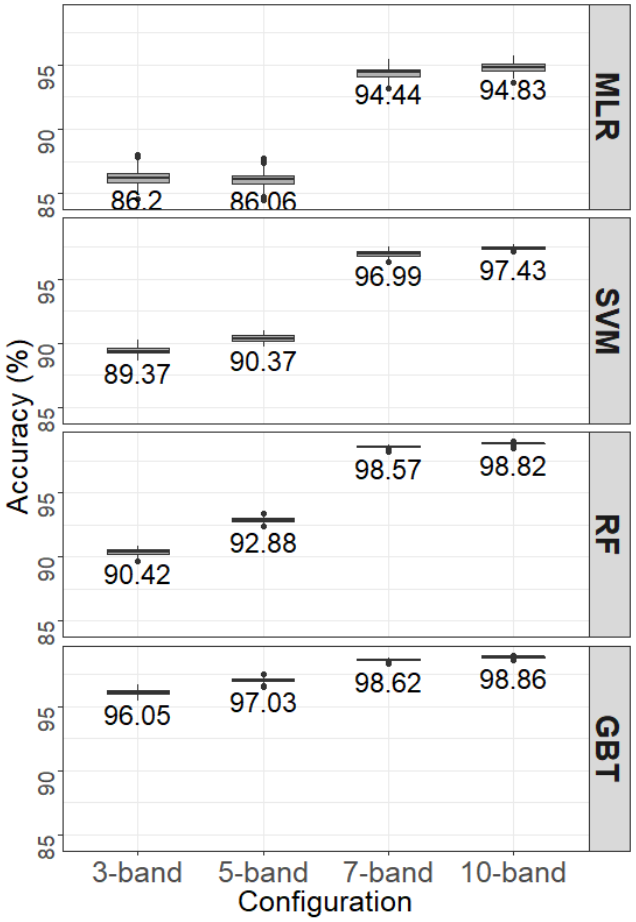

Figure 16: Comparison of classification accuracies (%) obtained with different band configurations across classifiers. The 7-band combination using RF is the one retained for generation of the LIC v2.1 product (Wu et al., 2021)

6.2.4 Random Forest Uncertainty

For LIC v3.0 to provide further quantification of the RF uncertainty, per-pixel uncertainty is provided. The approach used for the LIC v3.0 is based on work from Shaker and Hüllermeier, 2016, and Saberi et al., 2025. This value provides a numerical measure of how uncertain the model is about a specific prediction made. This approach relies on Shannon entropy and the sum of conditional entropy and mutual information (Depeweg et al., 2018). Total uncertainty (TU) is calculated as,

$$TU = H[\bar{\rho}] = -\sum_{k=1}^{K} \bar{p}_k \cdot \log_2 \bar{p}_k$$

where *H* denotes Shannon entropy and the posterior predictive distribution = ( ) is obtained through Bayesian model averaging, or the averaging of the probability predictions made by the individual models , weighted by their posterior probability,

$$\bar{\rho} = \int_{\mathcal{H}} h(x)\,dQ(h)$$

where *h* is a single predictor, *Q* is the second-order probability distribution, and is the hypothesis space. This process can be further extended to determine aleatoric (inherent) uncertainty and systematic or epistemic uncertainty. These data are not provided as part of the LIC v3.0 and are not detailed here.

For the calculation of uncertainty in LIC v3.0 the process is done through an ensemble method (Saberi et al., 2025). To determine the predicted probability distribution from the RF model, the relative frequency of the samples of each class within the leaf node are used. The leaf node, or terminal node, is the point at which a final decision is made using the random forest classifier (Saberi et al., 2025). Finally, aggregation is performed by computing the average over the probability distributions from the individual tress (Saberi et al., 2025). Example of the total uncertainty available in LIC v3.0 is shown in Figure 17. The higher uncertainty is found near class boundaries where there is less certainty about the retrieval made.

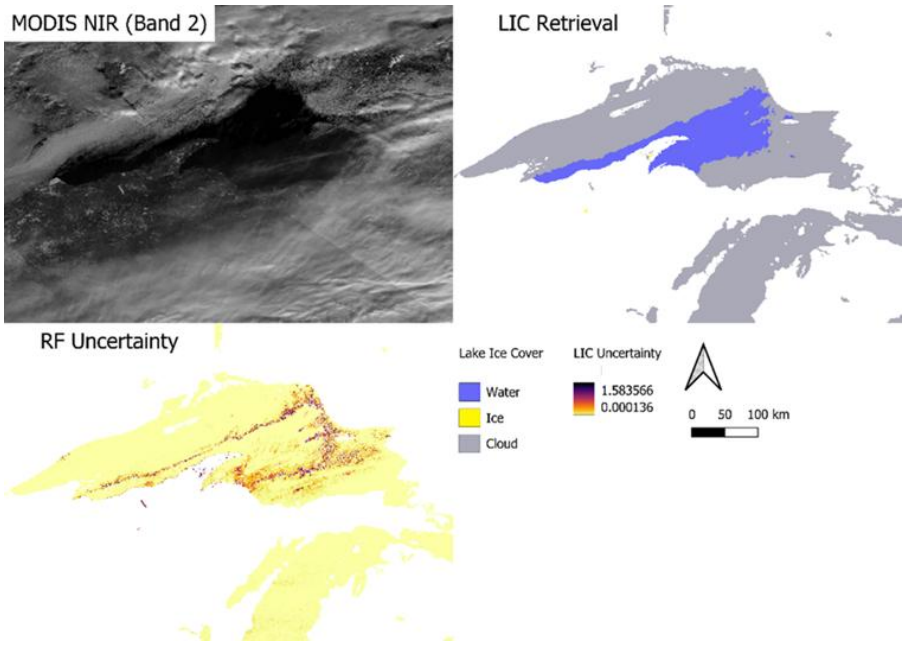

Figure 17 Example of RF uncertainty for Lake Superior 1 January 2021.

6.2.5 Temperature Filter

Following the retrieval decision based on the majority vote, a temperature filter is applied to correct for misclassifications. Common examples include turbid lakes in the spring/summer where sediment heavy water is misclassified as ice due to similarities in spectral reflectance and for thinner cloud covers/wildfire smoke that may be misclassified as ice. The temperature filter uses MODIS band 31 to address these issues. For pixels where the temperature is >283.15 K but ice is retrieved the classification is corrected to water. The buffer of 10 K is employed to not avoid pixels where a change of state has not occurred.

Changes made due to the temperature filter are recorded in the process flag.

6.2.6 Random Forest Quality Score

Utilizing information about the MODIS swaths and random forest uncertainty, a quality score for the LIC product is provided. To provide a quality score that is comparable within and between days, uncertainty values are normalized and weighted based on the percentage of overlapping swaths that agree with the retrieved ice class. This is calculated as follows,

$$RF\ Quality\ = \frac{Total\ Uncertainty}{Maximum\ Uncertainty} \cdot \frac{Number\ of\ Swaths\ in\ Agreement}{Total\ Number\ of\ Overlapping\ Swaths}$$

Maximum uncertainty is equivalent to the where n is the number of classes. In this application the maximum uncertainty is equivalent to 1.585. This value is used to maintain consistency across images and models. The quality score is a function of both the model uncertainty as well as the overlapping swaths, higher quality scores are typically assigned where more data is used to make the final decision. For example, a pixel with a low uncertainty where only 1 out of 3 swaths agrees with the retrieved value will receive a lower quality score.

Quality is ranked on a scale of 1 to 5, where 1 is the lowest quality and 5 is the highest quality.

6.2.7 Lake-wide Statistics

In the CRDP v3.0 new lake-wide statistics are included. Ice fraction provides a lake-wide value for the fraction of ice cover excluding cloud grid cells. This is calculated by dividing the total number of ice grid cells by the total number of lake grid cells excluding the number of cloud cells identified. The value is provided as a percentage. The area of each lake covered by ice (in km^2) is also provided. This is calculated by multiplying the lake area by the fraction of ice cover. For area of ice coverage, clouds are included as part of the total number of lake grid cells.

Additionally, lake-wide total cloud cover is also provided as a percent which is calculated by dividing the number of cloud grid cells by the total number of lake grid cells. This can be useful for removing over or under-estimation of ice fraction and areal ice coverage. The recommendation is to discard observations where cloud coverage exceeds 70%.

6.3 Product Validation

Quality assessment of the LIC product is accomplished by comparing retrieved ice, water and cloud pixels against those obtained from visual interpretation of RGB colour composite images from MODIS Terra Level 1B calibrated radiances (TOA reflectance data). The images are selected to include several lakes across the Northern Hemisphere over a few ice seasons of MODIS Terra record (2000 - 2023). The product is also validated using the Multisensor Snow and Ice Mapping System (IMS). This is done by comparing ice cover extent between the CCI product and IMS product. Pixels that are classified as cloud cover in the CCI product are omitted.

6.4 Summary of the strengths, weaknesses and limitations

The random forest algorithm (RF) was selected for LIC product generation since it outperforms threshold-based approaches (e.g., NASA Snow product) and other machine learning classifiers, such as multinomial logistic regression, and support vector machine (Wu et al., 2021). High overall accuracy (>95%) has been achieved with the RF classifier in both spatial and temporal transferability assessments (Wu et al., 2021). CRDCP v3.0 also includes RF total uncertainty which provides the user with insight into the confidence of the individual pixel retrievals. To further strengthen this, the LIC quality score provides an indication of both uncertainty and swath agreement.

As with any lake product generated from optical data, the presence of clouds as well as extensive cloud cover periods and low solar illumination angles, particularly during the fall freeze-up at high latitudes,

introduce classification errors and limit the retrieval of open water and ice cover for many days of the year. . For example, no retrieval is performed when the solar zenith angle is >85 degrees; a limitation due to the use of MODIS shortwave bands that record very low surface reflectance during ice formation in late fall and wintertime. In CRDCP v3.0, temperature filters are introduced to address misclassifications of features such as highly turbid lakes or sections of lakes that are misclassified as ice-covered during the open water season. Issues persist in confusion between blue clear ice/open water in the spring months. Future versions of the product may explore the use of other climate data to further improve identification and correction of misclassifications.

6.5 References

Breiman, L. (2001). Random forests. Machine Learning, 45(1), 5–32. https://doi.org/10.1023/A:1010933404324.

Carrea, L., Embury, O., & Merchant, C. J. (2015). Datasets related to in-land water for limnology and remote sensing applications: distance-to-land, distance-to-water, water-body identifier and lake centre co-ordinates. Geoscience Data Journal, 2(2), 83-97.

Depeweg, S., Hernandez-Lobato, J., Doshi-Velez, F., and Udluft, S. (2018) Decomposition of uncertainty in Bayesian deep learning for efficient and risk-sensitive learning. in Proceedings ICML, Stockholm, Sweden.

Duguay, C. R. Bernier, M. Gauthier, Y. & Kouraev, A. (2015). Remote sensing of lake and river ice. In Remote Sensing of the Cryosphere, Edited by M. Tedesco. Wiley-Blackwell (Oxford, UK), 273-306.

Duguay, C.R., Flato, G.M., Jeffries, M.O., Ménard, P., Morris, K. & Rouse, W.R. (2003). Ice cover variability on shallow lakes at high latitudes: Model simulations and observations. Hydrological Processes, 17(17), 3465-3483.

Saberi, N., Shaker, M.H., Duguay, C., Scott, K.A., & Hullermeier, E. (2025). Uncertainty estimation of lake ice cover maps from a random forest classifier using MODIS TOA reflectance data. IEEE Journal of Selected Topics in Applied Earth Observations and Remote Sensing, 18: 5919-5927, doi: 10.1109/JSTARS.2024.3518306.

Shaker, M. and Hüllermeier, E. (2020). Aleatoric and epistemic uncertainty with random forests. In Proceedings IDA, 18th International Symposium on Intelligent Data Analysis, ser. LNCS, vol. 12080. Konstanz, Germany: Springer, 444–456.

Wu, Y., Duguay, C.R. & Xu, L. (2021). Assessment of machine learning classifiers for global lake ice cover mapping from MODIS TOA reflectance data. Remote Sensing of Environment, 253, 112206, https://doi.org/10.1016/j.rse.2020.112206.

7 Lake Ice Thickness- LIT

Lake ice is a major landscape feature in the winter season at northern latitudes and plays a key role in climate moderation and the energy balance (Brown and Duguay, 2010). Lake ice conditions, particularly the length of the ice season and ice thickness, have a significant impact on the economy of northern regions through their influence on transportation, travel, fishing, and recreation activities (Ghiasi et al., 2020). Therefore, accurate knowledge about lake ice properties, such as lake ice thickness (LIT), is necessary. Furthermore, LIT is a key climate change indicator recognized as one of six thematic variables under the GCOS Essential Climate Variable (ECV) Lake. LIT integrates changes in surface air temperature and on-ice snow mass (depth and density) (Brown and Duguay, 2011). Decreasing trends in maximum (late winter) ice thickness have been documented in recent years for lakes on the North Slope of Alaska (ca. 20 cm 1991-2011; Surdu et al., 2014) and in Russia (10-15% decrease 1980-2010; Vuglinsky, 2017). Yet, field LIT measurements are sparse in both space and time, and many northern countries have seen an erosion in their in situ observational networks over the last four decades. Therefore, there is a pressing need to use satellite remote sensing to provide broad-scale and regular monitoring of LIT in the face of climate change (see Murfitt et al 2021 for a recent review).

This section contains a detailed description of a novel physically-based algorithm for the retrieval of LIT founded on the exploitation of Ku-band radar altimetry waveforms in Low Resolution Mode (LRM) that contain information correlated with the seasonal evolution of ice thickness over freshwater lakes. The mathematical formulations, processing steps, input and output data as well as statistical metrics used for quality assessment/validation of each algorithm are provided in the next two sections. A detailed description of the algorithm and results are provided in [Mangilli et al. 2022].

7.1 Description

The radar waveforms from altimetry missions show a specific signature on ice covered lakes. For LRM waveforms, this signature corresponds to a step-like break in the leading edge. This break is understood as the double back-scattering of the radar wave at 1) the snow-ice interface and at 2) the ice-water interface. The width of the step in the leading edge is directly related to the ice thickness. An illustrative example is shown in the right plot of Figure 18 for Jason-3 waveform data over the Great Slave Lake (Canada) in February 2020. When the waveforms, measured along track each ~50 milliseconds (~350 meters), are lined up into a radar echogram, the step-like feature associated with the LIT translates into a distinguishable fringe, as shown in the left plot of Figure 18.

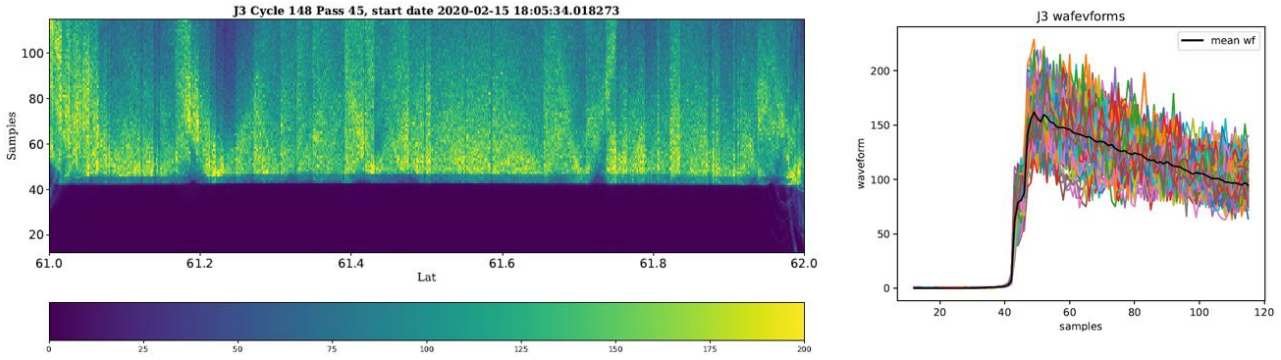

Figure 18: Example of LRM radar echogram (left) and waveforms (right) over the iced-covered Great Slave Lake. Jason-3 data (pass 45, cycle 148, February 2020).

Given the specific signature of the LIT in radar LRM echograms, a physical model can be constructed, based on Brownian modelling of the radar echoes over an ocean surface, where the waveform is described as the sum of two backscattered echoes. The radar waveform, as a function of the range gates, S(x), can therefore be defined as the sum of two positive definite error functions:

$$S_1(\mathbf{x}) = \mathrm{erf}(\mathbf{x} - x_c) + 1$$
$$S_2(\mathbf{x}) = \mathrm{erf}(\mathbf{x} - x_c - \Delta_{ICE}^{gates}) + 1 \qquad [7.1]$$

where x is the range gates array of N gates samples, erf(z) is the error function:

$$\mathrm{erf}(z) = \frac{2}{\sqrt{\pi}} \int_0^z e^{-t^2} dt \qquad [7.2]$$

x_c is the central gate of the first echo and Δ_{ICE}^{gates} is the ice thickness expressed in number of gates, that is, the width of the step in the leading edge. The modelled waveform takes the form:

$$S(\mathbf{x}) = [S_1(\mathbf{x}) + \alpha S_2(\mathbf{x})]\, e^{-\xi \hat{\mathbf{x}}} + N_t, \qquad [7.3]$$

where α= [0, 1] is the amplitude of the second echo, ξ is the parameter associated to the attenuation of the second plateau, modelled as a decreasing exponential, ^x is the normalized samples vector, and N_t is the term associated to the thermal noise. The normalized waveform re-scaled by the overall amplitude A_{wf} , can therefore be modelled as:

$$S_{iced\_lake}(\mathbf{x}, \theta_\mathbf{p}) = A_{wf} \hat{S}(\mathbf{x}) \qquad [7.4]$$

where $\hat{S}(x)$ is the model function of Eq. (7.3) normalized to unit and

$$\theta_\mathbf{p} = \{A_{wf}, \Delta_{ICE}^{gates}, \alpha, \xi, x_c\} \qquad [7.5]$$

is the five parameters vector. The ice thickness in unit of meters, Δ_{ICE}, is defined by applying the following conversion from range gates to meters:

$$\Delta_{ICE} = \Delta_{ICE}^{gates} \frac{c_{ice}}{2B} = \Delta_{ICE}^{gates} \frac{c}{n_{ice} 2B} \qquad [7.6]$$

where B is the radar bandwidth, $c_{ice} = c / n_{ice}$ is the light speed in the ice, with c the speed of light in the vacuum and nice the refractive index of ice.

7.2 Algorithm definition

The LRM LIT algorithm is a retracker specific to the LIT analysis of the radar waveforms, based on the modelling described in section 4.1. For each data cycle, and a given Region of Interest (RoI) defined by a latitude cut $LW_{LIT} = [lat_{min}, lat_{max}]$ over a given target lake, the LIT analysis consists of two steps: 1) the optimization step, that is, the waveform fit, and 2) the estimation of the parameters' mean and standard deviation, as described below and summarized in Figure 19.

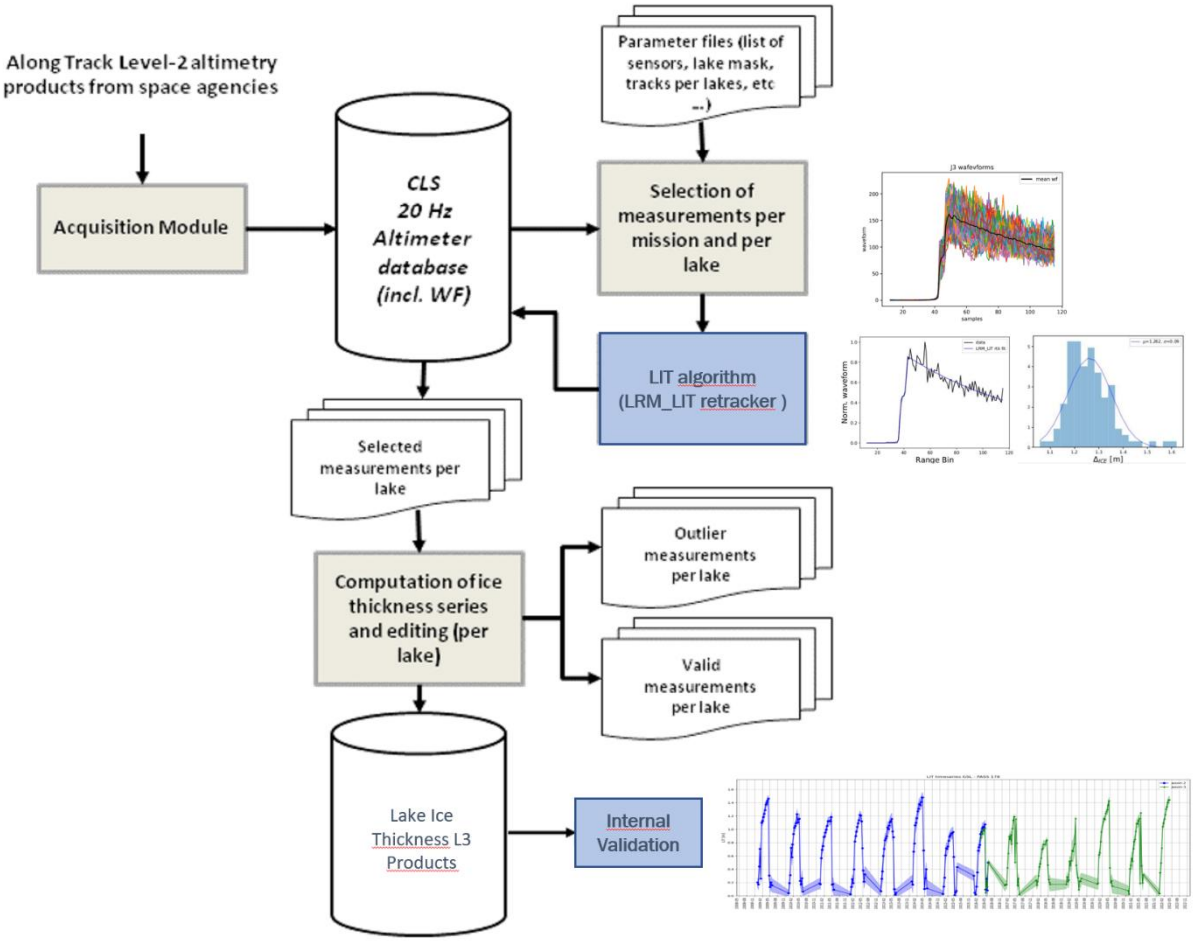

Figure 19: Major steps of the LIT processing

7.2.1 Step 1: Optimisation and best fit parameters

The optimisation step consists of performing a Least Square Levenberg-Marquardt weighted fit of each echo in the LIT analysis window with the model described in 7.1. The optimized function is:

$$\chi^2 = \mathbf{r}^T \mathbb{C}^{-1} \mathbf{r} \simeq \sum_i \left(\frac{r_i}{\sigma_i}\right)^2 \qquad [7.7]$$

where, $r = y(x) - S_{model}(x; \theta_p)$ is the vector of residuals between the waveform data, $y(x)$, and the model, $S_{model}(x; \theta_p)$. The weights, σ_i, are computed as the standard deviation of the echoes within the LIT analysis window. For each data cycle, a set of best fit values for each of the five parameters is provided from the fit of the individual echoes in the analysis window.

7.2.2 Step 2: Parameters estimation and LIT retrieval

The second step of the retracking analysis is the parameter estimation which provides, as the main output, the LIT measurement with the associated uncertainty. The estimation is done by computing the mean and standard deviation of the best fit parameters for each data cycle in the LIT analysis window. To get the constraints on the five parameters with the corresponding uncertainties for each cycle, the histograms of the five parameters best fit values estimated from the fit of each echo is computed. A Gaussian fit on the histograms is performed to get, for each parameter, the mean and variance.

In order to manage eventual outliers, we consider the fit results for which the model and the observations agree within three standard deviations (that is, a reduced chi-squared < 3) . We also discard fit results that could give unrealistic LIT values of Δ_{ICE}>3 meters before computing the LIT histograms and performing the Gaussian fit.

7.3 Quality assessment

7.3.1 Quality checks

We perform reduced chi-squared goodness of fit tests. An example of LIT estimation as a function of latitude along a Jason-2 altimeter track (step 1 of the LRM_LIT retracker) with the reduced chi-squared values for each fitted waveform over Great Slave Lake is shown in Figure 20. Reduced chi-squared values around 1 indicate that the fit performs correctly.

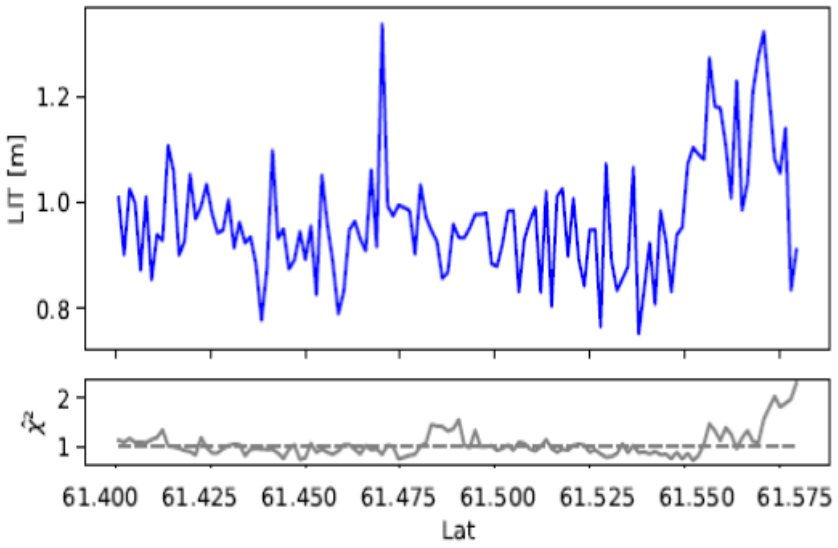

Figure 20: Example of LIT estimation as a function of the latitude along Jason-2 track 45 over the Great Slave Lake (top panel) and the associated reduced chi2 goodness of fit statistics (bottom panel)

7.3.2 Validation

The LRM_LIT retracker has been validated on simulations representative of Jason-like missions. A summary is given in Figure 21, where the top plots refer to winter-like simulated waveforms (left panel) and the LIT histogram (right panel).

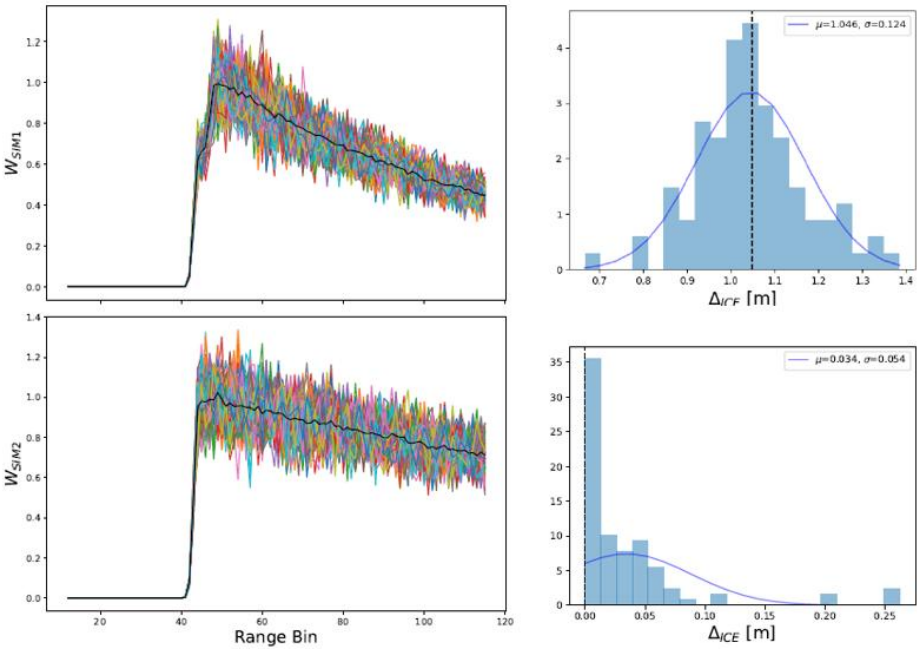

Figure 21: Validation of the LIT estimation with the LRM_LIT retracker on Jason-like simulations. In the left column are shown Jason-like waveform simulations corresponding to the winter-like SIM1 waveforms (top) and to the summer-like SIM2 waveforms. In the right column are shown LIT histograms computed for the winter-like simulations SIM1 (top panel) and for the summer-like simulations SIM2 (bottom panel). The blue lines correspond to the Gaussian fit of the histograms. The input values used to generate the simulations are also shown as dashed black lines.

The input value used to generate the simulations is shown as a dashed line. The same description applies to the bottom plots, for the summer-like simulations without the ice signature. In both cases the LRM_LIT retracker gives unbiased LIT results. The uncertainty of the LIT retrieval from the winter-like simulations is ~10 cm.

LIT retrievals from satellite missions have been evaluated against LIT simulations from the thermodynamic lake ice model CLIMo [Duguay et al., 2003]. A qualitative comparison with in-situ data was also performed when possible[1]. Figure 22 provides an example of the comparison of the LIT estimations obtained within a winter season over Great Slave Lake with the LRM_LIT retracker applied to Jason-2 data (blue triangles) and Jason-3 data (red stars) and LIT from CLIMo simulations with different on-ice snow depth scenarios (diamonds) and in situ data (circles). There is an excellent agreement between Jason-2 and Jason-3 LIT estimates, which are fully compatible with the thermodynamic simulations and qualitatively in agreement with in situ data. We note that, in general, the LIT melting phase is detected earlier with the satellite-based measurements because of snow melting that perturbs the radar echoes.

[1] It is worth noting that the comparison between LIT estimates from satellite missions and in situ data must be taken with caution. In fact, in situ data are collected near the shore, while satellite data are taken from the middle of the lake to avoid land contamination. These are indeed two different environments in terms of bathymetry, wind exposure, snow type and quantity. All these parameters play a key role on ice formation and thickness and they can lead to significant LIT differences.

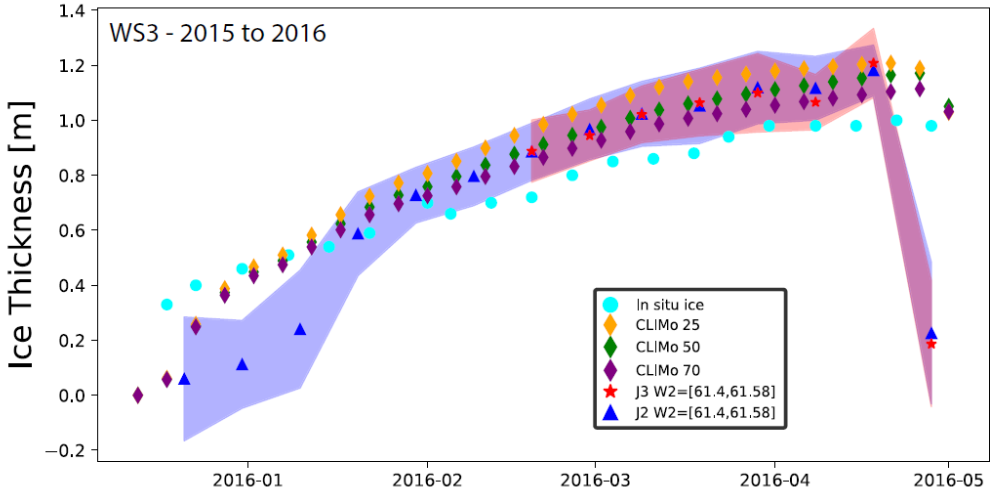

Figure 22: LIT estimates over Great Slave Lake for the 2015-16 winter season. Shown are a comparison between LIT estimates with the LRM_LIT retracker from Jason-2 (triangles) and Jason-3 (stars) data, CLIMo simulations (diamonds) and in situ data (circles). The shaded areas correspond to the LIT estimation uncertainties computed from Jason-2 data (blue) and Jason-3 data (red). Three different realizations of CLIMo simulations are shown by varying the amount of snow on the ice. The in-situ data consist of ice thickness measurements collected in Back Bay near Yellowknife.

To quantify the comparison between the LIT estimates from Jason-2, Jason-3 and CLIMo, two statistics are computed, the MBE:

$$MBE = \frac{1}{N}\sum_{i}^{N}(LIT_i^{J2} - LIT_i^{DS}) \qquad [7.8]$$

And the RMSE:

$$RMSE = \sqrt{\frac{1}{N}\sum_{i}^{N}(LIT_i^{J2} - LIT_i^{DS})^2} \qquad [7.9]$$

of the LIT estimates derived from Jason-2, LIT^{J2}_i , and the other data sets, LIT^{DS}_i , for the N measurements obtained in the middle of the winter season. In the illustrative case of the 2015-16 winter season shown in Figure 22, agreement between the Jason-2 (blue triangles) and Jason-3 (red stars) LIT measurements is excellent. In the middle of the ice season, the MBE is only 0.013 m and the RMSE is 0.024 m between the two data sets. Also, the difference in the LIT mean value is only 0.02 m and that of maximum LIT is 0.025 m. Both Jason-2 and Jason-3 LIT are in strong agreement with the thermodynamics simulations with 50% of snow on ice as input (CLIMo-50 simulations), in particular in the middle of the ice season where the MBE between Jason-2 and CLIMo-50 is less than 0.01 m and the RMSE is 0.019 m. Overall, these results demonstrate that LIT estimates can be retrieved from radar altimetry data that are compatible with thermodynamic simulations and qualitatively in agreement with in situ measurements.

Finally, the superposition of the LIT retrievals on RADARSAT-2 synthetic aperture radar (SAR) and MODIS optical images allows for a better assessment of the consistency of the LIT estimates as they provide valuable information about the state of the ice and overlaying snow cover. Figure 23 shows (left column from top to bottom) the Jason-2 LIT estimates superimposed on RADARSAT-2/MODIS images obtained within one day of Jason-2 overpasses in December, February, March and end of April. The ice thickness is colour coded and ranges from no or thin ice (0-0.32 m) in light blue to LIT in the range of 1.28- 1.60 m in pink. Plots on the right-hand side of Figure 23, show the spatial evolution of the Jason-2 LIT estimates (top plots) and the corresponding evolution of the reduced chi-squared statistics as a function of the latitude (bottom plots) for the same dates as in the left column.

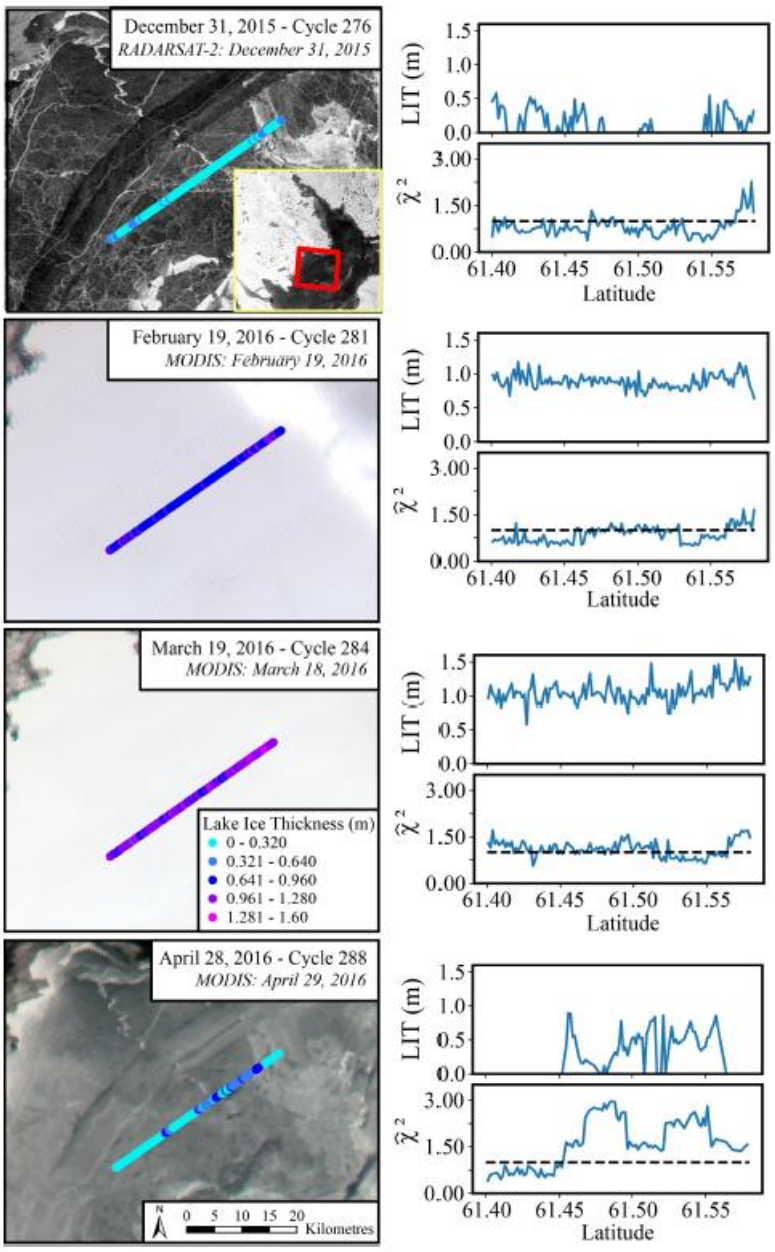

Figure 23 Evolution of Jason-2 LIT estimates over Great Slave Lake along track 45 for WS3 (winter season 2015-2016). Plots in the left column show, from top to bottom, along-track Jason-2 LIT estimates superimposed on MODIS images on the same date or within one day in December, February, March and end of April. Plots in the right column show the evolution of the Jason-2 LIT estimates as a function of latitude (top plots) and of the reduced chi-squared statistics as a function of the latitude(bottom plots) along the track.

7.4 Summary of the strengths, weaknesses and limitations

Overall, the LRM_LIT retracker provides an excellent fit to the data as well as a consistent and robust estimation of LIT over the whole ice growth period. The retracker can capture the inter-annual LIT variations and the seasonal transitions of ice forming and melting but cannot precisely follow the ice evolution at the transitions because of the difficulty of retracking heterogeneous surfaces when the ice is too thin and when snow on the ice surface begins to melt. The accuracy of retrievals, once the ice is well established on the lake surface, is in the order of 0.10 m, providing a significant improvement when compared to previous studies.

The LIT analysis has been illustrated over one representative lake, the Great Slave Lake, but the method can be easily generalized to other target lakes providing that the ice signature, that is, the step like feature

in the leading edge, is present in the radar waveforms. Indeed, the freshwater ice signature depends on the properties and thickness of the snowpack and the ice layer and could be erased if some conditions are not met, as for instance in the case of snow-free lake ice or melting snow on the ice surface. In any case, the presence of the ice signature in the radar waveform is a requirement general enough to ensure the robustness of the method over a large number of freshwater lakes. Based on these findings, it can therefore be concluded that the LRM_LIT retracker method is a novel and promising tool for monitoring variability and trends in LIT.

7.5 References

Brown, L.C. & Duguay, C.R. (2010). The response and role of ice cover in lake-climate interactions. Progress in Physical Geography, 34(5), 671–704, doi: 10.1177/0309133310375653

Brown, L.C. & Duguay, C.R. (2011). A comparison of simulated and measured lake ice thickness using a shallow water ice profiler. Hydrological Processes, 25, 2932–2941, doi: 10.1002/hyp.8087.

Duguay, C.R., Flato, G.M., Jeffries, M.O., Ménard, P., Morris, K. & Rouse, W.R. (2003). Ice cover variability on shallow lakes at high latitudes: Model simulations and observations. Hydrological Processes, 17(17), 3465-3483.

Ghiasi, Y., Duguay, C.R., Murfitt, J., Thompson, A., van der Sanden, J., Drouin, H. & Prévost, C. (2020). Application of GNSS interferometric reflectometry for the estimation of lake ice thickness. Remote Sensing, 12, 2721, doi:10.3390/rs12172721.

Kheyrollah Pour, H., Duguay, C.R., Scott, A. & Kang, K.-K. (2017). Improvement of lake ice thickness retrieval from MODIS satellite data using a thermodynamic model. IEEE Transactions on Geoscience and Remote Sensing, 55(10), 5956-5965, doi: 10.1109/TGRS.2017.2718533.

Mangilli, A., Thibaut, P., Duguay, C.R. & Murfitt, J. (2022). A New Approach for the estimation of lake ice thickness from conventional radar altimetry. IEEE Transactions on Geoscience and Remote Sensing, vol. 60, pp. 1-15, 2022, Art no. 4305515 https://doi.org/10.1109/TGRS.2022.3197109

Murfitt, J.C., Brown, L.C. & Howell, S.E.L. (2018). Estimating lake ice thickness in Central Ontario. PLoS ONE, 13(12), e0208519, https://doi.org/10.1371/journal.pone.0208519.

Murfitt, J. & Duguay, C.R. (2021). 50 years of lake ice research from active microwave remote sensing: Progress and prospects. Remote Sensing of Environment, 264, 112616, https://doi.org/10.1016/j.rse.2021.112616.

Surdu, C., Duguay, C.R., Brown, L.C. & Fernández Prieto, D. (2014). Response of ice cover on shallow Arctic lakes of the North Slope of Alaska to contemporary climate conditions (1950-2011): Radar remote sensing and numerical modeling data analysis. The Cryosphere, 8, 167-180, doi:10.5194/tc-8-167-2014.

Vuglinsky, V. (2017). Assessment of changes in ice regime characteristics of Russian lakes and rivers under current climate conditions. Natural Resources, 8, 416-431.

8 Lake Storage Change – LSC

8.1 Description

The volume of water stored in lakes and reservoirs is important to monitor the impact of anthropic use and climate change at local and global scales. Satellite altimeters and optical instruments are used to determine the water level and surface extent of lakes and reservoirs with high precision. Lake Storage Change (LSC) can subsequently be derived from Lake Water Level (LWL) and Lake Water Extent (LWE).

A split between two different classes of lakes is proposed: those that are surface-varying and those that are not. This division implies different methodologies and possibilities concerning the production of LSC time-series. In some cases, surface-varying lakes can lead to the estimation of LSC time-series from 1984 onwards without water height information and solely relying on LWE with Digital Elevation Model data. Combining this information with topographic data allows us to extrapolate changes in the volume of water in a lake over even longer time spans. In most cases, the use of LWL and LWE will lead to an efficient assessment of LSC time-series.

8.2 Algorithm definition

In the proposed algorithm, the first step is to check the surface variability of the lake to distinguish varying and unvarying lakes. This information determines how lake storage change will be retrieved. If the lake to monitor is considered as varying surface wise, an estimation of the hypsometric curve (through parametric estimation with polynomial model) from height and surfaces time series is done. The LSC is extracted by the integration of this curve. If the lake is considered as unvarying surface wise, the LSC is directly computed from the mean area of the lake and height time series with the basic volume formula. In the absence of altitude time series, surface area time series and DEM availability, a complementary method has been developed to reconstruct altitude time series. The final detailed pipeline setup is displayed on Figure 24.

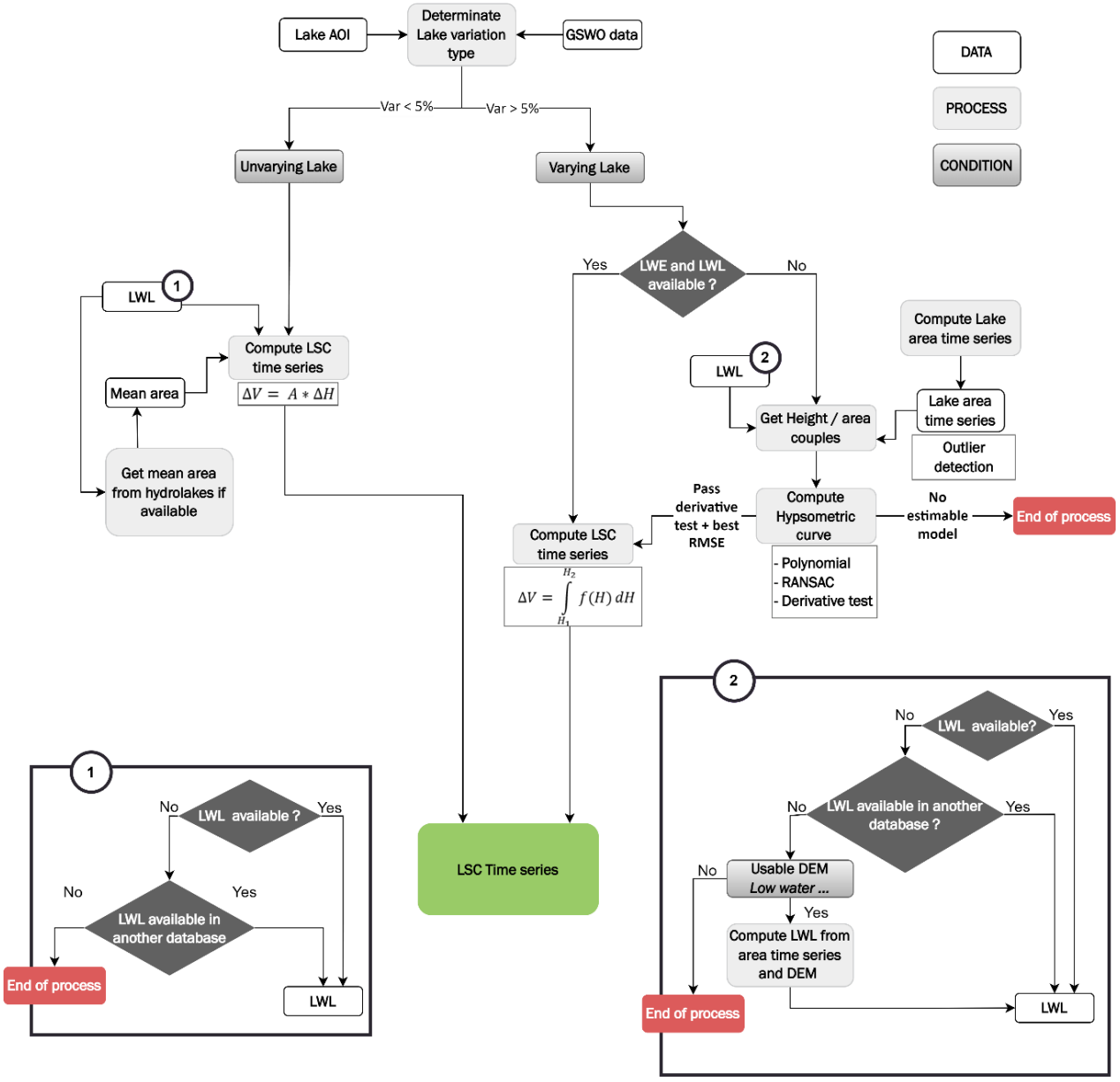

Figure 24: LSC production pipeline

8.2.1 Varying versus unvarying surface area

Water level change typically induces water surface area variation but, in some cases, lakes do not vary much in extent but only in level and *vice versa*. This low variation undermines the estimation or use of an accurate hypsometric curve with the current remote sensing data resolution. The separation between static and dynamic water bodies in terms of water area changes is done here using the Global Surface Water Occurrence (GSWO, Pekel et al., 2016) dataset, which encompasses water surfaces from 1984 to 2021 using Landsat. A particular water body will be determined thanks to an Area Of Interest, whose precision is key to focus only on the body of interest and not surrounding watered areas.

To determine the estimated extent of lake surface variation, the surface corresponding to at least 15% of water occurrence (nearly full state of the lake) is compared to the surface corresponding to the maximum occurrence detected minus 20% occurrence (lowest observed state of the lake), as presented in **Error! Reference source not found.**). These values have been chosen to avoid considering erroneous

measurements present in the GSWO dataset or artefacts linked with border effects which might correspond to mixed pixels, but also to consider reservoirs that have begun being filled up after the first Landsat measurements, which induce lower occurrence than 90% for “permanent” water bodies. That way, the water body surface variation is estimated in relation to its nearly maximum extent.

$$\Delta S = S_{GSWO \geq 15\%} - S_{\mathrm{GSWO} \geq \max(GSWO) - 20\%} \quad (1)$$

We consider a lake as unvarying surface-wise if its surface variation ΔS between lowest and nearly full states of the water body using GSWO is lower than 5% of the maximum observed extent (i.e $\Delta S \leqslant 5\%$). By using this methodology, 995 lakes of the 2024 lakes in CRDP2.1 can be considered as unvarying surface wise.

8.2.2 Alternative height estimates from DEM

When no altimetry information can be retrieved from remote sensing satellites due to the lack of coverage (spatially and timewise) or inaccurate measurements, another approach must be considered. Thus, the use of precise water surfaces derived from high-resolution imagery is a starting point to estimate the water level from their contours projected on DEM. This way, both height and surface are retrieved at the same time, which allows the direct estimation of the hypsometric curve. This approach can also be used to enlarge the LSC time series for lakes where only recent altimeters are available, as the first regular imaging satellite data began work in 1984 with Landsat 4.

We must keep in mind that ideally, and for LSC estimation, the acquisition of a DEM should be at the lowest level of the water body which is rarely the case. Hence, if we observe a lowering trend of lake water height with time, recent DEM will be more suitable than older ones. The methodology proposed is summed up as follows in four steps:

7) Open each water mask extracted from the optical sensors, and project it to precisely warp the DEM projection in extent and resolution
8) Extract the contours from all the water areas
9) Extract all the DEM elevation values overlapped by the contours:
10) Select a representative height value: from the extracted DEM elevation values, the median value provided the most accurate estimate.

If the methodology is sound in numerous cases, its use at an operational level cannot yet be assured, as it still needs an important supervision to produce accurate results.

8.2.3 Hypsometric curve definition

The Area versus Height curve of a lake is also called the hypsometric curve. It is by design estimated as a polynomial function during the LWE time-series production from LWL. For LSC production, it is retrieved from the LWL and LWE production chains and used as detailed below.

8.2.4 Volume variation determination

Once the model of the hypsometric curve has been estimated, it is possible to calculate the LSC. Since the model of the curve is defined as a function of heights, the estimation involves integration between the oldest height (H_0) and each height in the subsequent time series where f is a polynomial function (1).

$$\Delta V = \int_{H_0}^{H_i} f(H)\, dH \quad (1)$$

If the surface variation rate is less than 5%, then a basic volume formula will be applied. Upstream, we calculate an average surface (A) value representative of the lake and apply the following formula (2).

$$\Delta V = \Delta H_0^i * A \quad (2)$$

8.3 Quality assessment

In the proposed algorithm, we rely strongly on the quality of the datasets provided by the LWL and LWE producers. The main difference in terms of quality remains between the lakes varying surface-wise and the unvarying ones as defined in our algorithm (see previous section):

- For varying lakes surface-wise, the quality of the LSC estimated is directly linked to the quality of the hypsometric curve established by the LWL and LWE producers.
- For unvarying lakes surface-wise, the static water surface area will be extracted from the HydroLakes database (Messager et al. 2016). Thus, an error in this dataset will have an impact on the LSC estimation. Besides this point, the quality of the LWL on such lakes will drive the LSC behaviour.

8.4 Summary of the strengths, weaknesses and limitations

The strengths of the methodology proposed for LSC estimation is that it can be applied theoretically on any water body at a global scale. Relying on the outputs of the LWL and LWE teams, the quality is already established during their processing.

The main weakness relies on the existence of LWL time-series on the water body, which drives in any case the LSC time-series production. The use of the height from DEM methodology has also a weakness in the fact that it is hardly automatically usable as it is and still needs strong human supervision and needs precise water surfaces masks for contour delineation. Also, there is still no guaranty that this approach will succeed in all cases.

The main limitation concerns the surface-unvarying lakes with no LWL time-series. For these water bodies, no long time-series of LSC can be produced.

8.5 References

Crétaux, J.-F., Abarca-del-Río, R., Bergé-Nguyen, M., Arsen, A., Drolon, V., Clos, G., & Maisongrande, P. (2016). Lake Volume Monitoring from Space. *Surveys in Geophysics*, *37*(2), 269–305. https://doi.org/10.1007/s10712-016-9362-6

Magome, J., Ishidara, H., & Takeuchi, K. (2003). Method for satellite monitoringof water storage in reservoirs for efficient regional water management. IAHS Publ. no.281, pp.303-310.

Messager, M. L., Lehner, B., Grill, G., Nedeva, I., & Schmitt, O. (2016). Estimating the volume and age of water stored in global lakes using a geo-statistical approach. *Nature Communications*, *7*(1), 13603. https://doi.org/10.1038/ncomms13603

Pekel, J.-F., Cottam, A., Gorelick, N., & Belward, A. S. (2016). High-resolution mapping of global surface water and its long-term changes. Nature, 540(7633), 418–422. https://doi.org/10.1038/nature20584